Nuclear Heat Dose Rate Separation by Calculation and Measurement

Haack, K.

Publication date:
1972

Document Version
Publisher's PDF, also known as Version of record

Risø Report No. 119

Danish Atomic Energy Commission

Research Establishment Risø

Nuclear Heat Dose Rate Separation by Calculation and Measurement

by Karsten Haack

March 1972

Sales distributors: Jul. Gjellerup, 87, Sølvgade, DK-1307 Copenhagen K, Denmark
Available on exchange from: Library, Danish Atomic Energy Commission, Risø, DK-4000 Roskilde, Denmark

U.D.C.
621.039.564.5

Nuclear Heat Dose Rate Separation by Calculation and Measurement

by

Karsten Haack

Danish Atomic Energy Commission
Research Establishment Risø
DR 3

Abstract

An adiabatic and an isothermal rod type calorimeter have been developed. A detailed description of design, construction, instrumentation, and handling equipment is given together with the results from calibrations and measurements.

Correction calculations of the heat contributions from thermal- and fast-neutron flux reactions in the calorimeter sample and structure are made in order to isolate the primary γ-heat in each core position. A guide is given on the similar calculations to be done for a rig design in order to estimate the total nuclear heating.

Graphs showing the vertical distributions of γ-heat in the fuel elements and the experiment holes of DR 3 are included in the report.

The calorimeter characteristics are:

Type	Outer diameter (mm)	Sensitivity range (W/g)
Adiabatic A25	25	0.005 - 0.500
Isothermal I6	6	0.1 - 5

ISBN 87 550 0130 0

CONTENTS

Page

1. INSTRUMENT DEVELOPMENT

1.1. Experimental Facilities in DR 3

DR 3 is a 10 MW, heavy-water-moderated and -cooled reactor using highly enriched U^{235} fuel.

A vertical view of the reactor top is shown in fig. 1. Experimental facilities in the heavy water are the four 4V holes (4" width) and the four 7V holes (7" width). Furthermore, experimental facilities are available in the 2" central holes of the hollow fuel elements. Four horizontal 7" through-tubes penetrate the moderator tangentially to the core.

In the graphite reflector six 4VGR (4" width) experimental holes are located.

1.2. Previous Measurements

The nuclear heat in one of the horizontal and two of the vertical 7" experiment tubes: 7-TLA/4, 7V1 and 7V2, was measured from March 1961 to February 1962 by means of a 25 mm o.d. isothermal gas-gap calorimeter. The aluminium sample contained an electrical heater for calibration purposes and was suspended inside the outer can by means of three 0.2 mm constantan wires, which formed a thermocouple together with the copper leads from the calorimeter to the instrumentation. These leads and those for the heater were passed in ceramic capillary tubes, through a 10 mm aluminium tube to the outside of the reactor. The construction was rather fragile, and the calorimeter was therefore difficult to handle. Many faults occurred, and as the results obtained in 7V1 and 7V2 were in rather bad agreement with those obtained in other "PLUTO"-type reactors, the measurements were stopped in February 1962.

An adiabatic calorimeter developed at DR 3 was used for a single measurement in 7V2 in March 1962. This calorimeter contained a copper sample, insulated with mineral wool against the 27.5 mm o.d. aluminium can. The temperature in the sample was measured by means of a 1 mm o.d. stainless-steel-sheathed and mineral-insulated cromel/alumel thermocouple. The result did not correspond with the results from the isothermal calorimeter mentioned above, nor with those from other "PLUTO"-type reactors. All nuclear-heat measurements were therefore stopped, and a literature study was started in order that more reliable calorimeter types, suiting the operating and space conditions of DR 3, might be designed.

1.3. Design Considerations

The nuclear heat in the core region was estimated to be a few W/g. Previous measurements had shown that the nuclear heat in the experimental tubes outside the core was in the range 10 - 500 mW/g.

The access to the Mk. II fuel elements is through the 7.8 mm i.d. flux scanning tubes, which are mounted on the concave outer side of the fuel element box. Mk. III and Mk. IV elements which are not occupied by rigs are normally equipped with flux scan rigs carrying a tube similar to that of the Mk. II elements.

For access to be gained to the experimental holes outside the core, new plugs had to be constructed. Thus the choice of dimensions was independent of the existing equipment in that case.

It was therefore decided to construct a calorimeter with an accuracy better than 5% for measurements in experiment tubes. The small tube size in the fuel elements impeded the use of that calorimeter in these, and a simpler type therefore had to be constructed. In order to obtain the best possible accuracy with this simpler calorimeter, equipment for intercalibration of the two types in a Mk. III element was made.

1.3.1. The Adiabatic Vacuum-Gap Calorimeter A 25

The most accurate of the calorimeter types known at the time was thought to be the adiabatic type described by Anderson et al.[2-4]. It was chosen as reference for measurements in experiment tubes, see fig. 2.

The sample size was set at about 10 grammes as a compromise between the aims of obtaining a reasonable heat distribution and at the same time a small self-shielding effect. The outside diameter of the calorimeter was set at 1". Optimization calculations of the sample diameter as shown in ref. 24, taking into account that a thermal sheath had to be placed inside the outer vacuum can, gave an outside diameter of the sample of 13 mm.

The heaters on the sample and on the thermal sheath had to be made of materials which would not essentially affect the measurements either by γ-shielding or by secondary heat arising from nuclear processes in the heaters. 0.2 and 0.3 mm CrNi wires were chosen for the heaters on the sample and on the thermal sheath respectively.

As it is desirable to balance the sample and thermal-sheath temperatures within 0.1°C during the calibrations as well as the measurements, the thermocouples had to be made with insulated junctions. This would give the best protection against creep currents and potentials from voltage drops due to false earth or return currents in the heater circuits. As the response of

Figure 2

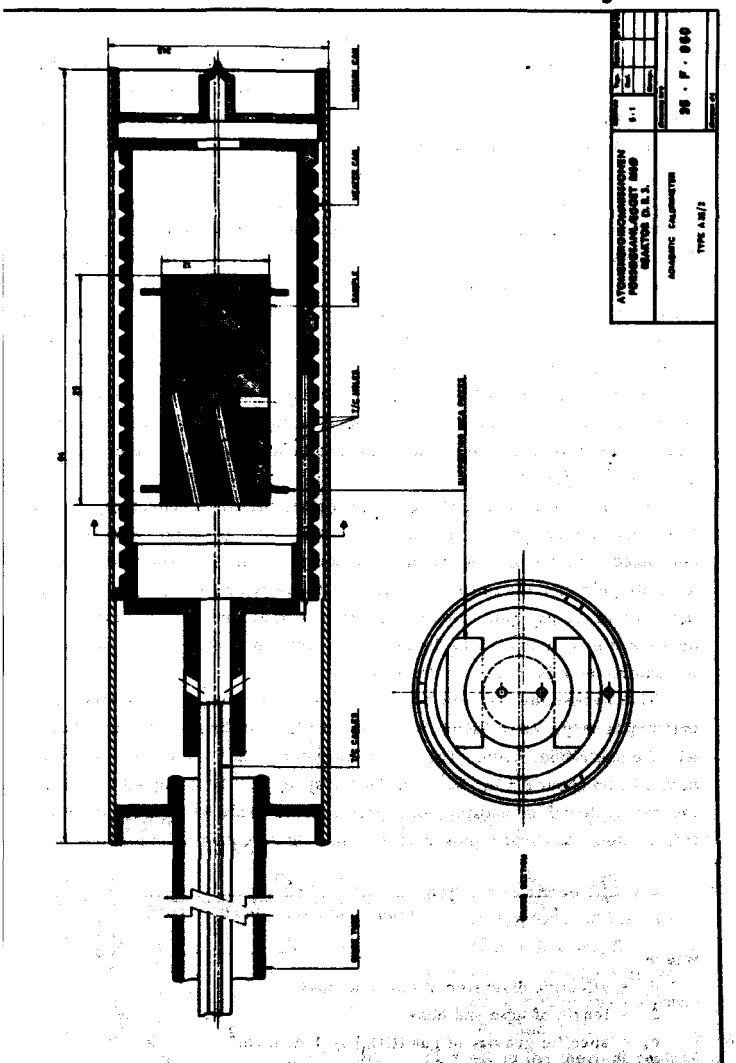
ATOMBRENNSTOFFKOMBINAT
ROSSENDORF/AGGERT 888
DRATOS D.D.R.
1:1
AQUATIC CALIBRATOR
TYPE AK/3
96 - P - 000

a cromel/alumel thermocouple to 0.1 °C is 4 μV, and several volts is led to the heaters, quite a lot of fault possibilities are hidden in this detail.

The temperature range and the demand for radiation constancy of the calorimeter did not allow other electrical insulation than ceramics. The heaters were laid in a cement consisting of Al_2O_2 powder in sodium silicate. All electrical connections had to be made by twisting the wires and pressing a copper capillary tube on the connection.

Silver brazing could not be used in the construction of the calorimeter as the brazing flux contains boron, which is an α-emitter when irradiated in the reactor. The heat generation due to (n, α) processes is very great, and even very small amounts of α-emitting material in the calorimeter structure will lead to erroneous results. In ref. 22 the heat generation due to the (n, α) reaction for boron is calculated to be 1.6 kW per gramme of boron in a thermal flux of 10^{14} n/cm^2 sec.

The thermal conductivity λ of the residual gas in the vacuum gap between the sample and the can is dependent on the gas as well as on the vacuum. The most suitable gas was found to be CO_2 with a value of $\lambda_{atm} = 3.3 \cdot 10^{-5}$ cal/cm°Csec.

During the evacuation of the gas space the thermal conductivity remains fairly constant as long as the mean free path of the gas molecules is small compared with the dimensions of the apparatus. At 10μ (1μ = 10^{-3} Torr) absolute pressure the mean free path of CO_2 is 3.2 mm, which is close to the width of the gas gap. Below 10μ the thermal conductivity of the gas decreases proportionally to the pressure, and a pressure of 1μ or less in the calorimeter is therefore desirable.

This necessitates a very tight outer can, and a long time of vacuum pumping is required to bring the gas molecules out through the supporting Al-tube and rubber hose. The inside diameter of the Al-tube and the rubber hose will be about 8 mm, but some of the space will be occupied by the three thermocouple cables and the two heater cables. This will reduce the effective diameter to about 5 mm, and the pumping rate may be estimated at

$$S = \frac{\sqrt{2\pi}}{6} \cdot \frac{d^3}{l\sqrt{\rho_1}} = 0.418 \frac{0.5^3}{1300\sqrt{0.001977 \cdot 0.102 \cdot 10^{-5}}} \approx 1 \text{ cm}^3/\text{sec},$$

where

- d = effective diameter of tube and hose
- l = length of tube and hose
- ρ_1 = specific gravity of gas (CO_2) at 1 dyn/cm^2
- S = volume removed per sec at the pressure existing in the calorimeter.

As the total volume of the calorimeter is about $V = 36\ cm^3$, the pressure will decrease according to the equation

$$P = P_0(1 - \frac{S}{V})^t = P_0\,(1 - \frac{1}{36})^t$$

if the system is completely tight. This is not possible in practice, and as the rubber and aluminium surfaces need time for degassing, too, several days of pumping are needed.

If a vacuum of 1 μ is obtained, the thermal conductivity of the gas is reduced to

$$\lambda_{1\mu} = 3.3 \cdot 10^{-6}\ cal/cm \cdot {}^{o}C \cdot sec.$$

The heat conduction through the gas gap is then

$$K_g = 3.3 \cdot 10^{-6} \frac{2 \cdot \pi \cdot l_p}{\ln(\frac{d_2}{d_1})} = 1.60 \cdot 10^{-4}\ cal/{}^{o}C \cdot sec,$$

where d_1 and d_2 = inner and outer diameter of the cylindrical gas gap and l_p = length of sample.

The heat conduction along the four thermocouple leads and the two heater leads will be, approximately,

$$K_l = 6 \cdot 2 \frac{\frac{\pi}{4} \cdot d^2}{l_l} = 1.51 \cdot 10^{-4}\ cal/{}^{o}C \cdot sec.$$

The heat conduction through the mica pieces which support the sample can be calculated on the assumption that four of the eight corners of the 0.4 mm mica plates touch the can in an area of 0.4 x 0.5 mm.

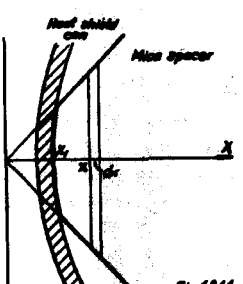

Fig. 4.2.1.1

The heat conduction is in general

$$Q = \lambda \cdot \frac{A}{X} \cdot \Delta T = \frac{1}{M} \Delta T,$$

where A = cross section
ΔT = temperature difference
X = conduction length
λ = specific conductivity of mica = $3.3 \cdot 10^{-3}$ cal/cm · °C · sec
and $M = \frac{X}{A\lambda}$ is the thermal resistance.

For the differential length dx we have (thickness of mica = t cm)

$dM = \frac{dx}{2x \cdot t \cdot \lambda}$, giving a total thermal resistance of

$$M = \frac{1}{2t\lambda} \int_{x_1}^{x_2} \frac{dx}{x} = \frac{1}{2t\lambda} \ln \frac{x_2}{x_1} .$$

The total heat conduction through the four mica corners is then

$$K_m = \frac{2t\lambda}{\ln(\frac{x_2}{x_1})} \cdot 4 = 4.94 \cdot 10^{-4} \text{ cal/}^{\circ}\text{C} \cdot \text{sec},$$

where x_2 is the gas gap width: $x_2 = 0.3$ cm, and $x_1 = \frac{0.05}{\sqrt{2}}$.

The total heat conduction from sample to can is therefore

$$K = K_g + K_l + K_m = (1.60 + 1.51 + 4.94)10^{-4} =$$

$8.05 \cdot 10^{-4}$ cal/°C · sec = 3.37 mW/°C.

In order to keep the error from this heat conduction below 0.1% at a nuclear-heat rate of 100 mW/g Al, the delta temperature between sample and can should be kept below

$$\Delta T_{max} = \frac{W_Y \cdot M_p}{K} \cdot \frac{0.1}{100} = \frac{100 \cdot 10}{3.37} \cdot 10^{-3} = 0.30^{\circ}\text{C},$$

where M_p = mass of sample.

The calculation of the gas-gap heat conduction shows that operation of the calorimeter with the gas at atmospheric pressure would increase the error from the heat conduction by a factor of about 3.

1.3.2. The Isothermal Rod Calorimeter I6

The difficulties in supporting the sample in a calorimeter with an outside can diameter of only 6 mm led to the choice of the rod type (see fig. 3).

In a cylindrical rod of a material with the density V g/cm^3 and the thermal conductivity K W/cm · °C, placed in a λ-field with the heat deposition q W/g, the heat balance

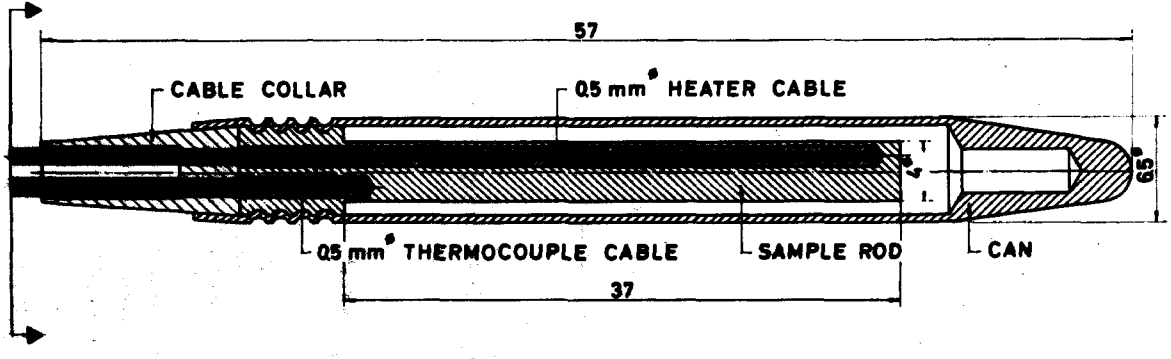

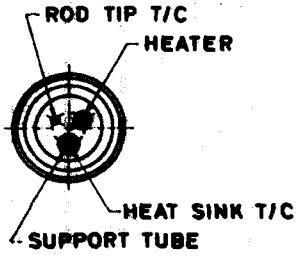

ISOTHERMAL ROD CALORIMETER
TYPE J6

MATERIAL: AL 2S

Figure 3

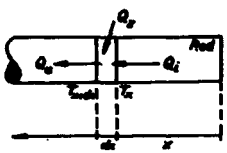

Fig. 1.3.1.1

$Q_u = Q_y + Q_i$ can be written

$$-K \cdot A \cdot \frac{d(T_{(x+dx)})}{dx} = q \cdot V \cdot A \cdot dx - K \cdot A \cdot \frac{dT_x}{dx}.$$

Expansion of the left side according to the Taylor formula gives

$$-K \cdot A \cdot \left(\frac{dT_x}{dx} + \frac{d^2T_x}{dx^2}dx + \frac{d^3T_x}{dx^3} \cdot \frac{(dx)^2}{2} + \ldots\ldots\right) = q \cdot V \cdot A \cdot dx - K \cdot A \cdot \frac{dT_x}{dx}.$$

If we exclude the terms of higher order, this can be reduced to

$$-K\frac{d^2T_x}{dx^2} \cdot dx = q \cdot V \cdot dx$$

$$\frac{d^2T_x}{dx^2} = \frac{qV}{K}.$$

At the free end of the rod $Q_i = 0$, and therefore

$$q \cdot V \cdot A \cdot dx = K \cdot A \cdot \frac{dT_x}{dx}.$$

This gives the rim value for $\frac{dT_x}{dx}$ at the free end of the rod

$$\frac{dT_x}{dx} \to 0 \quad \text{for} \quad dx \to 0.$$

By the substitution of Z for $\frac{dT_x}{dx}$ we get

$$Z \cdot \frac{dZ}{dT_x} = -\frac{qV}{K}.$$

Hence $\int_{Z_o}^{Z} ZdZ = -\frac{qV}{K}\int_{T_o}^{T_x} dT_x$, and as $Z_o = \left(\frac{dT_x}{dx}\right)_{x=o} = 0$,

we have

$$Z^2 = \frac{2qV}{K}(T_o - T_x) \qquad (1)$$

$$x = \int_0^x dx = \pm \int_{T_0}^{T_x} \frac{dT_x}{\sqrt{\frac{2qV}{K}(T_0 - T_x)}} = (\pm)\sqrt{\frac{qV}{2K}(T_0 - T_x)} .$$

The temperature along the rod will then follow the equation

$$T_x = T_0 - \frac{qV}{2K} x^2. \qquad (2)$$

The main disadvantages of the rod-type calorimeter are

(a) the heat loss from the rod to the can through the gas gap;

(b) the difficulties in measuring the correct temperature at the fixed end of the rod.

In order to reduce the error from (a) the temperature difference between the rod ends should be kept as small as the sensitivity of the instrumentation allows, i. e. about 20°C. The length L of the rod is then determined by eq. (2) at

$$T_0 - T_x = 20^\circ C \;\Rightarrow\; L = \sqrt{\frac{2 \cdot 2.09}{3 \cdot 2.7}}\,(20) = 4.5 \text{ cm}.$$

The heat transfer through the gas gap could be reduced by evacuation, but as continuous pumping would be impossible because of the small dimensions of the connecting pipe, and as the tightness of a sealed system was thought to be insufficient to keep the pressure at 1# , it was decided to have the gap filled with gas at normal pressure.

The heat transfer through the gas gap is then

$$K_g = \int_0^L \lambda \frac{2\pi dx}{\ln\frac{d_2}{d_1}} (T_x - T_K) = \frac{2\pi\lambda}{\ln\frac{d_2}{d_1}} \cdot \frac{qV}{2K} \int_0^L (L^2 - x^2)dx =$$

$$\frac{2\pi\lambda qVL^3}{3K\ln\frac{d_2}{d_1}} \simeq 0.05\, q \text{ W}. \qquad (3)$$

As this is 5% of the estimated nuclear heat in the sample, it was found advantageous to provide for a possibility of calibrating the calorimeter, e. g. by installing an electrical heater, which is able to simulate the uniform

distribution of nuclear heat in the rod. The heater of the best shape would be a thin, cylindrical one along the entire length of the rod.

1.4. Constructions

1.4.1. Construction of Type A25

A number of technological difficulties made the first attempt to construct this type less successful. The experience gained is briefly resumed in the following.

The supporting mica rings between the sample and the can were made in such a way that the thermal resistance was at its maximum. This resulted in a rather fragile structure as the mica tended to split into a number of layers already during the preparation. One of the rings burst after a few days' operation, and the sample moved sideways by degrees at the unsupported end (see X-ray photo, fig. 4a) until it touched the can after seven months' operation. Then the calorimeter had to be scrapped.

The next model, A25/2, was made with rectangular mica pieces, two at each end of the sample (see fig. 2), pinched in grooves in the sample and touching the inside of the can only with their corners.

It is desirable to reduce the mass of the calorimeter structure outside the sample as much as possible in order to minimize the errors from radiation produced by nuclear reactions in the structure. This raised problems of vacuum-tight welding of the outer can, which had a plate thickness of only 0.5 - 1.0 mm. Three weldings were necessary to ensure that the rolling directions of the blanks were parallel to the blank surfaces so as to give the best vacuum tightness. The closing of the last welding seam was difficult because of a small overpressure inside the can produced by the welding heat. The next model, A25/2, was therefore provided with a small tube in the bottom plate for equalizing the pressure. When the seams had been welded, this tube was closed by pressing and welding. The big mass of aluminium at the upper end of A25/1 which can be seen in the X-ray photo fig. 4a is a result of an unsuccessful welding. Unfortunately it contributes significantly to the secondary heating from the structure.

Another problem in the calorimeter construction was the connections of the thin wires from the heaters and the thermocouples to the leads of the mineral-insulated cables connecting the calorimeter to the instrumentation. A point-welding technique was tried, but without success. Better results were obtained by flame welding with thin copper wire as binder. Fluxes could not be used on account of their content of boron. However, the re-

Figure 4

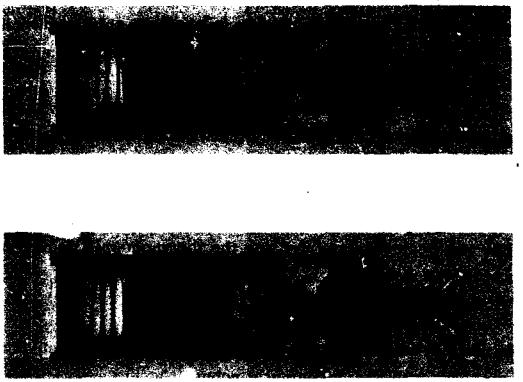

Fig. 4a. Calorimeter type A 25/1. X-ray photo.

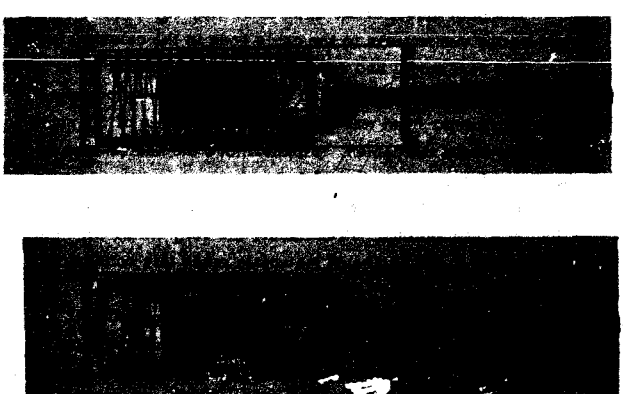

Fig. 4b. Calorimeter type A 25/2. X-ray photo.

producibility of the connections made by flame welding was not sufficient as the content of slag varied too much in the junctions. A method of copper plating the twisted wires was found to be the best solution although junctions made in this way are of course more sensible to corrosion, which may reduce the in-pile life of the calorimeter.

In the first model the can thermocouple hot junction was mounted by caulking the end into a hole drilled slantwise in the can. During the installation in the vacuum jacket and guide tube the thermocouple had to be bent and twisted so that its end was by and by loosened and the thermal contact with the can thus reduced. This was avoided in the second model by making the heater can eccentric and drilling the thermocouple pocket axially where the can side was thickest.

1.4.2. Construction of Type J6

The main problem in this calorimeter type was the construction of a heater small enough and sufficiently robust.

In the first two models the heater was wound round the sheath of the thermocouple which measured the temperature of the free end of the rod. The heater was insulated from the rod and from the thermocouple sheath by means of Al_2O_3-cement.

The first model broke down after only one in-pile irradiation owing to bad heater connections to the cable ends in the calorimeter head.

The next model had an eccentric heater hole in order to give more space for the heater connections and the heat-sink thermocouple. A "collar" on the calorimeter head was to prevent movements of the cable ends when pressed round the cables. Furthermore the heater-to-cable connections were soldered and copper-plated.

In spite of these precautions, the calorimeter did not work for more than two irradiations. Presumably the very small dimensions and the limitations in the choice of materials made this construction method unreliable.

Therefore the third model, J6/3, was supplied with a prefabricated heater made by swaging a 1 mm o.d., mineral-insulated heater cable with two cores of NiCr down to 0.5 mm o.d. in the outer 43 mm of the cable, i.e. the part inside the calorimeter rod. The two NiCr wires were welded together at the end, and the weld was insulated from the inconel sheath of the cable.

By the swaging from 1 to 0.5 mm outer cable diameter the cross section of the NiCr wires was reduced by a factor of 4. Hence the electrical

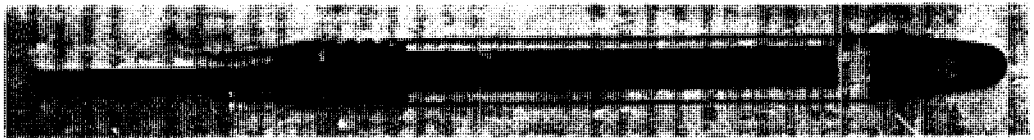

Enlarged

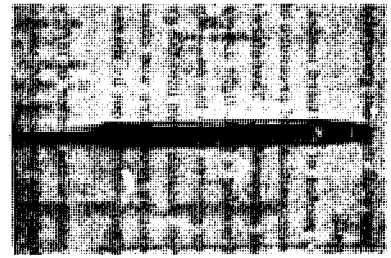

Natural size

Figure 5

Isothermal rod calorimeter type I6
X-ray photos

resistance and thereby the electrical heat generation per cm cable would be increased by a factor of 4. Thus the swaged end of the cable would work as a heater, and still the heat generation in the rest of the cable would be reasonably small.

X-ray photos of the third model are to be seen in fig. 5.

The composition and pressure of the gas between rod and can should be as constant as possible. Therefore experiments were carried out to find a method of making a leak-tight assembly of rod and can. The best solution was to turn grooves into the heat-sink end of the rod and press the can uniformly from outside down into the grooves.

The closing procedure was checked by means of dummy calorimeters. The tests were carried out by mass-spectroscopy methods in a vacuum of 10^{-4} μ.

The cable to the heater of I6/1 was 1 mm cromel/alumel thermocouple cable, which was the only one available in this small dimension at that time. Later on a 1.5 mm o.d. cable with two copper wires mineral insulated in a copper sheath was marketed, and was used in the second model I6/2.

The thermocouples were 1.0 mm Cr/Al in J6/1 and J6/2. In J6/3, 0.5 mm Cr/Al thermocouples were used.

1.5. Instrumentation

In order to maintain a temperature difference in calorimeter A 25 between sample and can not exceeding 0.1 °C during a measurement run, heat must be applied to the can as a compensation for that which disappears to the surroundings. The necessary heat is roughly estimated at about 20 W.

An amplifier chain capable of delivering an output of 20 W at an input of 4 μV, which is the thermocouple signal from 0.1 °C temperature difference, was designed.

A block diagram of the units chosen is seen in fig. 6. The time constants of the chain are settled by the filter between the "Knick" amplifier and the M-line transmitter and by the feedback coupling of the GR-1 preamplifier. The stability of the loop can be controlled by the integration, differentation and proportional band setting knobs on the controller unit, which is coupled to the recorder and set-point unit.

The output amplifier GR13 delivers 20 W at 20 volts. The resistance in the heater circuit was therefore set at 20 Ω. The calibration heater on the sample was connected to a circuit as shown in fig. 7. In order to keep a constant heat deposition at varying calibration temperatures, the sample

Figure 6

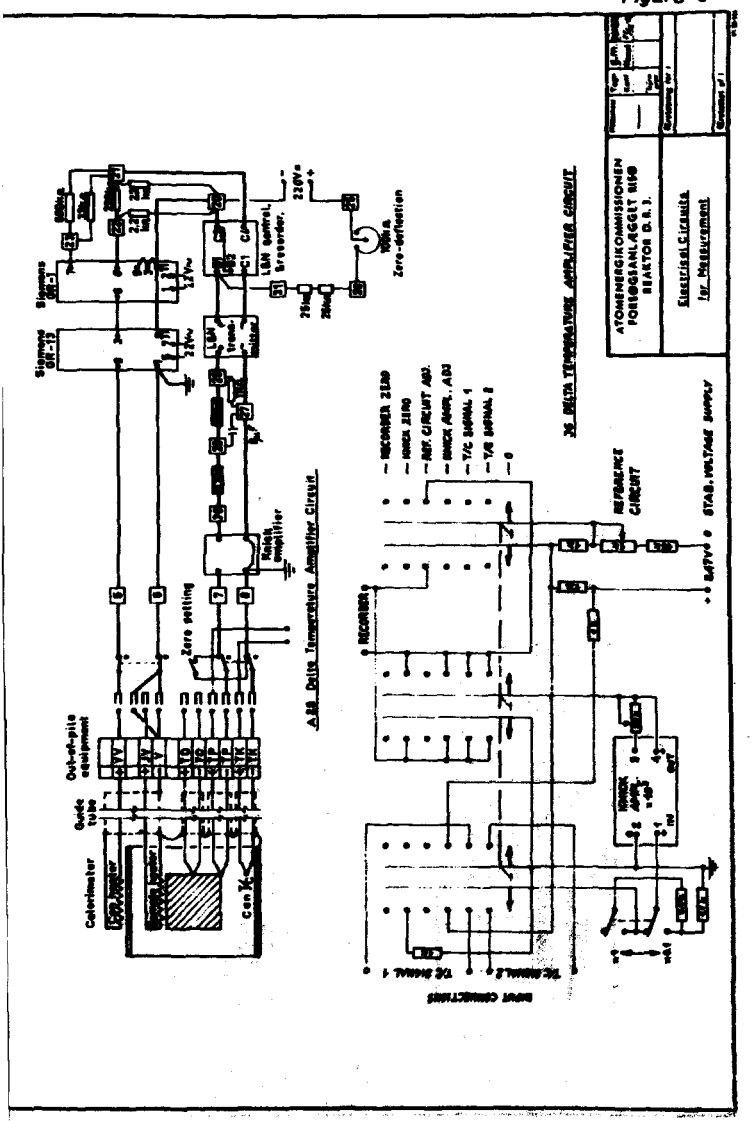
Calorimeter
Guide tube
Out-of-pile equipment
Zero setting
Power amplifier
ΔT Delta Temperature Amplifier Circuit
RECORDER
— RECORDER 2180
— INNER 2180
— REF. CURRENT ADJ.
— BRIDGE BAMPL. ADJ.
— T/C SIGNAL 1
— T/C SIGNAL 2
— 0
ΔT Delta Temperature Amplifier Circuit
REFERENCE CIRCUIT
STAB. VOLTAGE SUPPLY
INNER COMPARTMENT
T/C SIGNAL 1
T/C SIGNAL 2
Zero-deflection
ATOMENERGIKOMMISSIONEN
FORSØGSANLÆGGET RISØ
ROSKILDE (DK)
Electrical Circuits
for Measurement

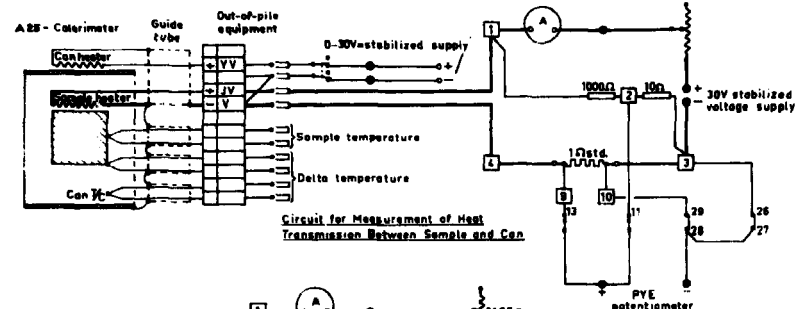

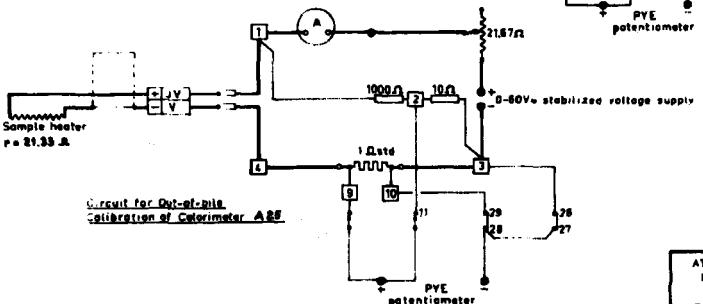

ATOMENERGIKOMMISSIONEN
FORSØGSANLÆGGET RISØ
REAKTOR D. 3.

Electrical Circuits for Calibration

Figure 7

heater was coupled in series with an external resistance to a constant-voltage generator as shown in the diagram. The heat deposition on the sample is

$$W = r \cdot I^2 = \frac{r \cdot U^2}{(R+r)^2},$$

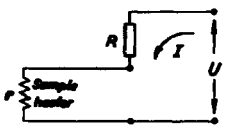

Fig. 1.5.1.1.

and it should be constant when r varies with the temperature, i.e. the slope

$$\frac{dW}{dr} = \frac{U^2(R-r)^2}{(R+r)^2}$$

should be zero, which happens when $R = r$.

The temperature coefficient of the CrNi heater wire is 0.014% per ^{o}C. In calibration run from 25 to 225^{o}C the resistance will vary from say 20.000 Ω to 20.681 Ω, and the power variation will be

$$W\% = (W_{25}-W_{225})100 = \left(\frac{20.000}{(R+20.000)^2} - \frac{20.681}{(R+20.681)^2}\right) U^2 \cdot 100 = 0.012\%$$

if $R = \frac{20.000 + 20.681}{2} = 20.340$ Ω

and U = 40 volts.

The temperature rise rate of the adiabatic calorimeter sample was recorded by a Graphispot GRD-4 recorder, which is of the mirror galvanometer type, in which the recording-pen sledge follows the galvanometer light spot hitting photocells on the sledge.

As this recorder type has a low internal resistance, the demand for maximum sensitivity necessitated the design of a special backed-off power circuit. With the symbols used in fig. 1.5.1.2 the following deduction may be made:

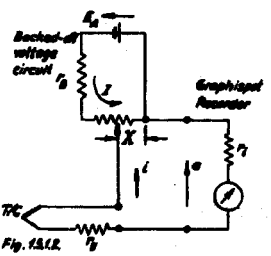

Fig. 1.5.1.2.

The backed-off power current

$$I = \frac{E_A - X \cdot i}{r_B + X}$$

reduces the T/C voltage:

$$E = (r_y + r_i)i + X(I+i) = (r_y + r_i + X - \frac{X^2}{r_B + X})\,i + \frac{E_A \cdot X}{r_B + X} ,$$

and the instrument reading will be

$$e = i \cdot r_i = (E - E_A \frac{1}{1 + \frac{r_B}{X}}) \frac{r_i}{r_y + r_i + \frac{r_B}{\frac{r_B}{X} + 1}} .$$

If $E = E_o + \Delta E$, and X is set so that

$E_o = E_A \frac{1}{1 + \frac{r_B}{X}}$, the expression for e will be

$$e = \Delta E \frac{r_i}{r_y + r_i + \frac{r_B \cdot X}{r_B + X}} .$$

The maximum backed-off power should correspond to about 250°C, i. e. $E_{max} \tilde{=} 10$ mV. With a battery voltage $E_A = 2$ V we have

$$\frac{E_{max}}{E_A} = \frac{0.010}{2} = 0.005 = \frac{X}{X + r_B} \simeq \frac{X}{r_B} \quad \text{as} \quad X \ll r_B .$$

The presence of X must not alter the sensitivity of the recorder more than 0.1%. This demand determines the value of r_B and X because

$$(\,(\frac{e}{\Delta E})X - (\frac{e}{\Delta E})\,)\,100\% = (\frac{r_i}{r_y + r_i} - \frac{r_i}{r_y + r_i + \frac{r_B}{\frac{r_B}{X} + 1}})\,100\%.$$

As $r_y = 140\ \Omega$

and $r_i = 22\ \Omega$, we have

$$0.1 = (\frac{22}{140 + 22 + \frac{r_B}{200 + 1}} - \frac{22}{140 + 22})\,100$$

$\Im : r_B = 221\ \Omega = 200\ \Omega$

and $X = 0.005 \cdot 221 = 1.105\ \Omega \cong 1\ \Omega$.

The resistance X was controlled by means of a two-decade multiswitch because the contact resistance in a sliding rheostat was found to be too uncertain. The resistance steps were 0.008 Ω, corresponding to 25% of full-scale deflection on the recorder.

The isothermal-calorimeter delta temperature was recorded by a Moseley 680 M Strip Chart Recorder. The signal was amplified 1000 times in a "Knick" amplifier, type MV. By means of a stabilized voltage circuit the amplifier and the recorder could be checked frequently, see fig. 6.

1.6. Handling and Supporting Equipment

The A25 calorimeter was mounted on a 3.2 m long Al-tube, which served as connection pipe to the vacuum pump. The calorimeter itself and the nearest 1.2 m of the pipe would be radioactive during the measurements, mainly on account of activation of Al, Cr, Ni, and Cu.

It was therefore necessary to withdraw the calorimeter and the supporting pipe into a "flask" which had an effective shielding round the lower part. The flask was to cut the beam from the open 25 mm hole sufficiently down and shut off the beam when measurements were stopped. The shielding thickness would be of the order of 30 cm, and it was decided to split the shielding into two parts: a 10 cm shield in the flask and a 20 cm movable shield. If all the shielding had been built into the flask, the accessibility of the neighbouring experimental facilities would have been too limited. The flask arrangement is shown in fig. 8.

The vacuum connection between the Al-tube and the vacuum pump was established by means of a hose which was led round a wheel at the top of the flask and down through a drive gear on its side. By means of this gear the calorimeter could be moved up and down.

In the upper position the calorimeter is hidden in a magazine, the bottom of which can be closed with a 10 cm thick cast-iron shutter. When the calorimeter is in measuring position in the reactor the 25 mm beam through the flask is attenuated by a 700 mm long lead cylinder mounted round the top of the Al guide tube.

The connection between the guide tube and the vacuum hose is a lead plug, in which the thermocouples and heater wires are connected to a soft cable moving along the vacuum hose inside the flask. Thus the lead plug contains the cold junctions of the thermocouples.

The position of the calorimeter relative to the horizontal core centre plane is read by means of a periscope on a scale painted on the Al guide tube.

The corrections to the γ-heat originating from the n_f and n_t fluxes in the experiment holes are determined by flux scans in the experimental tubes made through a flux scan hole in the flask-magazine wall. The calorimeter has to be in the magazine during flux scans, and the shutter must be placed in an intermediate position.

A special plug has been made for each of the three types of experiment holes: the 7V, the 4V and the 4VGR-holes.

For measurement of the nuclear heat just at the centre of the facility, guide-tube thimbles are inserted from the top of the plugs to the bottom of the experiment holes. The thimbles are perforated as much as possible in the part where the measurements take place, for the purpose of minimizing the corrections for secondary γ-radiation from nuclear processes in the surroundings of the calorimeter.

The perforations connected the atmosphere in the experiment hole with that in the thimble and the flask and made it necessary to have a tight system from the experiment liner to the flask and from the top of the flask to the movable vacuum hose. It was made by insertion of an intermediate plug between the beam plug and the flask. All connections are O-ring sealed. The top of the flask, including the vacuum-hose wheel, is sealed by a welded plastic cover, flanged to a flexible hose, the other end of which is sealed to the outside of the vacuum hose. The CO_2 pressure in the flask and the experiment hole is controlled by a reduction valve to about 2 mm Hg above the atmosphere. Water locks secure the system against pressure variations due to temperature changes in the experiment hole.

The J6-type calorimeter is operated by means of a gear plug placed on the top of the fuel-element plug (see fig. 10). Two rollers move the calorimeter into and out from the core. By means of small cams on the calorimeter wires and a microswitch activated by the rollers, the calorimeter movement is stopped for a pre-set time for measurements in selected positions. The scanning of fuel elements is automatic and lasts about two hours.

The calorimeter is led to the gear plug through a plastic hose and a shielded guide tube in the "top void", which is the space between the upper side of the fuel-element plug and the top plate.

The gear plug can be moved during full-power operation from one fuel element position to another. To allow the movement the calorimeter is withdrawn to the shielded guide tube, and the plastic hose is disconnected

FLASK

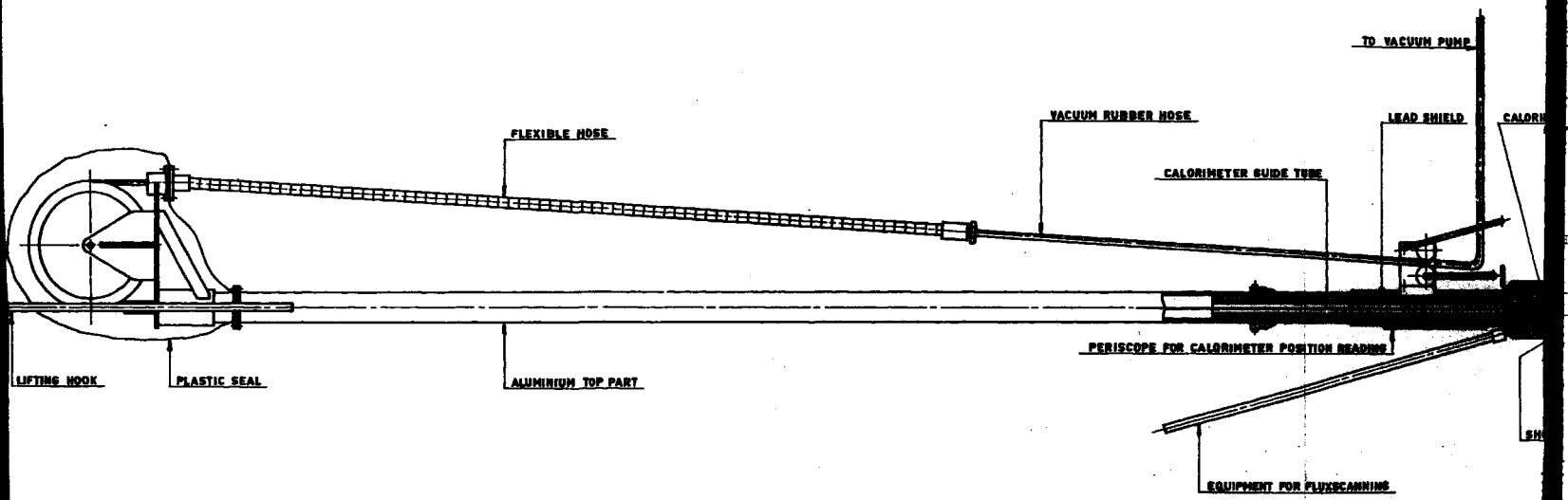

SECTION - I

LASK

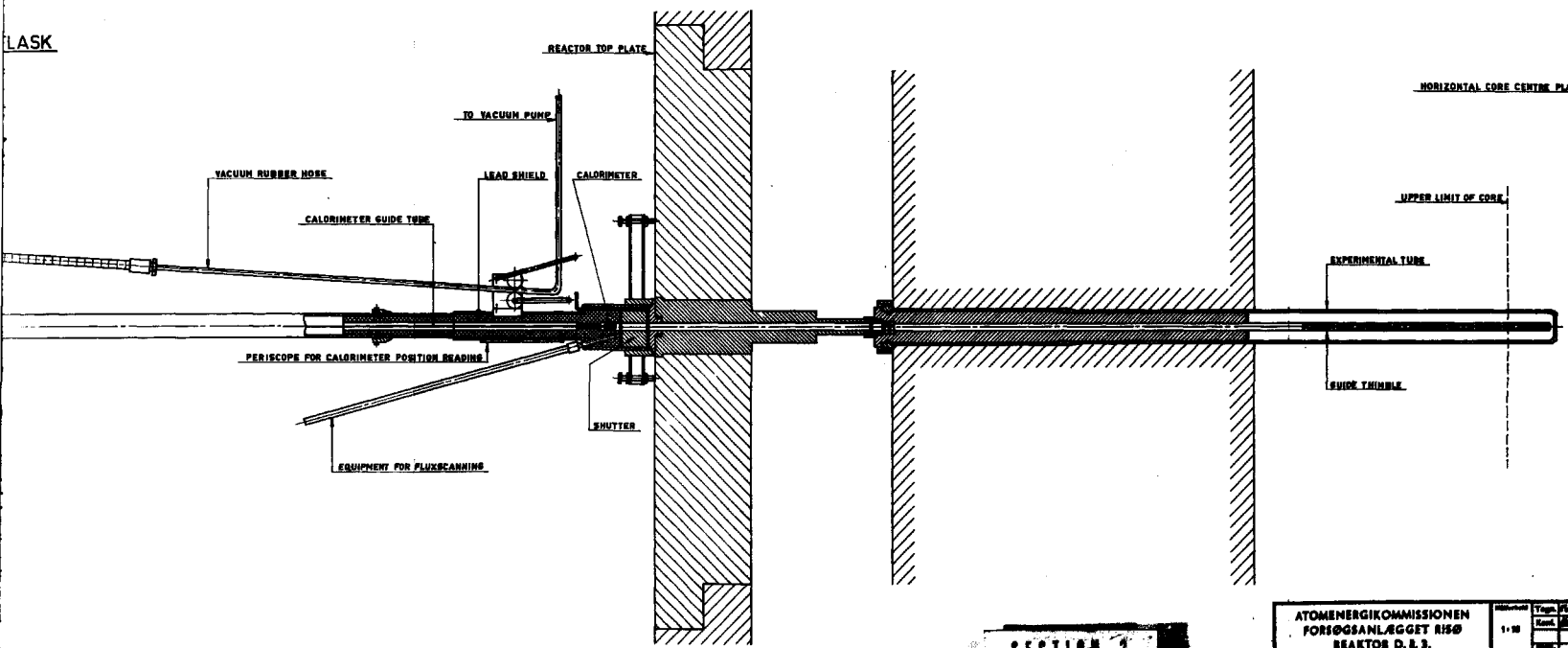

SECTION 2

ATOMENERGIKOMMISSIONEN
FORSØGSANLÆGGET RISØ
REAKTOR D. R. 3.

1:10

γ - CALORIMETER MEASUREMENT
ARRANGEMENT IN A 4V FACILITY.

28 - X - 854

Figure 10

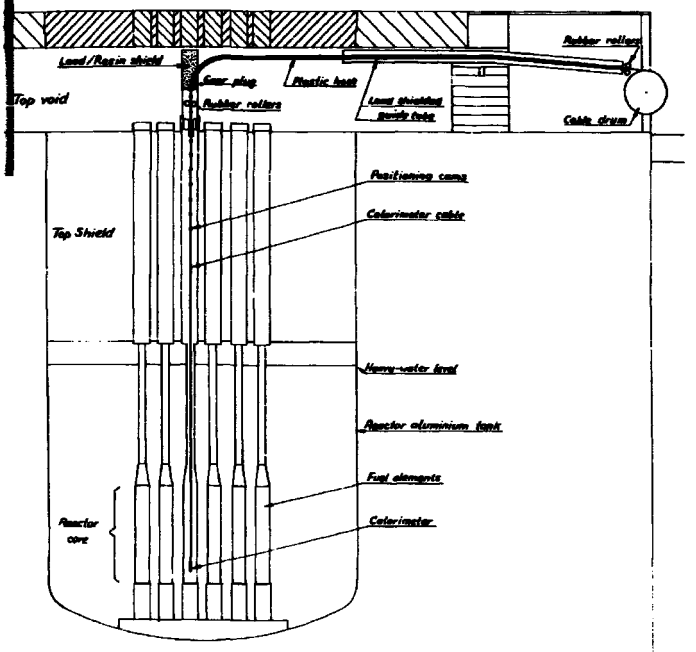

Calorimeter type I6. Arrangement for scanning in flux-scan tubes in Mk. II fuel elements and in flux-scan rigs in Mk. III and Mk. IV fuel elements.

from the gear plug.

The gear plug is shielded with 5 mm borax plate and 10 cm resin and lead.

2. SEPARATION OF NUCLEAR-HEAT DOSE-RATE COMPONENTS

2.1. Introduction

2.1.1. Survey of the Components

The nuclear heat released in a piece of material in a reactor consists of several components, which may be listed in groups as follows:

(A) Fission-Y

(B) Decay-Y and -β from fission products

(C) Capture-Y from nuclear reactions in the structure of fuel elements, control absorbers, experimental tubes, rigs and loops, coolant, moderator, reflector, and reactor tank

(D) Decay-Y and -β from nuclei created by the reactions mentioned under (C)

(E) Capture-Y from nuclear reactions in the material itself

(F) Decay-γ and -β from nuclei created by the reactions mentioned under (E)

(G) Elastic scattering of fast neutrons

(H) Inelastic scattering of fast neutrons.

2.1.2. The Ideal Dose. The Position Dose. Discussion

The I. C. R. V. convention[23] defines a dose named KERMA (Kinetic Energy Released in Matter) as the dose when the primary radiation is not attenuated and all the secondary radiation is absorbed in the material.

Linacre and Thomas[38] distinguish between the ideal dose, identical with the KERMA defined above, and the true dose. They define the primary radiation as the radiation incident on a sample, directly or indirectly ionizing, and the secondary radiation as the charged particles formed in the sample in its interaction with the primary radiation. The modified primary radiation resulting from this interaction they refer to as the scattered radiation.

If the results of the measurement of nuclear heat is used for estimation of the total heating in a rig or a structure element in a reactor, it is more convenient to split the dose-rate component in another way. The rig designer primarily wants to know the unperturbed radiation heating in that position in the core where he intends to install his rig, and to this figure, which is mostly characteristic of the position, he will add a calculated correction dependent on the materials of the rig.

The sum of the "position dose rate" and the "material dose rate" is now equal to the "true dose" as defined by Linacre and Thomas. The partition into position dose rate and material dose rate makes it possible to supply a set of heating rates based on the position dose rates for the experimental facilities of a certain reactor. These position dose rates are only dependent on the reactor power and the core configuration.

Referring to the list of radiation components in 2.1.1, we see that the position dose rate comprises the radiation doses A, B, C, and D, while the material dose rate accounts for the doses E, F, G, and H and the perturbation corrections to the position dose components.

The results of measurements of nuclear heat by means of the calorimeters A25 and J6 include the position dose rates as well as the material dose rates belonging to the specific calorimeter. In order to obtain the set of position factors of nuclear heating one must calculate the material dose rate components and perturbation corrections and subtract them from the measurement results. These calculations are carried out in the following part of section 2.

Some of the calculations can be verified by measurements. A few measurements of this kind have been made and more planned. The results and the comparisons between calculated and measured components in the dose separation will be issued later.

The correction calculation methods used in order to obtain the position dose rates from the calorimeter measurements are applicable also when a rig designer wants to calculate the true dose for a specific rig in one of the experimental facilities. The correction calculations are therefore described in detail and a guide for the utilization of the results for prediction of nuclear heat is given in section 4.

2.2. Thermal Neutron Capture

2.2.1. Thermal-Neutron Capture in the Structure

With an absorption cross section of an isotope constituting a part of a component in the calorimeter structure of

$$\Sigma_{ai} = \frac{M_{qi} \cdot \sigma_{ai} \cdot 0.602}{A_i} \text{ cm}^2, \quad (4)$$

where

M_{qi} = the mass of isotope "i" in the structure component q (grammes

σ_{ai} = the microscopic thermal-neutron absorption cross section (barns)

0.602 = Avogadro's number in units of 10^{-24}

A_i = atomic weight of the structure material, and at a thermal-neutron flux of φ_{th} n/cm^2 sec, the capture-Y source strength i

$$S_i = \Sigma_{ai} \cdot \varphi_{th} \cdot E_{bi}, \quad (5)$$

where E_{bi} is the mean binding energy released by thermal-neutron capture in the isotope "i".

Only a fraction of this source strength

$$S_i \cdot G_q$$

hits the sample, which only absorbs a fraction dependent on its linear energy-absorption coefficient μ_{eai}. Index "i" indicates that the μ-value corresponds to the level of the binding energy of the isotope "i".

Hence the heat in a mass unit of the sample due to capture-Y from the calorimeter structure is

$$\Delta W_{CSt} = \frac{1}{M_P} \sum_{q=1}^{Q} \sum_{i=1}^{I} (G_q \cdot S_i \cdot \mu_{eai}) \quad \text{MeV/sec} \cdot \text{g}, \quad (6)$$

where Q is the number of structure components, and I is the number of isotopes present in the structure. M_P is the sample mass.

In numerical calculations it is more practical to rearrange eq. (6) and convert MeV/sec into watts:

$$\Delta W_{CSt} = \frac{0.602}{6.24 \cdot 10^{12}} \cdot \frac{\varphi_{th}}{M_P} \sum_{q=1}^{Q} \sum_{i=1}^{I} (G_q \cdot M_{qi} \cdot \frac{\sigma_{ai}}{A_i} \cdot E_{bi} \cdot \mu_{eai}) \text{W/g}$$

$$= 9.65 \cdot 10^{-14} \cdot \frac{\varphi_{th}}{M_P} \sum_{q=1}^{Q} \sum_{i=1}^{I} (G_q \cdot \frac{M_{qi} \cdot \sigma_{ai}}{A_i} \cdot E_{bi} \cdot \mu_{eai}) \text{W/g} \quad (7)$$

The geometry factor G_{St} will be deduced for cylindrical geometries concentric to the sample and for plane structure elements perpendicular to the sample axis.

2.2.2. Geometry Factors

(a) Cylindrical Elements. It is assumed that the cylinder axis equals the sample axis. The cylinder Y-source strength is S monoenergetic photons per sec. If the cylinder mass were concentrated in a thin, cylindrical tube with radius R equal to the mean cylinder radius, the number of photons expelled from a ring with the axial length dx that hit a disc of the sample is (see fig. 2.2.2.1)

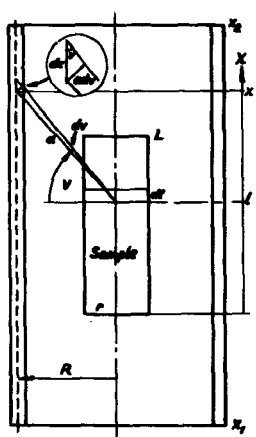

Fig 2.2.2.1

$$\frac{A}{4\pi a^2} \cdot \frac{Sdx}{(x_2-x_1)},$$

where a is the distance to the centre of the disc and A is the approximate apparent disc area seen from the cylinder ring:

$$A = \pi r^2 \sin v .$$

As the distance travelled in the disc by a photon penetrating the disc centre is dl/sin v, the energy deposition in the disc is

$$\frac{A}{4\pi a^2} \cdot \frac{Sdx}{(x_2-x_1)} \cdot \mu \cdot \frac{dl}{\sin v},$$

where μ is the linear absorption coefficient of the sample material for the energy of Y involved.

As $dx = adv/\cos v$

and $a = R/\cos v$,

the total energy deposition in the sample of gammas from the cylinder shell is

$$\mu S \cdot G = \int_0^L \int_{v_2}^{v_1} \frac{\pi \cdot r^2 \cdot \sin v \cdot S \cdot R/\cos v \cdot dv \cdot \mu \cdot dl}{4\pi \cdot (R/\cos v)^2 \cdot (x_2 - x_1) \cdot \cos v \cdot \sin v} \qquad (8)$$

$$\mu S \cdot G = \frac{r^2 \cdot S \cdot \mu}{4R(x_2 - x_1)} \int_0^L dl \int_{v_2}^{v_1} dv \quad (-\tfrac{\pi}{2} \leq v_1 \wedge v_2 \leq +\tfrac{\pi}{2}). \qquad (9)$$

As

$$v_1 = \text{Arc tg } \frac{x_1 - l}{R} \quad \text{and} \quad v_2 = \text{Arc tg } \frac{x_2 - l}{R}$$

and the solution of the integrals is

$$\int (\text{Arc tg } \frac{x-l}{R})\, dl = -R \int \text{Arc tg } u \, du = -R(u \text{ Arc tg } u - 1/2 \ln(1+u^2)),$$

where

$$u = \frac{x-l}{R}; \quad dl = -R\, du,$$

the geometry factor becomes

$$G = \frac{r^2}{4(x_2 - x_1)} (u_1 \text{ Arc tg } u_1 - u_2 \text{ Arc tg } u_2 - t_1 \text{ Arc tg } t_1 + t_2 \text{ Arc tg } t_2 + 1/2 \ln \frac{(u_2^2 + 1)(t_1^2 + 1)}{(u_1^2 + 1)(t_2^2 + 1)}, \qquad (10)$$

where

$$u_1 = \frac{x_1 - L}{R}, \quad u_2 = \frac{x_2 - L}{R}, \quad t_1 = \frac{x_1}{R}, \quad \text{and} \quad t_2 = \frac{x_2}{R}.$$

If the cylinder shell is "long in both directions", eq. (6) becomes

$$\mu SG = \frac{r^2 S \mu}{4R(x_2 - x_1)} \int_0^L dl \int_{-\frac{\pi}{2}}^{+\frac{\pi}{2}} dv = \frac{r^2 S \mu \pi L}{4R(x_2 - x_1)}.$$

Hence

$$G = \frac{r^2 \pi L}{4R(x_2 - x_1)} . \qquad (11)$$

If the cylinder shell is "long in one direction" only, eq. (6) becomes

$$\mu SG = \frac{r^2 S \mu}{4R(x_2 - x_1)} \int_0^L dl \int_{v_1}^{\frac{\pi}{2}} dv,$$

and by a similar deduction as before we obtain

$$G = \frac{r^2}{4(x_2 - x_1)} \left(u_1 \operatorname{Arc\,tg} u_1 - t_1 \operatorname{Arc\,tg} t_1 + 1/2 \ln \frac{t_1^2 + 1}{u_1^2 + 1} + \frac{\mu L}{2} \right). \qquad (12)$$

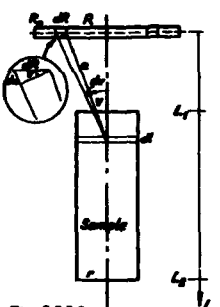

Fig. 2.2.2.2

(b) Plane Elements. This deduction deals with disc-type structure elements as shown in fig. 2.2.2.2. The sample axis is perpendicular to the circular disc and passes through its centre. The disc thickness is small compared with the distance to the sample. The disc γ-source strength is

$$\frac{S}{\pi R_o^2} \text{ photons/cm}^2 \text{ sec.}$$

The γ-source strength from a ring of the disc with the radius R and the radial thickness dR is

$$2\pi R\, dR \frac{S}{\pi R_o^2} = \frac{2S}{R_o^2} \cdot R \cdot dR.$$

The number of photons expelled from this ring to a disc of the sample at the distance l from the structure disc is

$$\frac{A}{4\pi a^2} \cdot \frac{2S}{R_o^2} R\, dR,$$

where the apparent area seen from the ring is

$$A = \pi r^2 \cos v.$$

As the distance travelled in the sample disc by a photon penetrating the disc centre is $dl/\cos v$, the energy deposition in the disc is

$$\frac{A}{4\pi a^2} \cdot \frac{2S}{R_o^2} R \cdot dr\mu \frac{dl}{\cos v},$$

where μ is again the linear absorption coefficient of the sample material for the energy of γ involved.

As $R = a \sin v$

and $dR = da/\sin v$,

the total energy deposition in the sample from the plane structure element is

$$\mu S G = \int_{L_1}^{L_2} \int_{a_1}^{a_2} \frac{\pi r^2 \cos v}{4\pi a^2} \frac{2S}{R_o^2} a \sin v \frac{da}{\sin v} \mu \frac{dl}{\cos v}$$

$$= \frac{S r^2}{2R_o^2} \int_{L_1}^{L_2} dl \int_1^{\sqrt{R_o^2+1^2}} \frac{1}{a} da = \frac{S r^2}{2R_o^2} \mu \int_{L_1}^{L_2} (\ln\sqrt{R_o^2+1^2} - \ln 1)dl .$$

The solution of the logarithmic integrals is

$$\int(\ln\sqrt{R_o^2+1^2})dl = 1/2 \int(\ln(R_o^2+1^2))dl = \frac{1}{2}\ln(R_o^2+1^2) - l + R \text{ Arc tg} \frac{1}{R_o}$$

$$\int \ln 1 \, dl = l \cdot \ln 1 - l.$$

Hence the geometry factor becomes

$$G = \frac{r^2}{2R_o^2}\left(\frac{L_2}{2}\ln\left(\left(\frac{R_o}{L_2}\right)^2+1\right) + R_o \text{ Arc tg} \frac{L_2}{R_o} - \frac{L_1}{2}\ln\left(\left(\frac{R_o}{L_1}\right)^2+1\right) - R_o \text{ Arc tg} \frac{L_1}{R_o}\right).$$

(13)

2.2.3. Thermal-Neutron Capture in the Sample

If we use the same symbols and the same deduction as in 2.2.1, the capture-γ from thermal-neutron reactions in a unit mass of the sample itself is

$$\Delta W_{CSp} = 0.65 \cdot 10^{-14} \frac{\varphi_{th}}{M_P} \sum_{i=1}^{I} \left(M_i \frac{\sigma_{ai} \cdot E_{bi}}{A_i} X_i \right) \quad W/g, \qquad (14)$$

where $X_i = f(\mu_{eai} \cdot \bar{l})$ is the fraction of the released energy that is absorbed in the sample. This capture probability has been calculated for infinite cylinders, slabs and spheres by Case, de Hoffmann and Placzek[4], and a diagram showing the results is given in fig. 14. The best approximation of the sample geometry is a sphere with the same weight as the sample. The radius of the equivalent is

$$\bar{l} = \sqrt[3]{\frac{3}{4} r^2 L},$$

where R and L are the radius and length of the cylindrical sample.

2.3. Decay of Activated Nuclei

2.3.1. The Decay-β Spectrum of Al^{28}

On the decay of a radioactive isotope a number of β-particles and photons of different energies are expelled. The photons usually posess usually fixed energies, while the energy distribution of the β-particles is continuous. In the following the relative frequency distribution function will be deducted. The β-decay of Al^{28} is chosen as an example as aluminium constitutes the most common element in the calorimeters.

On the decay from Al^{28} to Si^{28}, β-particles and neutrinos of energies ranging from zero to the maximum energy: 2.87 MeV, are emitted.

In relativistic units the number of β-particles expelled with the energy[2]

$$W = \frac{E(MeV)}{0.511} + 1 \qquad (0 \leq E \leq 2.87 \text{ MeV})$$

$$N(W) = K \cdot \eta \cdot W \cdot q^2, \qquad (15)$$

where

K is an arbitrary constant

η is the momentum of the neutrino

q is the momentum of the electron.

Figure 14

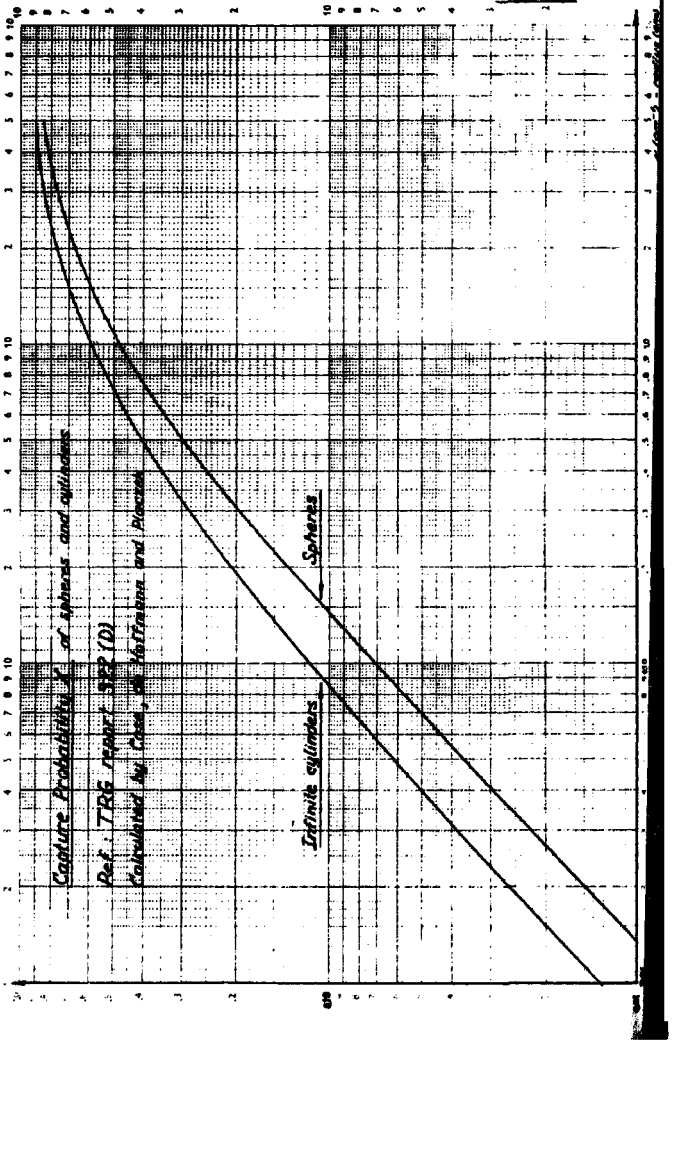
Capture Probabilities for infinite cylinders and spheres
Ref.: TR6 report: 382 (D)
Calculated by Case - de Hoffmann and Placzek
Infinite cylinders
Spheres

Figure 12

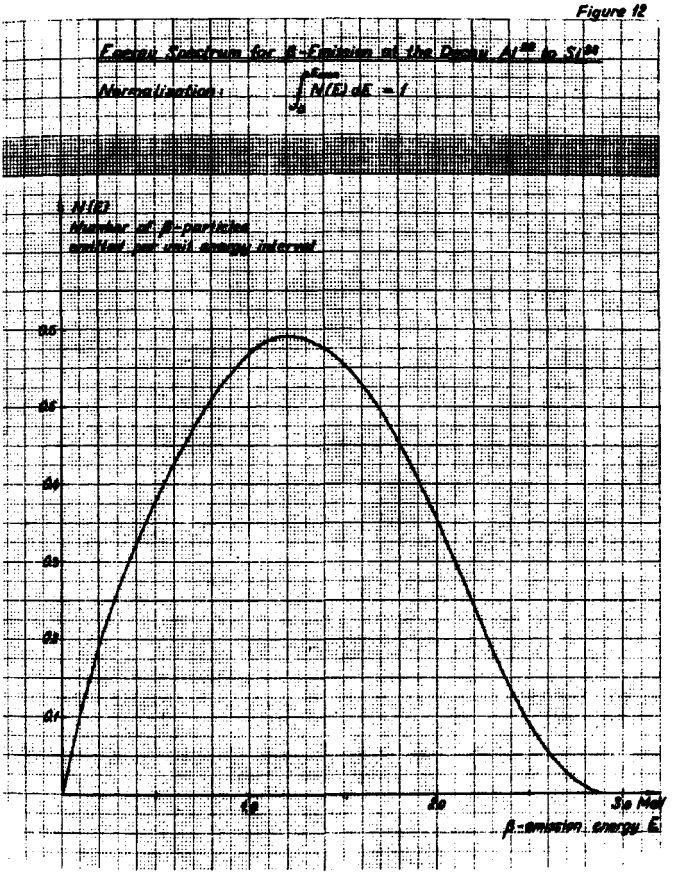
Energy Spectrum for β-Emission of the Decay Al^{28} to Si^{28}
Normalization: $\int_{E_0}^{E_{max}} N(E)\,dE = 1$
N(E)
Number of β-particles emitted per unit energy interval
0.5
0.4
0.3
0.2
0.1
1.0
2.0
3.0 MeV
β-emission energy E

As

$$\eta = W^2 - 1$$

and $q = W_o - W$,

(15) is transformed to

$$N(W) = K\sqrt{W^2 - 1} \cdot W(W_o - W)^2. \qquad (16)$$

K is determined by the normalization

$$\int_{W_1}^{W_o} N(W) = 1, \qquad \text{where} \quad \begin{cases} W_1 = \frac{0}{0.511} + 1 = 1 \\ W_o = \frac{2.87}{0.511} + 1 = 6.616. \end{cases}$$

As

$$\frac{1}{K} = \int_1^{6.616} \sqrt{W^2 - 1} \cdot W(W_o - W)^2 dW$$

$$= \left[\frac{1}{5}\sqrt{(x^2-1)^5} + (\frac{1}{3} - \frac{1}{2}W_o x + \frac{1}{3}W_o^2)\sqrt{(x^2-1)^3} - \frac{1}{4}W_o x\sqrt{x^2-1} + \frac{1}{4}W_o \ln|x + x^2 - 1| \right]_1^{6.}$$

we find

$$K = \frac{1}{377.27}$$

and in E - units

$$N(E) = \frac{1}{377.27} \cdot \frac{6.616-1}{2.87} \cdot \sqrt{(\frac{E}{0.511})^2 + \frac{2E}{0.511}} \, (\frac{E}{0.511} + 1)(\frac{2.87}{0.511} - \frac{E}{0.511})^2$$

$$= 0.07607 \sqrt{E^2 + 1.022\ E}\ (E^3 - 5.23\ E^2 + 5.31\ E + 4.21). \qquad (17)$$

The spectrum given by (17) is shown in fig. 12.

2.3.2. Decay of Nuclei Formed in the Structure

After some irradiation time an equilibrium between the formation of Al^{28}:

$$Al^{27}(n,\gamma)\,Al^{28},$$

and the decay of Al^{28}:

$$Al^{28} \rightarrow Si^{28} + \beta^- + \gamma$$

will be obtained.

The equilibrium concentration of Al^{28} is

$$A_o = \frac{\Sigma \Phi}{\lambda_A} ,$$

where

Σ = macroscopic activation cross section of Al^{28}

Φ = thermal-neutron flux

and λ_A = decay constant of Al^{28}.

Thus the concentration of Al^{28} will rise according to the exponential function

$$A_T = A_o (1 - e^{-\lambda A \cdot T}) . \qquad (18)$$

90% saturation is obtained after

$$T = - \frac{2.3}{0.693 T} \ln(1 - 0.90) = 7.64 \text{ min.}$$

As the adjustment of the measurement equipment generally lasts about 8 min, most of the measurements are made with an Al^{28} concentration close to the equilibrium value.

The heat deposition in the sample due to decay of a thermal-neutron activated isotope "i" with k modes of β-decay, is calculated by dividing each of the k β-energy spectra (see fig. 12) into j intervals and finding the fractional contribution of the mean energy $\bar{E}_j$ in each interval to the total energy release. The probability that the emission energy of a β-particle is within the interval Δ_j is

$N_j \Delta_j$,

where N_j is the β-spectrum ordinate: The number of β-particles expelled per unit energy interval.

Only a fraction of these β-particles will be absorbed in the sample. The geometry factors deduced in subsection 2. 2. 2 give the fractions of the total β-release that will be expelled in the direction of the sample. But a considerable part of this energy will be attenuated by the structure element itself and by other structure layers in between the sample and the element in question. If the penetration probability is called δ_{Sj}, the total heat deposition in the sample from β-decay in the structure will at equilibrium be (by analogy with 2. 2. 1):

$$\Delta W_{DSt\beta} = \sum_{q=1}^{Q} \sum_{i=1}^{I} \left(\frac{M_{qi} \cdot \sigma_{ai} \cdot 0.602 \cdot \varphi_{th}}{A_i \cdot 6.24 \cdot 10^{12}} \frac{G_q}{M_P} \sum_{k=1}^{K} N_k \sum_{j=1}^{J} (N_j \Delta_j E_j \delta_{Sj}) \right) W/g \qquad (19)$$

$$= 9.65 \cdot 10^{-14} \cdot \frac{\varphi_{th}}{M_P} \sum_{q=1}^{Q} \sum_{i=1}^{I} \left(G_q \frac{M_{qi} \sigma_{ai}}{A_i} \sum_{k=1}^{K} N_k \sum_{j=1}^{J} (N_j \Delta_j E_j \delta_{Sj}) \right) W/g.$$

δ_{Sj} is found by means of the following consideration:

If m structure layers surround the sample inside the structure element in question, *β-particles from this element* have to penetrate m + 1/2 layers on an average in order to hit the sample. The total effective thickness of the m + 1/2 layers is denoted t.

According to Glasstone[6] the average residual energy of a β-particle having penetrated an aluminium layer of the thickness t is

$$E_p = E_j - 5.00\, t - 0.278 \text{ MeV},$$

where the initial energy of the β-particle is E_j MeV.

Thus the penetration probability is

$$\delta_{Sj} = \frac{E_p}{E_j} = 1 - (5.00\, t + 0.278) \cdot \frac{1}{E_j} . \qquad (20)$$

The thickness t is the mean distance travelled by the photons through the layer in all relevant directions, dependent on the sizes of the sample and the structure element. If the mean direction is characterized by the angle v from the calorimeter axis, we have

$$t = t_c / \sin v,$$

where t_c is the perpendicular distance to the layer.

By calculation of the heat in the sample from γ-decay in the structure it is assumed that the photons are not attenuated. In general, the decay of an isotope "i" is accompanied by the emission of photons of several energies. The contribution from the k'th photon with the energy E_k and the probability of occurrence N_k when it hits the sample, which has a linear energy absorption coefficient μ_{eak} at the energy E_k, will be

$$N_k E_k \mu_{eak}.$$

Consequently the heat deposition in the sample from γ-decay in the structure will at equilibrium be (by analogy with 2.2.1)

$$\Delta W_{DSt\gamma} = \sum_{q=1}^{Q} \sum_{i=1}^{I} \left(\frac{M_{qi} \cdot \sigma_{ai} \cdot 0.602 \cdot \varphi_{th}}{A_i \cdot 6.24 \cdot 10^{12}} \cdot \frac{G_q}{M_P} \sum_{k=1}^{K} (N_k E_k \mu_{eak}) \right) \cdot \tag{21}$$

$$= 9.65 \cdot 10^{14} \frac{\varphi_{th}}{M_P} \sum_{q=1}^{Q} \sum_{i=1}^{I} \left(G_q \frac{M_{qi} \cdot \sigma_{ai}}{A_i} \sum_{k=1}^{K} (N_k E_k \mu_{eak}) \right) W/g.$$

By combination of eqs. (19) and (21) we find the total heat deposition in the sample due to decay of activated nuclei in the structure

$$\Delta W_{DSt} = 9.65 \cdot 10^{-14} \frac{\varphi_{th}}{M_P} \sum_{q=1}^{Q} \sum_{i=1}^{I} \left(G_{st} M_{st} D_i \sum_{k=1}^{K} N_k \left(\sum_{j=1}^{J} (N_j \Delta_j E_j b_{sj}) + E_k \mu_{eak} \right) \right) W/g. \tag{22}$$

2.3.3. Decay of Nuclei Formed in the Sample

The heat deposition in the sample caused by decay of activated nuclei in the sample itself is calculated as in subsection 2.3.2 by considering the k'th mode of decay of the isotope "i".

The ratio X_k of γ absorbed in the sample to that released in the sample is found as described in 2.2.3.

The corresponding ratio (1-d) of β absorbed in the sample to that released in the sample is calculated by means of a computer code: BETATAB, P. 400. The β-spectrum is divided into a number of intervals, and the code makes summations of the losses of β-energy from all mass units in the sample through all space angles and in all β-spectrum intervals. The code deals with finite cylindrical shapes. A further description is found in ref. 53.

As the BETATAB code computes the fractional loss denoted d of β-energy from the sample, the energy deposition in the sample is expressed by (1-d).

By analogy with eq. (22) the total amount of heat deposited in the sample as a consequence of decay of activated nuclei in the sample can be expressed as

$$\Delta W_{DS_p} = 9.65 \cdot 10^{14} \frac{\Phi_{th}}{M_p} \sum_{i=1}^{I} \left(\frac{M_i \sigma_{ai}}{A_i} \sum_{k=1}^{K} (1-d) N_k \left(\sum_{j=1}^{J} (N_j \Delta_j E_j) + E_k X_k \right) \right) W/g. \tag{23}$$

2.4. Fast Neutron Reactions

2.4.1. Elastic Scattering in the Sample

The mean energy transitio.. in an elastic collision of a neutron with the energy E and a nucleus with the mass number A is[6]

$$dW(E) = \frac{E}{2}\left(1 - \frac{(A-1)^2}{(A+1)^2}\right) = \frac{2EA}{(A+1)^2}. \tag{24}$$

Thus the heat generation by elastic scattering in a mass-unit material placed in a fast-neutron flux is

$$\Delta W_{ScE} = \frac{N}{A} \cdot \frac{2A}{(A+1)^2} \int_{E_1}^{E_2} \Phi(E) \sigma_S(E) E \, dE. \tag{25}$$

It is convenient to transfer the energy scale to a lethargy scale, defined by

$$du = d\left(\ln \frac{E_0}{E}\right) = -\frac{dE}{E} .$$

As

$$\Phi(u)\, du = -\Phi(E)\, dE,$$

we have

$$\Phi(u) = E\,\Phi(E).$$

Eq. (25) is now transformed to

$$\Delta W_{Sce} = \frac{2N}{(A+1)^2} \int_{u_1}^{u_2} \Phi(u)\, \sigma_S(u)\, du \quad \text{MeV/sec g.} \tag{26}$$

If $\Phi(u)$ is in units of 10^{14} n/cm^2 · sec, $\sigma_S(u)$ in barns and W in watts, we have

$$\Delta W_{Sce} = -\frac{19.32}{(A+1)^2} \int_{u_1}^{u_2} \Phi(u)\, \sigma_S(u)\, du \quad \text{W/g.} \tag{27}$$

The neutron spectra are shown in fig. 13. As the neutron spectra of DR 3 have not yet been measured, those in fig. 13 are based on Monte-Carlo calculations made by S. B. Wright for the British reactor PLUTO, which is similar to DR 3 (ref. 18). The spectra are valid for fuel elements and dummy elements, i. e. elements with the same geometric shape as fuel elements, but without uranium. The dashed extrapolation of the lower part of the dummy-element spectrum is the estimated trace of the spectrum in experimental facilities in the heavy water outside the core. Below 0.5 keV ($u = 10$) the spectrum is close to a 1/v-spectrum where u is constant.

Fig. 13 also shows a pure fission spectrum given by[9)]

$$S(E) = 0.484 \cdot 10^{14} \cdot e^{-E} \cdot \sinh\sqrt{2E}$$

or

$$S(u) = 0.484 \cdot 10^{14}\, e^{-(E_R \cdot e^{-u})} \sinh\sqrt{2\, E_R\, e^{-u}} \tag{28}$$

This spectrum is normalized to 10^{14} fission neutrons per sec as

$$\int_{\infty}^{0} S(u)\, du = \int_{0}^{\infty} S(E)\, dE = 10^{14} \text{ n/cm}^2 \text{ sec.}$$

The fast-neutron flux measurements in DR 3 are carried out by means of the threshold reaction

$$_{28}N^{58} (n, p) _{27}Co^{58}$$

with a mean activation cross section

$$\bar{\sigma} = 0.017 \text{ barns}$$

defined by

$$\int_0^\infty \sigma(E)\, S(E)\, dE = \bar{\sigma} \int_0^\infty S(E)\, dE. \qquad (29)$$

Above 3 MeV ($0 < u < 1.2$) the fission spectrum coincides with the fuel-element spectrum (see fig. 13) as nearly all neutrons here are birth neutrons. Thus the $\Phi(u)$ function illustrates the spectrum of the flux produced by the normalized fission flux 10^{14} n/cm^2·sec. As, according to eq. (29), the fission flux is determined by the $_{28}Ni^{58}$ threshold reaction, the $\Phi(u)$ function consequently gives the spectral distribution of a fast-neutron flux measured at 10^{14} n/cm^2 · sec by means of a $_{28}Ni^{58}$ foil.

2.4.2. Inelastic Scattering in the Sample

The energy of incident neutrons taking part in inelastic collisions in 1 gramme of $_{13}Al^{27}$ is

$$\Delta W_{Sci} = \frac{N}{A} \int_0^\infty \Phi(E)\, \sigma_{Si}(E) \cdot E \cdot dE \quad \text{MeV/sec} \cdot g$$

or

$$\Delta W_{Sci} = 0.3575 \int_0^{u_1} \varphi(u)\, \sigma_{Si}(u)\, du \ \text{W/g} \qquad (30)$$

for Al^{27} in a fission flux of 10^{14} n/cm^2 sec.

No inelastic scattering takes place when the energy of the incident neutron is below that of the lowest state above the ground state. The excited nucleus may expel one or more neutrons or a proton, a deuteron, and a-particle or other particles, but the threshold energies are in most cases greater than the energies of the most energetic neutrons of the fission spectrum in the fuel element. According to Howerton[84] the only reactions in Al^{27} with a threshold energy lower than 8 MeV are

Table 2.4.1

$_{13}Al^{27}$	Threshold energy (MeV)	Inel. scatt. cross section (barns)
(n, p)	1.8 (u_1 = 1.7)	0.10
(n, d)	6.0 (u_1 = 0.5)	~ 0
(n, α)	3.1 (u_1 = 1.2)	0.12
(n, n, γ)	2.5 (u_1 = 1.4)	0.80

2.5. Numerical Calculations

2.5.1. Dose-Rate Separation in A25/2

Table 2.5.1

Geometry factors for calorimeter A25/2. Cylindrical structure elements

Material		x_1 (cm)	x_2 (cm)	R (cm)	Mass M_{qi} (g)	Geometry factor G_q	$G_q \cdot M_{qi}$
Al	Heat shield, cylinder	-1.55	3.50	1.01	12.22	0.1015	1.240
	" " , top collar	2.90	3.53	0.91	0.47	0.0614	0.029
	" " , top tube	3.70	5.30	0.27	0.88	0.0236	0.021
	Vacuum sheath, cyl.	-2.40	6.10	1.20	8.56	0.0567	0.485
	" " , bottom collar	-2.40	-1.60	1.14	1.09	0.0191	0.021
	" " , bottom tube	-2.30	-1.75	0.14	0.11	0.0278	0.003
	" " , top collar	5.73	6.03	1.11	0.57	0.011	0.006
	" " , top tube	5.33	5.84	0.53	0.18	0.0118	0.002
	Supporting tube	5.33	5.84	0.45	76.34	$5.7 \cdot 10^{-4}$	0.043
	Guide thimble	-100	100	1.54	331	$46 \cdot 10^{-4}$	1.522
Cu	2 Cu cables	4.20	100	0.15	$2 \cdot 9.5$	$8.06 \cdot 10^{-4}$	0.015
SS	3 T/C cables	4.20	100	0.09	$3 \cdot 10.0$	$8.14 \cdot 10^{-4}$	0.024

Table 2.5.2

Geometry factors for calorimeter A25/2. Plane structure elements

Material		L_1 (cm)	L_2 (cm)	R_o (cm)	Mass M_{qi} (g)	Geometry factor G_q	$G_q \cdot M_{qi}$
Al	Heat sheath, bottom	1.60	4.10	0.93	0.68	0.033	0.023
	" " , top lid	1.10	3.60	1.00	0.99	0.049	0.048
	Vacuum sheath, bottom lid	1.90	4.40	1.10	0.76	0.025	0.019
	" " , top lid	3.30	5.80	1.08	0.79	0.011	0.017

For all aluminium structure parts we have

$$\Sigma G_q \cdot M_{qi} = 3.468.$$

Table 2.5.3

Spectra of binding energy E_{bi} and absorption coefficient μ_{eai} (aluminium)

E (MeV)	$N_i \Delta_i E_{bi}$ ($\Delta_i = 1$)	μ_{eai} cm^{-1}	$\mu_{eai}\ \bar{1}$	X_i	$N_i \Delta_i E_{bi} X_i$	$N_i \Delta_i E_{bi} \mu_{eai}$
0-1	0.216	0.0772	0.0677	0.0495	0.0107	0.0167
1-2	0.216	0.0671	0.0588	0.0435	0.0094	0.0145
2-3	0.369	0.0596	0.0522	0.0387	0.0143	0.0220
3-4	1.284	0.0554	0.0485	0.0360	0.0462	0.0711
4-5	1.675	0.0530	0.0465	0.0346	0.0579	0.0888
5-6	0.680	0.0514	0.0450	0.0335	0.0228	0.0350
6-7	0.531	0.0504	0.0441	0.0330	0.0175	0.0268
7-8	2.755	0.0498	0.0436	0.0325	0.0895	0.1371
Total					0.2683	0.4120

Thermal flux: $1 \cdot 10^{14}$ n/cm^2 sec

Sample mass: M_P = 8.59 grammes (incl. heater, Al_2O_3 and T/C's)

Sample absorption coefficient $\bar{\mu}_{eai}$ = 0.0534 cm^{-1}

Table 2.5.4

Material dose rate from thermal-neutron capture in the structure

Material	A_i	p_i	σ_{ai} (barn)	E_{bi} (MeV)	$\bar{\mu}_{eai}$ (cm^{-1})	$E_{bi} \cdot \bar{\mu}_{eai}$	$G_q \cdot M_{qi}$	ΔW_{CSt} (mW/g)
Al	27.0	1	0.23	-	-	0.4120	3.468	13.66
Cu^{63}	63.0	0.691	4.30	7.92	0.0534	0.4229	0.015	0.33
Cu^{65}	65.0	0.309	2.11	7.01	0.0534	0.3743	0.015	0.06
SS	55.4	1	2.92	8.14	0.0534	0.4347	0.024	0.61
Total								14.66 mW/g

The geometry factors are calculated for the A25 calorimeter, serial no. 2, as this calorimeter was used for the measurements reported in section 3. The geometrical dimensions are read from the X-ray photo and the drawings. Minor divergences may exist between A25/2 and later calorimeters in the same series although they are made from the same drawings.

The copper cables for the heaters and the thermocouple cables are treated as tubes with the same outside diameter as the cables, but with the cable mass concentrated in the tube wall.

The two stable isotopes Cu^{63} and Cu^{65} are weighted according to their natural abundance. The thermocouple sheaths are treated as if they were made of stainless steel 18/8/1 although this may not be the correct composition. Mean values of binding energies for the stainless steel and the copper isotopes are used, and so is the mean absorption coefficient for the sample referring to the aluminium binding-energy spectrum. These approximations are considered to be allowable in view of the small contributions from the cables to the total dose rate in the sample.

Fig. 14 is a copy of Placzek's diagram showing the capture probability X_i in spheres and infinite cylinders of photons released in the sphere or cylinder itself. The sphere equivalent to the sample has the radius

$$\bar{l} = \sqrt[3]{\frac{3}{4} 0.6^2} \cdot 2.5 = 0.877 \text{ cm.}$$

Mean value of the absorption coefficient:

$\bar{\mu}_{eai} = 0.0534\ cm^{-1}$.

Table 2.5.5

Capture probability of the sample

	$\bar{l}$ (cm)	$\bar{\mu}_{eai} \cdot \bar{l}$	X_i
Sphere equivalent	0.877	0.0468	0.0347
Infinite cylinder	0.60	0.0320	0.0405

For comparison the capture probability of the infinite cylinder with the same radius as the cylindrical sample is included in table 2.5.5.

Table 2.5.6

Material dose rate from thermal-neutron capture in the sample

Φ_{th} ($n/cm^2 \cdot sec$)	A	σ_a (barns)	$\sum_{n=i}^{I} N_i \Delta_i E_{bi} X_i$	ΔW_{CSp} (mW/g)
10^{14}	27	0.23	0.2683	22.1

The contributions from the sample thermocouples and heater to the sample heating are calculated to be less than 0.1 mW/g.

Table 2.5.7 presents the summations of β-energy depositions in the sample from decay in the structure elements calculated by means of eq. (22) in 2.3.2. The mean penetration angle of β-particles from outer structure elements is set at

$v = 60^{o}$.

The maximum range of β-particles in aluminium is 0.51 cm. Thus, only tube parts of the supporting tube and the heat-shield top tube up to this length are taken into account. The fraction of energy released in each energy interval: $N_j \Delta_j$, is read from the spectrum, fig. 12.

Table 2.5.1

Summation of β-contributions from decay in the structure

	t (cm)	Δ_j(MeV)	0-0.5	0.5-1.0	1.0-1.5	1.5-2.0	2.0-2.5	2.5-3.0	(a) $\sum_j N_j \Delta_j E_p$	(b) $G_q M_{qi}$	(a)x(b)
		E_j(MeV)	0.25	0.75	1.25	1.75	2.25	2.75			
		$N_j \Delta_j$	0.1070	0.2435	0.2802	0.2342	0.1083	0.0125			
Heat-shield cylinder	0.09	E_p	-	0.022	0.522	1.022	1.522	2.022			
		$N_j \Delta_j E_p$	-	0.005	0.151	0.239	0.165	0.025	0.585	1.340	0.725
Heat-shield top collar	0.05	E_p	-	0.222	0.722	1.222	1.722	2.222			
		$N_j \Delta_j E_p$	-	0.054	0.209	0.286	0.187	0.028	0.764	0.029	0.022
Heat-shield top tube	0.25	E_p	-	-	-	0.222	0.722	1.222			
		$N_j \Delta_j E_p$	-	-	-	0.052	0.078	0.015	0.145	0.021	0.003
Heat-shield top lid	0.09	E_p	-	0.022	0.522	1.022	1.522	2.022			
		$N_j \Delta_j E_p$	-	0.005	0.151	0.239	0.165	0.025	0.585	0.049	0.028
Heat-shield bottom	0.06	E_p	-	0.172	0.672	1.172	1.672	2.172			
		$N_j \Delta_j E_p$	-	0.042	0.185	0.274	0.181	0.027	0.710	0.023	0.017
Vacuum-sheath cylinder	0.21	E_p	-	-	-	0.422	0.922	1.422			
		$N_j \Delta_j E_p$	-	-	-	0.099	0.100	0.018	0.217	0.485	0.105
Vacuum-sheath top lid	0.20	E_p	-	-	-	0.472	0.972	1.472			
		$N_j \Delta_j E_p$	-	-	-	0.111	0.105	0.018	0.234	0.017	0.004
Vacuum-sheath top collar	0.08	E_p	-	0.072	0.572	1.072	1.572	2.072			
		$N_j \Delta_j E_p$	-	0.018	0.166	0.251	0.170	0.026	0.631	0.006	0.004
Vacuum-sheath bottom collar	0.08	E_p	-	0.072	0.572	1.072	1.572	2.072			
		$N_j \Delta_j E_p$	-	0.018	0.166	0.251	0.170	0.026	0.631	0.021	0.013
Vacuum-sheath bottom	0.16	E_p	-	-	0.172	0.672	1.172	1.672			
		$N_j \Delta_j E_p$	-	-	0.050	0.157	0.127	0.021	0.355	0.019	0.007
Supporting tube	0.25	E_p	-	-	-	0.222	0.722	1.222			
		$N_j \Delta_j E_p$	-	-	-	0.052	0.078	0.015	0.145	0.006	0.001
Guide thimble	0.31	E_p	-	-	-	-	-	0.422	0.922		
		$N_j \Delta_j E_p$	-	-	-	-	0.046	0.012	0.058	1.095	0.064
Total											0.993

The heating from the decay gammas is calculated by means of the geometry factors from tables 1 and 2. On each disintegration one photon with the energy 1.78 MeV is released, and the corresponding absorption coefficient for the aluminium sample is 0.0645 cm^{-1}.

The mineral-insulated cables with copper and stainless-steel (CrNi) sheaths contribute very little to the decay heating of the sample. Only the Cu^{65} isotope has a sufficiently short half-life to attain saturation, but with a cross section of 2.3 barns, a natural abundance of 30.9% and a very small geometry factor, its contribution is negligible.

Table 2.5.8

Material dose rate from Al^{28} decay in the structure

	Material	A_i	σ_{ai}	$\sum_{k=1}^{K} N_k E_k$	μ_{eak}	$G_q M_{qi}$	Total of table 2.5.7	ΔW_{DSt} (mW/g)
β	Al	27.0	0.23	-	-	-	0.993	9.5
γ	Al	27.0	0.23	1.78	0.0645	3.468	-	3.8

Heating of the sample by Al^{28} decay in the sample itself is calculated from eq. (23) in 2.3.3. The fractional loss of energy by escaping β-particles is calculated with the computer code BETATAB for a sample with the radius 0.6 cm and the length 2.5 cm to be 8.7%. The γ-capture probability X_k is read from fig. 14 for a sphere approximation as before, radius 0.877 cm, and a linear energy absorption coefficient of $\mu = 0.0645\ cm^{-1}$, which gives $X_k = 0.042$.

Table 2.5.9

Material dose rate from Al^{28} decay in the sample

	Material	A	σ_a (barns)	(1-d)	X_k	$\sum_{j=1}^{J} N_j \Delta_j E_j$	E_k	ΔW_{DSt} (mW/g)
β	Al	27.0	0.23	0.913	-	1.26		94.6
γ	Al	27.0	0.23	-	0.042	-	1.78	6.1

Table 2.5.10

Fast-neutron elastic scattering in fuel and dummy elements

u	Δu	σ_g (barns)	Φ(u) normalized to 10^{14} W/cm^2·s		d(ΔW_{Sce})	
			Fuel elem.	Dummy el.	Fuel elem.	Dummy el.
0	0.5	1.7	0.015	0.003	0.00031	0.00006
0.5	0.5	2.1	0.093	0.032	0.00240	0.00083
1.0	0.5	2.5	0.303	0.090	0.00933	0.00277
1.5	0.5	2.92	0.488	0.138	0.01758	0.00496
2.0	0.5	3.25	0.453	0.123	0.01812	0.00492
2.5	0.5	3.50	0.391	0.085	0.01685	0.00366
3.0	0.5	3.68	0.367	0.091	0.01663	0.00413
3.5	0.5	3.81	0.354	0.123	0.01661	0.00577
4.0	0.5	5.30	0.346	0.150	0.02258	0.00979
4.44	0.37	6.50	0.340	0.170	0.02014	0.01007
4.70	0.15	15.0	0.338	0.181	0.01873	0.01003
4.83	0.12	2.4	0.336	0.184	0.00238	0.00130
5.04	0.31	1.5	0.334	0.192	0.00382	0.00220
5.35	0.30	3.0	0.332	0.200	0.00736	0.00443
5.61	0.22	22.0	0.330	0.204	0.03934	0.02433
5.79	0.15	1.1	0.329	0.208	0.01337	0.00085
6.06	0.38	0.55	0.328	0.212	0.00189	0.00109
6.5	0.5	1.03	0.326	0.218	0.00413	0.00276
7.0	0.5	1.31	0.325	0.223	0.00525	0.00360
7.5	0.5	2.0	0.323	0.227	0.00796	0.00559
8.0	0.5	1.4	0.321	0.230	0.00554	0.00397
8.5	0.5	1.4	0.320	0.232	0.00552	0.00400
9.0	0.5	1.4	0.319	0.234	0.00550	0.00404
9.5	0.5	1.4	0.318	0.235	0.00549	0.00405
10.0	0.5	1.4	0.318	0.236	0.00549	0.00407
				ΔW_{Sce}	0.26009 W/g	0.12327 W/g

The heating by decay of isotopes produced from Cr and Ni in the sample thermocouples and heater is calculated roughly to be less than 0.1 mW/g.

Heating of the sample by fast-neutron elastic scattering is calculated by means of eq. (29) in 2.4.1. The lethargy scale from u = 0 to u = 10.25 is divided into 25 intervals, and the integral in eq. (29) is transformed into a summation of the flux and the scattering cross section in these 25 intervals. The calculations are shown in table 2.5.10 for fuel elements and dummy elements. The heating in experimental facilities outside the core is obtained by means of the column for dummy-element heating, as the flux spectra are identical down to u = 3. The remaining values for the experimental facilities in reflector positions are shown in table 2.5.10a.

Table 2.5.10a

Fast-neutron elastic scattering in reflector positions

u	Δu	σ_s (barns)	$\Phi(u)$ (n/cm^2 sec)	$d(\Delta W_{Sce})$ (mW/g)
0	0.5	1.7	-	-
0.5	0.5	2.1	-	-
1.0	0.5	2.5	-	-
1.5	0.5	2.92	0.000	0.0
2.0	0.5	3.25	0.010	0.40
2.5	0.5	3.50	0.049	2.54
3.0	0.5	3.68	0.087	3.94
$\sum_{n=0}^{3.0} \Delta W_{Sce}$ =				6.88 mW/g

From table 2.5.10 (dummy elem.) we have $\sum_{n=3.0}^{10.25} \Delta W_{Sce} = 101.94$ mW/g.

The energy of thermal neutrons corresponds to u = 18.0. The heating by elastic scattering of neutrons in the 1/v part of the spectrum from u = 10.25 to u = 18.0 is

Fuel elements: $\sum_{u=10}^{18} \Delta W_{Sce} = -\frac{19.32}{(A+1)^2} \cdot \overline{\Phi(u)} \cdot \overline{\sigma_s(u)} \cdot \Delta u$

$$= \frac{19.32}{(27+1)^2} \cdot 0.300 \cdot 1.400 \cdot (18.0-10.25) = \underline{80.2\,mW/g}$$

Dummy elements and reflector positions: $\sum_{u=10}^{18} \Delta W_{Sce} = \frac{19.32}{(27+1)^2} \cdot 0.260 \cdot 1.40 (18.0-10.25) =$ 69.5 mW/g

Table 2.5.11

Material dose rate from fast-neutron elastic scattering

u-interval	0-3	3-10.25	0-10.25	10.25-18	Total
Fuel elements (W/g)	-	-	0.2601	0.0802	0.3403
Dummy elements (W/g)	-	-	0.1233	0.0695	0.1928
Reflector positions (W/g)	0.0069	0.1019	-	0.0695	0.1783

The inelastic scattering reactions are merely important in fuel elements as only a small number of the neutrons present in dummy elements and reflector facilities have energies in excess of the inelastic-scattering threshold energies.

The attenuation probability of the scattered particles from the sample is denoted X in table 2.5.12, where the contributions from the reactions listed in table 2.4.1 are calculated by means of eq. (27) in 2.4.2. Mean values of the flux are obtained by integration of the spectrum for fuel elements in fig. 13.

Table 2.5.12

Material dose rate in Al^{27} from fast-neutron inelastic scattering

Reaction	u_1	$\overline{\phi(u)}$ 10^{14} n/cm^2 sec	σ_{Si} (barns)	X	ΔW_{Sci} (W/g)
(n, p)	1.7	0.250	0.10	~1.0	0.015
(n, d)	0.5	0.049	~ 0.00	~1.0	~0
(n, α)	1.2	0.143	0.12	~1.0	0.007
(n, n, γ)	1.4	0.197	0.80	~0.05	0.004
Total					0.026 W/g

The calculation of the heat from inelastic scattering reactions is rather uncertain because the parameters are not well known. But as the nuclear heat in a core position is of the order of 2 W/g and the fast flux is about $0.5 \cdot 10^{14}$ n/cm^2 sec, the inelastic-scattering contribution is only

$$\frac{0.026 \cdot 0.5 \cdot 100}{2} = 0.65\%;$$

so the uncertainties will be of no significance.

Summary of dose rate separation calculations for A25/2:

Table 2.5.13

Material dose rates from a thermal-neutron flux of 10^{14} n/cm^2 sec

Thermal-neutron capture in the structure	14.5 mW/g
- - - - - sample	22.1 -
β-decay in the structure	9.5 -
γ- - - - -	3.8 -
β- - - - sample	94.6 -
γ- - - - -	6.1 -
Total	150.6 mW/g

Table 2.5.14

Material dose rates from a fast-neutron flux of 10^{14} n/cm^2 sec

	Fuel element	Dummy element	Reflector pos.
Elastic scattering	340.3 mW/g	192.8 mW/g	178.3 mW/g
Inelastic -	26 -	0 -	0 -
Total	366 mW/g	193 mW/g	178 mW/g

2.5.2. Dose-Rate Separation in J6

As for the A25 calculations, a specific J6 calorimeter with serial no. 9 is chosen as model for the calculations although only minor differences exist between the J6 calorimeters. The calculations below are based on the drawing (fig. 3) and the X-ray photo of J6/9 (fig. 5). The sample size is: L = 3.55 cm; r = 0.2 cm.

Table 2.5.15

Geometry factors for cylindrical structure elements

Material	Object	x_1 (cm)	x_2 (cm)	R (cm)	Mass M_{qi} "(g)"	Geometry factor G_q	$G_q \cdot M_{qi}$
Al	Outer sheath	-0.20	+3.70	0.30	3.97	0.0811	0.322
Al	Sheath tip, cyl. part	-1.00	-0.20	0.23	0.406	0.0175	0.007
Al	Cable collar	-2.3	-1.4	0.23	0.139	0.0041	0.001
Al	100 cm flux scan tube	- 50	+ 50	0.45	8.357	0.00248	0.021
SS	20 cm T/C cables	0.7	20.00	0.22	5.265	0.00080	0.004

The heat-sink end of the rod is split into six discs perpendicular to the axis. Disc no. 1 is the part of the rod between the shortest T/C and the heat sink.

Table 2.5.16

Geometry factors for plane structure elements

Material	Disc. no.	Object	L_1 (cm)	L_2 (cm)	R_o (cm)	Mass M_{qi} (grams)	Geometry factor G_q	$G_q \cdot M_{qi}$
Al	1	Rod end	0.080	3.620	0.20	0.0485	0.0766	0.0037
	2	Heat sink	0.238	3.788	0.31	0.1400	0.0379	0.0045
	3	- -	0.388	3.938	0.31	0.1200	0.0210	0.0025
	4	- -	0.538	4.088	0.31	0.1200	0.0152	0.0018
	5	- -	0.688	4.238	0.31	0.1175	0.0117	0.0014
	6	- -	0.800	4.350	0.33	0.1174	0.0099	0.0011
	7	Cable collar disc	1.038	4.588	0.32	0.3002	0.0073	0.0022
	8	Outer sheath tip	1.200	4.750	0.23	0.1796	0.0062	0.0011

For all aluminium parts in J6/9 we have

$$\Sigma G_p \cdot M_{qi} = 0.317$$

The sample of the calorimeter is defined as the rod between the free end and the T/C junction at the heat-sink end.

Mass of sample (incl. heater and T/C cable): 1.334 g.

Sample absorption coefficient $\bar{\mu}_{eai} = 0.0534\ cm^{-1}$.

Thermal flux: $1 \cdot 10^{14}\ n/cm^2 \cdot sec.$

Table 2.5.17

Material dose rate from thermal-neutron capture in the structure

Material	A_i	P_i	σ_{ai} (barns)	E_{bi} (MeV)	$\bar{\mu}_{eai}$ (cm^{-1})	$E_{bi} \cdot \bar{\mu}_{eai}$	$G_q \cdot M_{qi}$	ΔW_{CSt} (mW/g)
Al	27.0	1	0.23	-	-	0.4120	0.317	8.1
SS	55.4	1	2.93	8.14	0.0534	0.4347	0.004	0.7
Total								8.8

Table 2.5.18

Spectra of binding energy E_{bi} and absorption coefficient μ_{esi}

E (MeV)	$N_i\Delta_i E_{bi}$ (Δ_i=1)	$\mu_{esi}(cm^{-1})$	$\mu_{esi}\bar{l}$	X_i	$N_i\Delta_i E_{bi}X_i$
0-1	0.216	0.0772	0.01544	0.0200	0.00432
1-2	0.216	0.0671	0.01342	0.0175	0.00378
2-3	0.369	0.0596	0.01192	0.0155	0.00572
3-4	1.284	0.0554	0.01108	0.0144	0.01849
4-5	1.675	0.0530	0.01060	0.0138	0.02312
5-6	0.680	0.0514	0.01028	0.0134	0.00911
6-7	0.531	0.0504	0.01008	0.0131	0.00696
7-8	2.755	0.0498	0.00996	0.0129	0.03554
Total					0.1070

The sample capture probability X_i is read from Placzek's diagram, fig. 14, for an infinite cylinder with the radius $\bar{l}$ = 0.2 cm.

Table 2.5.19

Material dose rate from thermal-neutron capture in the sample at a thermal flux of 10^{14} n/cm^2 sec

Material	A	σ_a (barns)	$\sum_{n=i}^{I} N_i\Delta_i E_{bi}X_i$	ΔW_{CSp} (mW/g)
Al	27	0.23	0.1070	8.8
SS(T/C's)	55.4	2.92	0.1498	9.5
Total				18.3

The material dose rate from SS in table 2.5.19 is weighted with the ratio between the mass in which the binding energy is released: 0.167 g (the mass of the T/C's) and the mass in which the energy is absorbed: 1.3337 g (the sample mass).

Table 2.5.20

Summation of β-contributions from decay in the structure

	l (cm)	Δ_j(MeV)	0-0.5	0.5-1.0	1.3-1.5	1.5-2.0	2.0-2.5	2.5-3.0	(a)	(b)	(a)-(b)
		E_j(MeV)	0.25	0.75	1.25	1.75	2.25	2.75	$\sum_j H_j \Delta_j E_{pj}$	$G_s \cdot H_{sj}$	
		$H_j \Delta_j$	0.1670	0.2625	0.2882	0.2362	0.1663	0.0625			
Outer sheath	0.035	E_{pj}	-	0.297	0.797	1.297	1.797	2.297			
		$H_j \Delta_j E_{pj}$		0.072	0.229	0.306	0.186	0.029	0.831	0.322	0.309
Sheath tip, cyl. part	0.25	E_{pj}	-	-	-	0.222	0.722	1.222			
		$H_j \Delta_j E_{pj}$				0.052	0.076	0.015	0.145	≈ 0.007	0.008
Flux scan tube	0.10	E_{pj}	-	-	0.472	0.972	1.472	1.972			
		$H_j \Delta_j E_{pj}$			0.137	0.229	0.150	0.025	0.569	0.0165	0.010
End end (disc no. 1)	0.05	E_{pj}	-	0.072	0.372	0.872	1.372	2.072			
		$H_j \Delta_j E_{pj}$		0.018	0.106	0.251	0.170	0.035	0.631	0.0080	0.009
Heat sink (disc no. 2)	0.26	E_{pj}	-	-	0.650	0.300	1.650	1.000			
		$H_j \Delta_j E_{pj}$			0.015	0.129	0.114	0.019	0.277	0.0027	0.003
Heat sink (disc no. 3)	0.4	E_{pj}	-	-	-	-	-	0.472			
		$H_j \Delta_j E_{pj}$						0.035	0.009	0.0060	0.003
Heat sink (disc no. 4)	0.35	E_{pj}	-	-	-	-	-	-			
		$H_j \Delta_j E_{pj}$							0	0.0045	0.000
Outer sheath tip	0.2	E_{pj}	-	-	-	0.672	0.972	1.472			
		$H_j \Delta_j E_{pj}$				0.110	0.105	0.018	0.233	0.0035	0.000
Total											0.369

The heating from β-decay in the structure is calculated in table 2.5.20. The mean penetration angle is set at $\nu = 45^{\circ}$ for cylindrical elements. As the maximum range in aluminium of the 2.87 MeV β-particles is 0.51 cm, the geometry factor G_s for the flux scan tube only refers to the 6 cm long centre part. The outer heat-sink discs and cable do not contribute to the β-decay heating for the same reason.

Table 2.5.21

Material dose rate from Al^{28}-decay in the structure

	Material	A_i	σ_{ai} (barns)	$\sum_{k=1}^{K} N_k E_k$	μ_{eak}	$G_q \cdot M_{qi}$	Total of table 2.5.20	ΔW_{DSt} (mW/g)
β	Al	27.0	0.23	-	-	-	0.238	17.4
Y	Al	27.0	0.23	1.78	0.0645	3.468		2.6

The computer code BETATAB is used to calculate the fractional loss of energy by escaping β-particles: 12.27%. The probability of Y-capture from the cylindrical sample is read from fig. 14: X_k = 0.0171.

The rates of heating by decay of the stainless-steel sheaths of the thermocouples in the sample are weighted with the ratio between the thermocouple masses: 0.167 g, and the sample mass: 1.3337 g.

Table 2.5.22

Material dose rate from decay in the sample

	Material	A	Abundance P	σ_a (barns)	1-d	$\sum_i n_j E_j \Delta_j$ (MeV)	$\Delta W_{DSpβ}$ (mW/g)
Decay β	Al	27.0	100	0.23	0.8773	1.26	90.9
Decay β	Cr^{54}(20%)	52.0	2.38	0.38	1.0	1.14	0.2
Decay β	Ni^{64}(80%)	58.7	1.16	1.6	1.0	0.605	0.2
					X_k	$\sum_k n_k E_k \Delta_k$	ΔW_{DSpY} (mW/g)
Decay Y	Al	27.0	100	0.23	0.0171	1.78	2.5
Decay Y	Cr^{54}(20%)	52.0	2.38	0.38	-	~ 0	~ 0
Decay Y	Ni^{64}(80%)	58.7	1.16	1.6	0.0171	0.586	~ 0

The heating from fast-neutron scattering and reactions is calculated for the adiabatic calorimeter A25/2 in 2.5.1. As the sample material is the same in the two types of calorimeters, the calculations are applicable also to the isothermal calorimeter J6/9.

Summary of dose-rate separation calculations for J6/9:

Table 2.5.23

Material dose rates from a thermal-neutron flux of 10^{14} n/cm^2 sec

Thermal-neutron capture in the structure	9.9 mW/g
Thermal-neutron capture in the sample	18.3 -
β-decay in the structure	17.4 -
γ-decay in the structure	2.6 -
β-decay in the sample	91.3 -
γ-decay in the sample	2.5 -
Total	142.0 mW/g

Material dose rates from a fast-neutron flux of 10^{14} n/cm^2 sec: the same as in 2.5.14.

3. MEASUREMENTS AND RESULTS

3.1. Scannings of Experimental Facilities 7V-, 4V- and 4VGR by Means of Calorimeter A25

3.1.1. Methods and Techniques

Nuclear-heat measurements can be carried out in an experimental hole provided with the plugs and guide tube belonging to the measurement equipment. As no more than two sets of equipment have been made, namely one set for the 7V holes and one for the 4V and 4VGR holes, only two holes can be scanned every four weeks of the reactor operation period.

When the flask is placed on top of the hole as shown in fig. 8, the vacuum in the calorimeter and the electronics are checked. The vacuum should be kept below 10^{-3} Torr.

The calorimeter is lowered by means of the hand wheel on the flask, and it is placed in the correct position by observing the marks on the calorimeter supporting tube through the periscope. Marks are made for every 10 cm on the supporting tube.

As soon as the nuclear heat starts to raise the sample temperature, power is switched on manually to the heat-shield heater and adjusted until the delta temperature between sample and heat shield is close to zero. Then the power is switched over to automatic control which keeps the delta temperature below 0.1 °C while the sample temperature increases from room temperature to about 225 °C. Then the heat-shield power is switched off, and the calorimeter is withdrawn into the flask again.

The recorded trace shows that the sample temperature increases nearly linearly with time. Full-scale deflection of the recorder equals a rise in temperature of 9.835 °C. Thus the backed-off voltage has to be changed about twenty times during one measurement, giving about twenty linear trace parts on the Graphispot recorder paper.

The slopes of the twenty trace parts differ from each other because

(1) the specific heat of the sample changes with temperature (see fig. 17),

(2) the thermocouple sensitivity changes with temperature (see fig. 16), and

(3) the contribution to the sample heating from the decay of activated nuclei changes as the degree of saturation of the activated isotopes changes.

The predominant activation process: Al 27 (n, γ) Al 28 with a half life of 2.3 minutes for the Al 28 isotope is saturated by about 98% in 10 minutes (see 2.3.1), which is the shortest time experienced for a measurement run. Consequently it was preferred to refer to the saturation condition. The slope was then read from the last temperature trace parts and in the calculations was used the appropriate data for specific heat and thermocouple sensitivity referring to the upper part of the temperature range, usually around 200 °C.

A complete scanning of an experimental hole comprised about ten measurements made at locations with 5 - 10 cm vertical distance and lasted two to five hours. Thermal- and fast-flux scannings by Co- and Ni-wires mounted in Al-wires were made through the flask in continuation of the nuclear-heat measurement.

3.1.2. Calibrations

3.1.2.1. Calibration of A25/2 as Adiabatic Calorimeter. With a specific heat c cal/^{o}C g of the calorimeter sample and a measured temperature rise rate dT/dt ^{o}C/sec, the heat deposition in the sample is

$$W = 4.1868 \cdot c \cdot dT/dt \ W/g. \qquad (33)$$

The value of c can be determined by calculation or by calibration.

The calibration method is preferable as faults in the temperature measuring device are eliminated if the device is used at the calibrations as well as at the in-pile measurements.

Ideally, the calibration should be made under exactly the same conditions as the in-pile measurements, i.e. with

(1) the same temperature of the surroundings,

(2) a uniform heat deposition in every part of the sample and structure, and

(3) the same conditions of heat conduction to the surroundings.

The surrounding temperature can be kept constant with an oven, but out-of-pile simulation of the two last conditions is rather difficult because the heat is produced by the electrical heater coils on the sample and the inner can, and this will rise the temperature gradients in the sample as well as in the can and the remaining structure, introducing errors which are bigger, the faster the temperature transient.

Therefore two types of out-of-pile calibrations were carried out, the first one simulating the in-pile conditions as well as possible within the limitations outlined above, and the second one without electrical power on the can heater.

The first type of calibration was carried out in the following way: By means of a network as shown in fig. 7 and described in 1.5.1 a current was sent through the sample heater-coil. The current was measured by means of "PYE" potentiometer across a precision 1 Ω shunt in the circuit. The can-heater-coil current was adjusted manually until the delta temperature between sample and can was steady close to zero. Then the automatic control was switched on, keeping the delta temperature below 0.1 ^{o}C during the calibration run. The linear sample temperature increased, and the delta temperature was recorded and the run stopped when the can heater

current had increased to the maximum out-put of the amplifier, 1 ampere, so that the delta temperature could no longer be kept below 0.1 °C. The calibration was repeated with different sample-coil currents and different surrounding temperatures.

The calibration result is the value of c and its dependence on the temperature. c is found from the electrical power $r_T \cdot I_T^2$ on the sample and the sample temperature slope $(dT/dt)_T$, all referring to the same sample temperature T

$$c = \frac{r_T \cdot I_T^2}{4.1868 \cdot (dT/dt)_T \cdot M_p} \text{cal}/^\circ\text{C} \cdot \text{g}. \tag{34}$$

The second type of calibration was made in the following way: With all parts of the calorimeter at the same temperature and in a constant surrounding temperature, a minor transient was made by switching a small electric current on to the sample heater-coil. The sample temperature rises and tends to reach an equilibrium value (see fig. 15) where the total of the applied electric heat would be led through the air gap to the inner can. The value of c could be found from the initial slope of the sample temperature, but the slope was rather uncertain here because the sample temperature was disturbed at that moment by small transients during the setting of the temperature gradients in the sample.

Before the sample temperature had reached its equilibrium value, the electric current on the sample heater was switched off, and the sample temperature decreased again. The sample temperature T and the sample-can delta temperature ΔT recorded during the calibration are shown in fig. 15.

The heat balances are:

Increasing sample temperature: $W_{el} - (W_{cond})_{\Delta T} = C \cdot dT/dt$ (35)

Decreasing sample temperature: $-(W_{cond})_{\Delta T} = C \cdot dT/dt$, (36)

where $W_{el} = r_T \cdot I_T^2$,

and $(W_{cond})_{\Delta T}$ is the heat conducted from the sample to the surroundings when the temperature difference between sample and can is ΔT °C. C is the sample heat capacity:

$$C = 4.1868 \cdot c \cdot M_p \text{ Ws}/^\circ\text{C}, \tag{37}$$

where M_p is the sample mass.

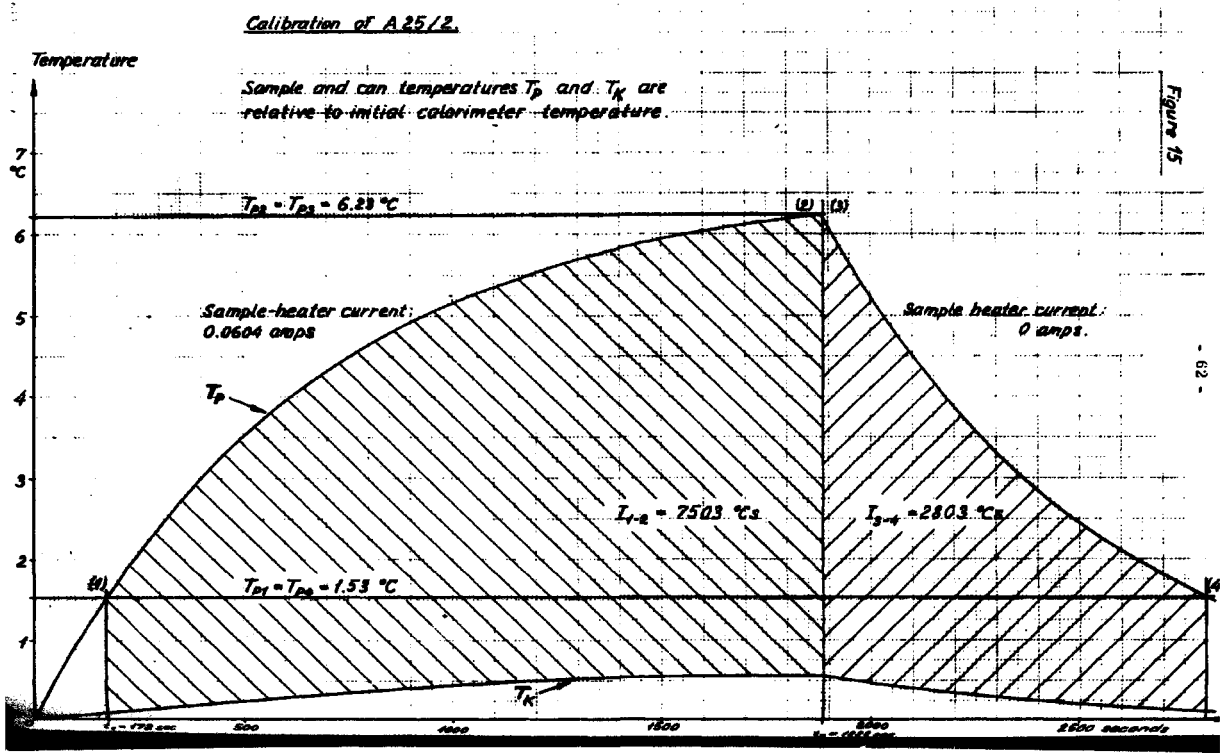
Calibration of A 25/2.
Temperature
Sample and can temperatures T_p and T_K are relative to initial calorimeter temperature.
°C
$T_{p2} = T_{p3} = 6.23$ °C
(2)
(3)
Sample-heater current: 0.0604 amps
Sample heater current: 0 amps.
T_p
$I_{1-2} = 7503$ °Cs
$I_{3-4} = 2803$ °Cs
(1)
$T_{p1} = T_{p4} = 1.53$ °C
(4)
T_K
500
1000
1500
2000 seconds

Figure 15

As the rise in sample temperature is only a few °C, the gas-gap conductivity can be considered constant, and $(W_{cond})_{\Delta T}$ depends consequently only on the sample-can delta temperature ΔT.

If two points on the sample temperature curve are chosen, one on the increasing and one on the decreasing part, so that ΔT is the same for the two points, the value of $(W_{cond})_{\Delta T}$ will also be the same. Thus, by substituting equation (36) into equation (35),

$$W_{el} + C \cdot (dT/dt)_d = C(dT/dt)_i , \tag{38}$$

where indices d and i refer to the decreasing and increasing part of the curve in fig. 15. By means of equation (37) the specific heat of the sample is found:

$$c = \frac{W_{el}}{4.1868 \cdot M_p((dT/dt)_i - (dT/dt)_d)} . \tag{39}$$

By reading many pairs of points on the curve, a number of c-values could be found. However, this is much more easily done by integration of equations (35) and (36):

$$\int_1^2 W_e dt - \int_1^2 K \cdot \Delta T dt = \int_1^2 C \, dT \tag{40}$$

$$-\int_3^4 K \Delta T \, dt = \int_3^4 C \, dT, \tag{41}$$

where 1 and 2 are points on the increasing, and 3 and 4 points on the decreasing part of the curve. K is the thermal conductivity between sample and can.

Integration of (40) and (41) gives

$$W_e(t_2 - t_1) - K \cdot l_{1-2} = C(T_2 - T_1) \tag{42}$$

$$- K \cdot l_{3-4} = C(T_4 - T_3) , \tag{43}$$

where

$$I_{1-2} = \int_1^2 \Delta T \, dt \quad \text{and} \quad I_{3-4} = \int_3^4 \Delta T \, dt \tag{44}$$

are found by graphical integration of the curves in fig. 15. If the curve points are chosen so that

$$T_3 - T_4 = T_2 - T_1 ,$$

(10) and (11) solved with respect to C and K give

$$C = \frac{I_{3-4}}{I_{1-2} + I_{3-4}} \cdot \frac{(t_2 - t_1)}{(T_2 - T_1)} \cdot W_e \quad \text{joules}/^{\circ}C \tag{45}$$

and

$$K = \frac{t_2 - t_1}{I_{1-2} + I_{3-4}} \cdot W_e \quad W/^{\circ}C . \tag{46}$$

The advantage of this type of calibration over the type described earlier is that all parts of the calorimeter have nearly the same temperature during the calibration. The "ideal conditions" stated at the beginning of this section (3.1.2) are thus better approached.

Fig. 17 shows the calibration result: The specific heat of the calorimeter sample versus temperature. The calculated mean specific heat of the sample is also shown in fig. 17. The measured thermocouple μV-signal is transformed into temperature in $^{\circ}C$ by means of standard thermocouple tables as the calorimeter thermocouples have not been calibrated individually. This may explain the deviation between the measured and the calculated curve.

Fig. 16 shows the sensitivities of cromel/alumel thermocouples versus temperature as stated by Kaye and Laby and by Benedict and Ashby. The differential sensitivity at $T^{\circ}C$ is defined as the slope at $T^{\circ}C$ on a curve showing thermocouple voltage versus temperature. It is the sensitivity of a delta temperature measurement by means of two thermocouples placed in nearly the same temperature, e.g. the sample/can delta temperature in the calorimeter. The absolute sensitivity at $T^{\circ}C$ is the sensitivity of a thermocouple with the hot junction at a temperature $T^{\circ}C$ and the cold junction at a reference temperature. In fig. 16 the reference is the room temperature: $20^{\circ}C$. The sensitivity of the centre sample thermocouple in the calorimeter is given by the absolute sensitivity curve.

The calculated curve in fig. 17 is based on the accurate weights and known specific heats of the sample construction materials:

Material	Weight grams	Specific heat cal/°C			Heat capacity cal/°C		
		20°C	110°C	200°C	20°C	110°C	200°C
Al 2S	7.199	0.215	0.225	0.235	1.548	1.620	1.691
Al_2O_3 cement	1.139	0.181	0.224	0.246	0.206	0.255	0.280
CrNi 80/20 heater	1.150	0.108	0.113	0.118	0.016	0.017	0.018
Inconel T/C sheath	0.077	0.108	0.113	0.118	0.008	0.009	0.009
Cromel wire	0.006	0.108	0.113	0.118	0.001	0.001	0.001
Alumel wire	0.005	0.100	0.167	0.175	0.001	0.001	0.001
MgO T/C insulation	0.015	0.262	0.287	0.301	0.004	0.004	0.005
Total	8.591				1.784	1.907	2.005
Mean specific heat of sample, cal/°Cg					0.208	0.222	0.233

In fig. 17 the measured curve is based on seven calibrations of which five were made at a temperature close to room temperature. A calibration at about 200°C failed. Two of the calibrations were made by means of the second calibration method, the others by means of the first method.

The calibration results were:

1st Method

Surrounding temp., °C	29	26	24	89	138
Sample current, amps.	0.0810	0.0985	0.3893	0.081	0.0605
- resistance, ohms	21.33	21.33	21.33	21.54	21.68
- temp. rise rate, °C/s	0.0186	0.0268	0.4083	0.0171	0.0918
- heat capacity, Ws/°C	7.53	7.71	7.91	8.25	8.65
- specific heat, cal/°Cg	0.210	0.215	0.220	0.229	0.240

2nd Method

Surrounding temp., °C	25	26
Sample current, amps.	0.0604	0.0805
- resistance, ohms	21.33	21.33
- temperature rise, °C	4.76	8.11
- heating time, sec.	1716	922
Temperature integral I_{1-21}, °Cs	7503	2803
- - I_{3-41}, °Cs	5833	5542
Sample heat capacity, Es/°C	7.73	7.76
- specific heat, cal/°C g	0.212	0.213
Thermal conductivity of gas gap W/°C	0.0130	0.0112

It was decided to draw the calibration curve in fig. 17 parallel to the calculated curve rather than straight through the calibration points as the temperature dependence of the sample materials is well known and calibration by the first method is rather uncertain at higher temperatures.

3.1.2.2. *Calibration of A25/2 as Isothermal Calorimeter.* After completion of the measurements in reactor run 64 when eight of the fourteen experimental tubes had been scanned, the centre thermocouple in the sample of the calorimeter A25/2 failed. As A25/2 was the only available calorimeter at that time, the measurements had to proceed with A25/2 as an isothermal calorimeter type. Further calibrations would then be necessary to get information on the gas-gap thermal conductivity and the variation of this figure with temperature and vacuum pressure.

With a known gas-gap conductivity K mW/°C, the nuclear heat W mW/g on the sample was found by measuring the sample/can delta temperature as

$$W = \frac{\Delta T \cdot K}{M_p} , \qquad (47)$$

where M_p is the sample mass.

Figure 17

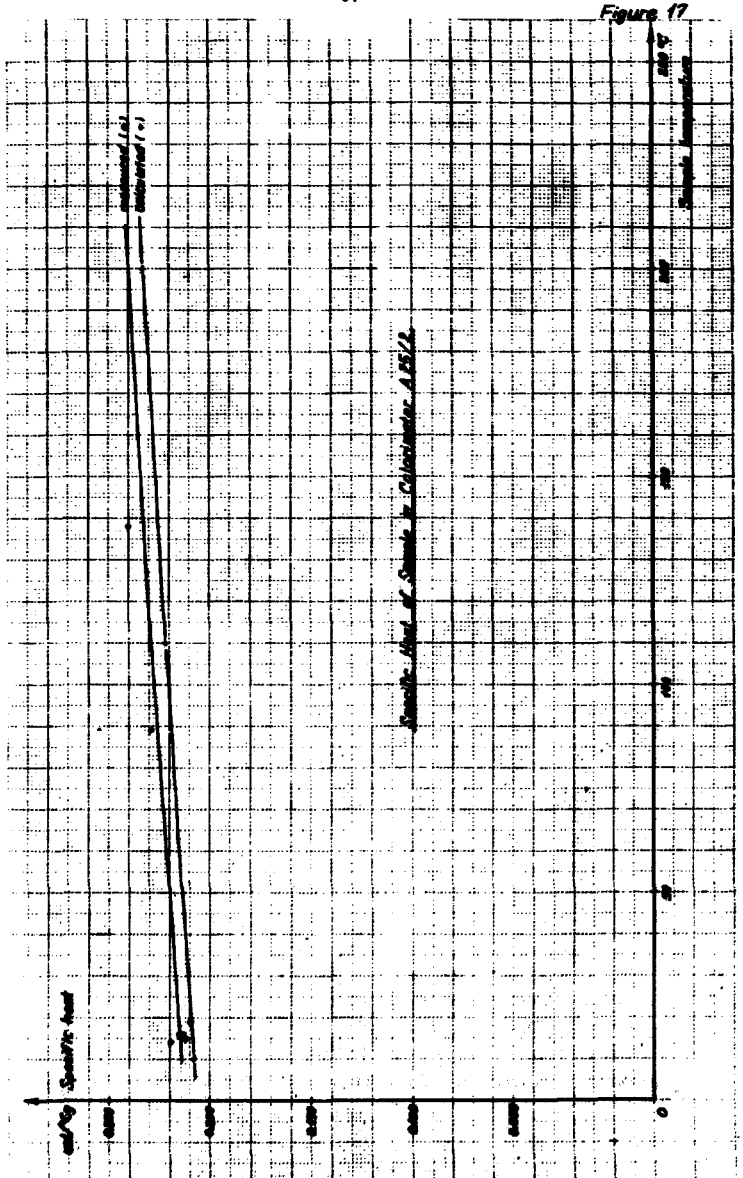
Specific Heat of Sodium by Calorimetric Method
Boiling Point
Melting Point
Specific Heat
Temperature

As shown in 1.3.1, the K value is strongly dependent on the vacuum pressure. Also small changes in the location of the sample in the can may change the K value at changes in the touching area of the supporting mica pieces. Thus the best procedure is to measure the K value in-pile simultaneously with the delta temperature measurement.

The conventional method for in-pile calibration of an isothermal calorimeter is as follows:

Fig. 3.1.2.1

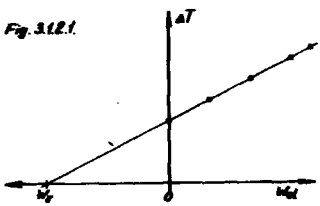

When the temperatures have stabilized in an in-pile measurement, the sample/can delta temperature is read (point 1 on fig. 3.1.2.1). Then an electric current is switched on to the sample heater, and after a new stabilization the delta temperature and the current I_p are read. The electric power on the sample is found from the temperature-corrected sample heater resistance r_T

$$W_{el} = r_T \cdot I_p^2 .$$

By plotting of a number of ΔT- and W_{el}-values in a diagram as 3.1.2.1 (points nos. 2, 3, 4, and 5) the thermal conductivity K is obtained as the slope of the line through the points. The nuclear heat can then be calculated by equation (16), or it can be read graphically by extending the line to the negative part of the W_{el}-axis. The nuclear heat appears as the distance from origin to the crossing point read in the same units as used on the W_{el}-axis. This is seen by comparing equation (16) with the figure.

The in-pile calibration results are given in subsection 3.1.3 together with the measurement results.

A number of K-measurements were also made out-of-pile. As a routine after each movement of the calorimeter flask the value of K was measured in order to check that the calorimeter had not been damaged by the handling bumpings. These measurements were all made at room temperature. At higher temperatures two measurement series were made.

In fig. 9 are seen these K-values measured out-of-pile as a function of the mean sample/can temperature which is an approximation to the gas-gap temperature. The deviations from the line are partly caused by the measurement conditions which were not perfect in all daily routine check measurements, and partly caused by different vacuum pressures. It was not

Figure 9

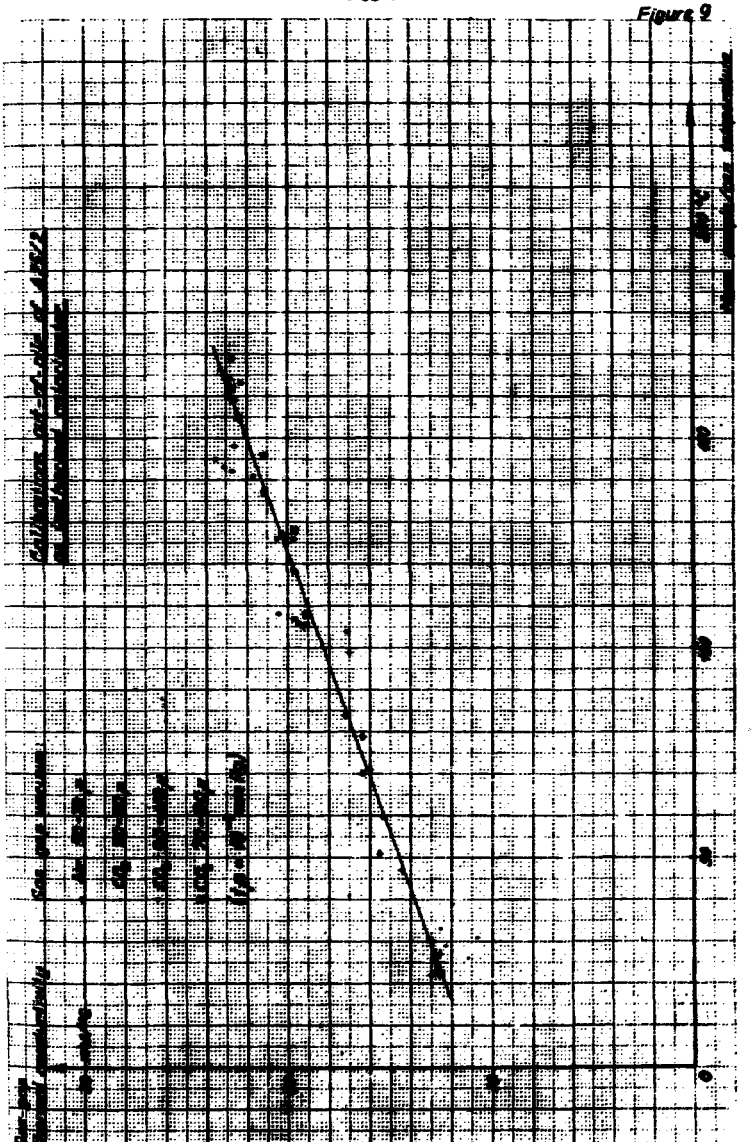

possible to get as low pressures ($< 10^{-3}$ Torr) as intended. The design calculations in section 1.3.1 were based on a vacuum better than 0.1 μ, which gave an estimated gas-gap heat conduction of 3.37 mW/°C. The same calculations based on a vacuum of 100 μ gave a figure of 9.4 mW/°C. The accordance with the measured values at 20°C is fairly good.

3.1.3. Results

The measurements reported here were made in reactor runs 51 to 69 covering the period January 1965 to July 1966.

Changes in core configuration at fuel burn-up and replacement and at rig changes alter the nuclear heat distribution, mainly in the core, but also outside the core in the experimental facilities. Therefore the measurement results cannot be taken as typical for the respective experimental holes. The estimated deviations from the material doses shown in figs. 22 - 35 are not more than 10%. This will be further illustrated for the fuel elements in 3.2.

The adiabatic measurement results are given in table 3.1.1. The sample specific heat is read in fig. 17 at the sample temperature which corresponds to the point on the sample temperature increase curve where the slope dT/dt °C/sec is read. An example of a sample temperature curve is shown in fig. 18. It is a cut of the recorder paper which supplied the result from the measurement in 4V2, 30 cm above the core centre plane (listed in table 3.1.3). As described before, the value of the sample temperature increase rate in the further calculations is the value at about 8 minutes after insertion when the neutron processes have nearly reached their equilibrium state. The sample temperature at this moment determines the value c of the sample specific heat to be used in equation (33) in 3.1.2.1.

The isothermal measurement results are given in table 3.1.2. The nuclear heat is calculated by formula (47) in 3.1.2.2. In fig. 9 is read the gas-gap conductivity at the actual mean gas-gap temperature. This introduces errors in the isothermal measurements as the gas-gap conductivity also changes with the gas-gap vacuum. Table 3.1.3 shows the difference between values obtained by means of out-of-pile calibrations (fig. 9) and in-pile calibrations made in a few positions by electric heating of the sample as described in 3.1.2.

The vacuum was measured at the connection between the flexible hose and the vacuum pump (see fig. 8) as it was practically impossible to connect a vacuum sensor closer to the calorimeter. For this reason the measured vacuum could not be related to the gas-gap conductivity. Nor does fig. 9

Figure 18

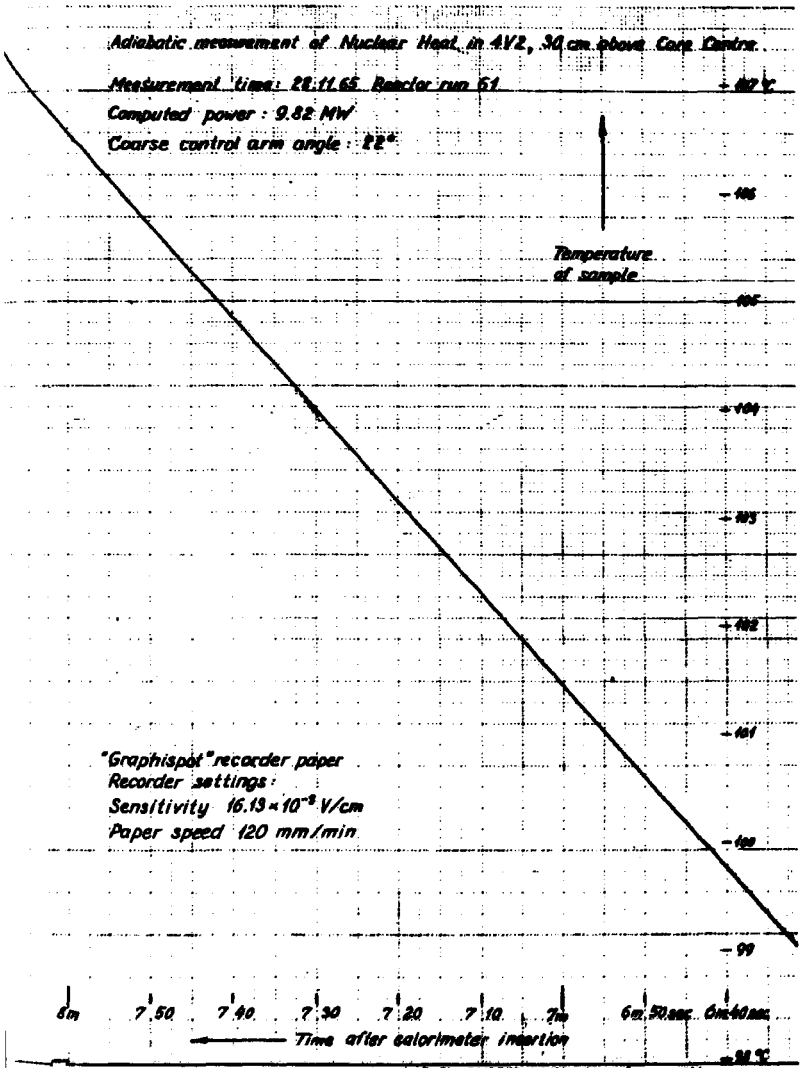
Adiabatic measurement of Nuclear Heat in 4V2, 30 cm above Core Centre
Measurement time: 28.11.65 Reactor run 51
Computed power : 9.82 MW
Course control arm angle : 22°
Temperature of sample
"Graphispot" recorder paper
Recorder settings:
Sensitivity 16.13 × 10⁻³ V/cm
Paper speed 120 mm/min
6m 7'50 7'40 7'30 7'20 7'10 7m 6m,50sec 6m40sec
Time after calorimeter insertion
A. G. FRISENETTE & SONI

indicate a relation, so it must be concluded that the isothermal A25-measurements have a built-in uncertainty resulting from the varying gas-gap vacuum. Table 3.1.3 illustrates the magnitude of this uncertainty.

The trouble might have been avoided if the gas gap had been filled with Co_2 at atmospheric pressure during the isothermal measurements as the thermal conductivity remains constant over a wide range of barometric pressures. Unfortunately we did not realize this problem at the time of failure of the sample centre thermocouple when it was decided to continue the measurements by the isothermal principle.

The vacuum during the measurements listed in tables 3.1.2 and 3.1.3 was in the range 0.07 - 0.14 Torr.

The measured nuclear heat is split into material dose rate and position dose rate in accordance with their definitions in subsection 2.1.2. By means of the thermal and fast-flux values and the calculated conversion factors, given in tables 2.5.13 and 2.5.14, the material dose rates are found. The resulting position dose rates are the heatings from the pure Y-field at the position concerned. This Y-field is perturbed by the presence of the calorimeter, but the size and choice of materials in the calorimeter render the perturbation insignificant.

All dose rates are given in units of mW/g. It should be mentioned here that

$$1 \text{ mW/g} = 100 \text{ rads/sec} = 3.6 \cdot 10^5 \text{ rads/h} . \qquad (48)$$

The reference reactor power, i.e. the thermal power carried away by the secondary reactor cooling system, was not the same in the individual measurements. It is listed as "computed power" in the heading of each graph (figs. 22 - 35). A comparison between the maximum values of the curves in figs. 22 - 35 is given in table 3.1.4. By the normalization to the computed power, 10.0 MW, the comparability is increased, but the figures are still subject to deviations introduced by changes in core configuration from cycle to cycle, as mentioned earlier.

Table 3.1.1

Adiabatic measurements with A35/2 in experimental facilities

Position cm above centrepl.	Temp. increase rate (°C/s)	Sample temp. (°C)	Sample specific heat (cal/°C·g)	Nuclear heat (mW/g)	Thermal flux ($n/cm^2 \cdot s$) x 10^{14}	Fast flux ($n/cm^2 \cdot s$) x 10^{14}	Material dose rate (mW/g)	Pos. dose rate (mW/g)
7V1								
- 10	0.2510	235	0.244	256	0.615	0.0041	93	163
- 5	0.2568	222	0.242	258	0.620	0.0043	94	164
0	0.2552	231	0.244	261	0.620	0.0043	94	167
+ 5	0.2621	212	0.241	264	0.610	0.0043	93	171
+ 10	0.2534	224	0.243	258	0.595	0.0041	90	168
15	0.2402	224	0.243	244	0.570	0.0038	86	158
20	0.2315	214	0.242	235	0.535	0.0034	81	154
30	0.1970	214	0.242	200	0.460	0.0024	70	130
40	0.1630	214	0.242	165	0.370	0.0014	56	109
50	0.1266	214	0.242	129	0.285	0.0007	43	86
60	0.0971	214	0.242	99	0.210	0.0004	32	67
4V1								
+ 17	0.1046	130	0.232	101	0.250	0.0003	38	63
20	0.1014	90	0.226	96	0.240	0.0003	36	60
30	0.0884	100	0.227	85	0.210	0.0001	32	53
40	0.0718	115	0.230	69	0.170	0.0001	26	43
50	0.0551	120	0.230	53	0.140	0.0000	21	32
70	0.0362	70	0.223	34	0.080	0.0000	12	22
4V2								
+ 20	0.0914	106	0.228	87	0.220	0.0002	33	54
30	0.0843	106	0.228	81	0.185	0.0002	28	53
40	0.0713	106	0.228	68	0.150	0.0001	23	45
50	0.0551	106	0.228	53	0.120	0.0000	18	35
60	0.0433	142	0.233	42	0.095	0.0000	14	28
80	0.0240	106	0.228	23	0.050	0.0000	8	15
4V3								
+ 17	0.1349	164	0.236	134	0.250	0.0003	38	96
20	0.1275	191	0.239	128	0.230	0.0002	35	93
30	0.1115	155	0.235	110	0.185	0.0002	25	85
40	0.0975	141	0.233	95	0.120	0.0001	19	77
50	0.0773	147	0.234	76	0.090	0.0000	14	62
60	0.0569	144	0.233	55	0.065	0.0000	10	45
80	0.0393	109	0.229	28	0.035	0.0000	5	23
4V4								
+ 20	0.1385	126	0.231	134	0.315	0.0004	47	87
30	0.1167	127	0.231	113	0.260	0.0003	39	74
40	0.0980	126	0.231	95	0.210	0.0002	32	63
50	0.0774	127	0.231	75	0.165	0.0001	25	50
60	0.0584	127	0.231	57	0.130	0.0001	20	37
70	0.0423	131	0.232	41	0.095	0.0000	14	27
80	0.0302	127	0.231	29	0.065	0.0000	10	19

Table 3.1.1 continued

Position cm centrpl.	Temp. increase rate (°C/s)	Sample temp. (°C)	Sample specific heat (cal/°C·g)	Nuclear heat (mW/g)	Thermal flux ($n/cm^2 \cdot s$) x 10^{14}	Fast flux ($n/cm^2 \cdot s$) x 10^{14}	Material dose rate (mW/g)	Pos. dose rate (mW/g)
4VGR-1								
- 15	0.0222	125	0.231	21.5	0.0600		9.0	12.5
- 10	0.0225	140	0.233	22.0	0.0605		9.1	12.9
- 5	0.0227	151	0.234	22.3	0.0610		9.2	13.1
0	0.0227	162	0.235	22.3	0.0610	less	9.2	13.1
+ 5	0.0228	171	0.236	22.5	0.0605	than	9.1	13.4
10	0.0224	167	0.236	22.2	0.0590	0.0001	8.9	13.3
15	0.0211	110	0.229	20.2	0.0575		8.7	11.5
20	0.0219	130	0.232	21.1	0.0560		8.4	12.7
30	0.0198	150	0.234	19.3	0.0515		7.7	11.6
40	0.0175	180	0.239	17.5	0.0460		6.9	10.6
4VGR-2								
- 10	0.0179	112	0.229	17.2	0.0475		7.1	10.1
- 5	0.0183	110	0.229	17.5	0.0480		7.2	10.3
0	0.0186	110	0.229	17.8	0.0475		7.1	10.7
+ 5	0.0183	110	0.229	17.5	0.0470	less	7.1	10.4
10	0.0180	110	0.229	17.2	0.0460	than	6.9	10.3
15	0.0179	110	0.229	17.1	0.0445	0.0001	6.7	10.4
20	0.0171	110	0.229	16.4	0.0430		6.5	9.9
30	0.0158	110	0.229	15.1	0.0390		5.9	9.2
40	0.0142	110	0.229	13.6	0.0345		5.2	8.4
50	0.0124	110	0.229	11.9	0.0290		4.4	7.5
4VGR-4								
- 15	0.0174	96	0.227	16.6	0.0410		6.2	10.4
- 10	0.0175	123	0.231	16.9	0.0405		6.1	10.8
- 5	0.0175	96	0.227	16.7	0.0400		6.0	10.7
0	0.0178	95	0.227	17.0	0.0390	less	5.9	11.1
+ 5	0.0178	96	0.227	17.0	0.0380	than	5.7	11.3
10	0.0171	95	0.227	16.3	0.0365	0.0001	5.5	10.8
15	0.0168	97	0.227	15.9	0.0350		5.3	10.6
20	0.0164	96	0.227	15.6	0.0335		5.0	10.6
30	0.0147	96	0.227	14.0	0.0300		4.5	9.5
40	0.0130	100	0.228	12.4	0.0260		3.9	8.5
50	0.0111	96	0.227	10.6	0.0210		3.2	7.4

Table 3.1.2

Isothermal measurements with A25/2 in experimental facilities

Position cm above centrepl.	Delta temp. °C	Gas-gap temp. °C	Gas-gap conduct. mW/°C	Nuclear heat mW/g	Thermal flux n/cm² s x 10¹⁴	Fast flux n/cm² s x 10¹⁴	Material dose rate mW/g	Position dose rate mW/g
TV2								
- 10	66.7	175	23.9	186	0.300	0.0025	58	128
- 5	67.4	180	24.3	191	0.390	0.0026	59	132
0	66.9	172	23.1	184	0.390	0.0026	59	125
+ 10	65.5	168	23.4	178	0.370	0.0023	56	122
20	62.1	158	22.6	163	0.330	0.0017	50	113
30	55.7	152	22.2	144	0.275	0.0011	42	102
50	38.4	138	21.1	84	0.170	0.0002	26	66
TV3								
- 10	72.8	184	24.5	208	0.365	0.0027	58	150
0	72.9	181	24.3	206	0.365	0.0028	55	151
+ 10	69.6	179	24.2	196	0.335	0.0026	51	145
20	64.9	176	24.0	181	0.285	0.0022	43	138
30	55.7	171	23.6	153	0.230	0.0016	35	118
40	45.6	164	23.1	123	0.185	0.0011	28	95
50	38.0	162	22.9	101	0.145	0.0006	22	78
60	31.0	135	20.9	75	0.110	0.0003	17	58
TV4								
- 10	87.3	228	27.8	282	0.585	0.0047	90	182
0	89.3	225	27.6	287	0.595	0.0048	90	197
+ 5	91.7	220	27.2	290	0.590	0.0047	90	200
10	90.3	219	27.2	286	0.575	0.0044	87	189
20	83.6	215	26.9	262	0.525	0.0036	80	182
30	77.4	190	25.0	225	0.450	0.0022	66	151
40	65.0	183	24.5	185	0.385	0.0013	55	130
50	52.5	177	24.0	147	0.285	0.0006	43	104
60	41.2	171	23.6	113	0.215	0.0003	32	81
4VGR-3								
- 15	9.42	107	18.8	20.6	0.044		6.6	14.0
- 10	9.76	108	18.8	21.4	0.045		6.7	14.7
- 5	9.88	106	18.8	21.6	0.045	less	6.7	14.8
+ 10	9.65	110	19.0	21.4	0.043	than	6.4	15.0
15	9.41	110	19.0	20.8	0.042	0.0001	6.2	14.6
30	8.71	90	18.2	19.3	0.037		5.5	13.8

Table 3.1.2 continued

Position cm above centrepl.	Delta temp. °C	Gas-gap temp. °C	Gas-gap conduct. mW/°C	Nuclear heat mW/g	Thermal flux n/cm^2 s x 10^{14}	Fast flux n/cm^2 s x 10^{14}	Material dose rate mW/g	Position dose rate mW/g
ϕVGR-5								
- 15	8.54	107	18.8	18.7	0.050		7.5	11.2
- 10	8.60	107	18.8	18.8	0.050		7.5	11.3
- 5	8.70	107	18.8	19.0	0.050		7.5	11.5
0	8.62	107	18.8	18.9	0.049	less	7.3	11.6
+ 5	8.66	107	18.8	19.0	0.048	than	7.2	11.8
10	8.59	107	18.8	18.8	0.047	0.0001	7.0	11.8
20	8.52	105	18.7	18.5	0.044		6.6	11.9
30	7.70	104	18.6	16.7	0.040		5.9	10.8
40	6.92	104	18.6	15.0	0.035		5.2	9.8
50	6.06	103	18.5	13.1	0.029		4.4	8.7
ϕVGR-6								
- 10	8.54	111	19.1	19.0	0.047		7.0	12.0
0	8.70	111	19.1	19.3	0.046		6.9	12.4
+ 10	8.50	111	19.1	18.9	0.045	less	6.8	12.1
20	7.97	110	19.0	17.6	0.043	than	6.4	11.2
30	7.54	110	19.0	16.7	0.039	0.0001	5.9	10.8
40	6.33	111	19.1	14.1	0.035		5.2	8.9
50	5.58	111	19.1	12.4	0.029		4.4	8.0

Table 3.1.3

In-pile isothermal calibrations of A25/2

Exper. hole	Position cm above centrepl.	Gas-gap temp. °C	Electric sample power mW/g	Delta temp. °C	Calculations by means In-pile calibr.		Out-of-pile cal.	
					Gas-gap conduct mW/°C	Nuclear heat mW/g	Gas-gap conduct mW/°C	Nuclear heat mW/g
7V2	- 10	175	0	66.7				
	- 10	190	49.1	82.8	25.9	200	23.9	186
	- 10	202	100.3	101.1				
4VGR-3	+ 15	110	0	9.41	16.1	17.6	19.0	20.8
	+ 15	112	9.02	14.23				
4VGR-3	+ 30	99	0	8.71				
	+ 30	100.8	7.86	12.62	17.1	17.4	18.2	19.3
	+ 30	102.4	12.28	14.89				
4VGR-3	+ 80	78	0	4.29				
	+ 80	8'	6.22	8.05	15.0	7.4	16.6	8.3
	+ 80	82	8.95	9.81				
4VGR-3	+110	61	0	2.10				
	+110	63	0.99	2.75	12.6	3.0	15.4	3.8
	+110	65	3.98	4.81				

Table 3.1.4

Maximum position dose rates normalized to computed power 10.000 MW

Position	Computed power MW	Max. pos. dose rate mW/g Measured	Normaliz.	Position	Computed power MW	Max. pos. dose rate mW/g Measured	Normaliz.
7V1	9.86	169	172	4VGR-1	9.90	13.3	13.4
7V2	9.76	129	132	4VGR-2	10.00	10.6	10.6
7V3	9.24	151	163	4VGR-3	9.90	15.0	15.2
7V4	10.04	200	199	4VGR-4	9.50	11.1	11.7
4V1	9.84	60	61	4VGR-5	9.40	11.8	12.6
4V2	9.82	56	57	4VGR-6	10.15	12.4	12.2
4V3	9.86	93	94				
4V4	10.10	86	85				

FIGURE NO. 2

REAKTOR DR - 3

POSITION DOSE RATE IN 7V1

MEASUREMENT DATA

PERIOD No 63

CALORIMETER	A 25/ 2
COMPUTED POWER	986 MW
CCA ANGLE	23,883°
FCR. POSITION	29,7 cm
DATE OF MEASUREMENT	29/12/ 65
CORE CONFIGURATION No	92

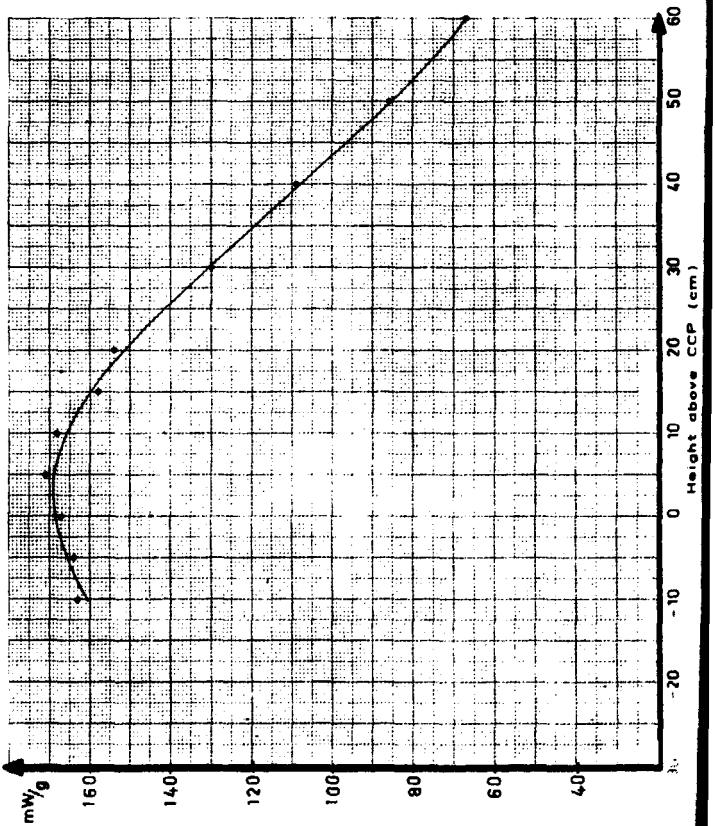

FIGURE NO. 24

REAKTOR DR - 3.

POSITION DOSE RATE IN 7v2

MEASUREMENT DATA

PERIOD No 64

CALORIMETER	A 25/2
COMPUTED POWER	976 MW
CCA. ANGLE	19,735°
FCR. POSITION	—
DATE OF MEASUREMENT	19/1/66
CORE CONFIGURATION No	93

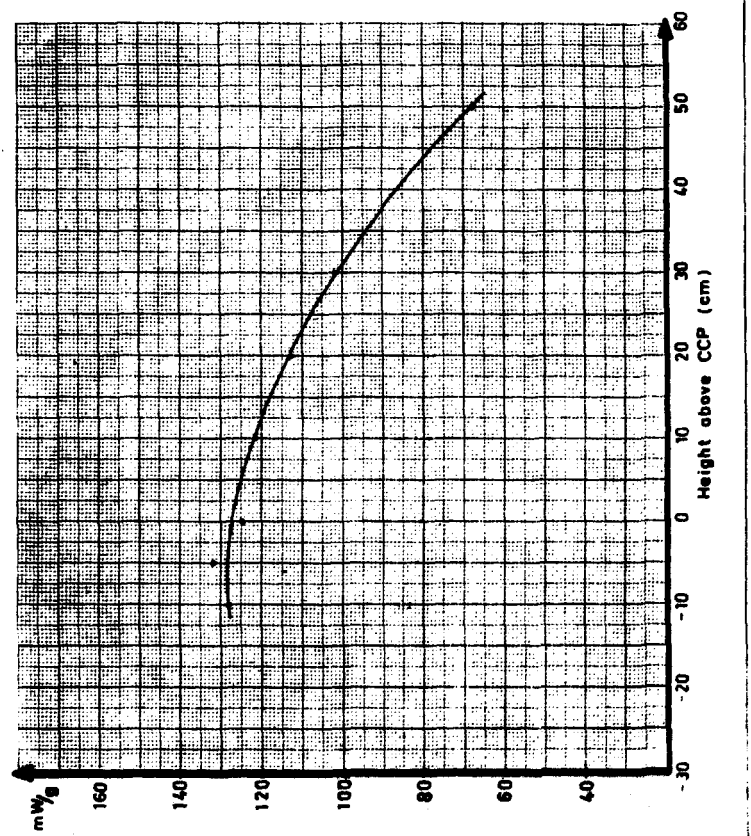

FIGURE NO.B

REAKTOR DR - 3

POSITION DOSE RATE IN 7V3

MEASUREMENT DATA

PERIOD No 65

CALORIMETER	A 25/2
COMPUTED POWER	9.24 MW
CCA ANGLE	21.694°
FCR POSITION	—
DATE OF MEASUREMENT	24/2/66
CORE CONFIGURATION No	94

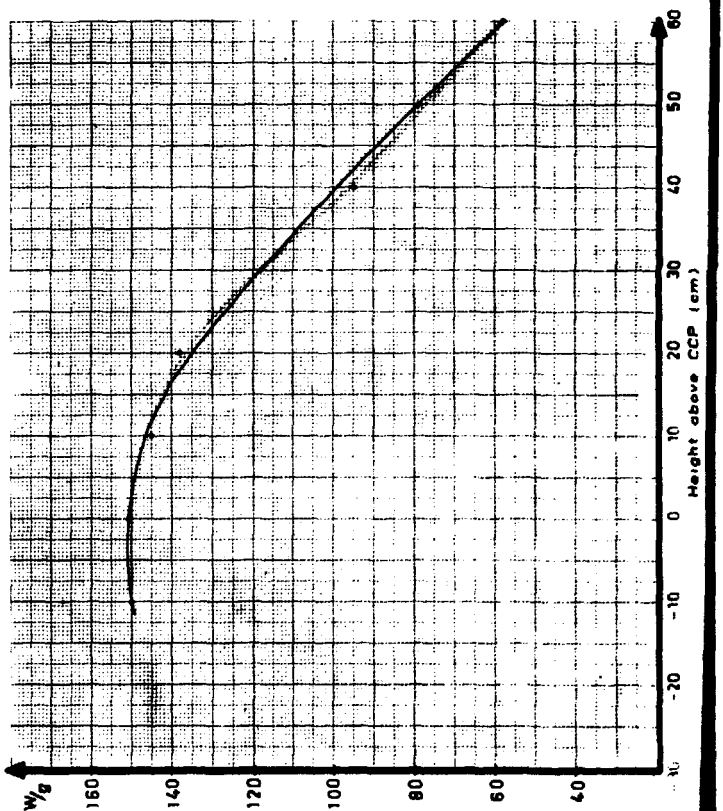

FIGURE No. 25

REAKTOR DR - 3

POSITION DOSE RATE IN 7V4

MEASUREMENT DATA

PERIOD No. 69

CALORIMETER	A 25/2
COMPUTED POWER	1004 MW
CCA ANGLE	26,958 °
FCR POSITION	———
DATE OF MEASUREMENT	15/6/66
CORE CONFIGURATION No	98

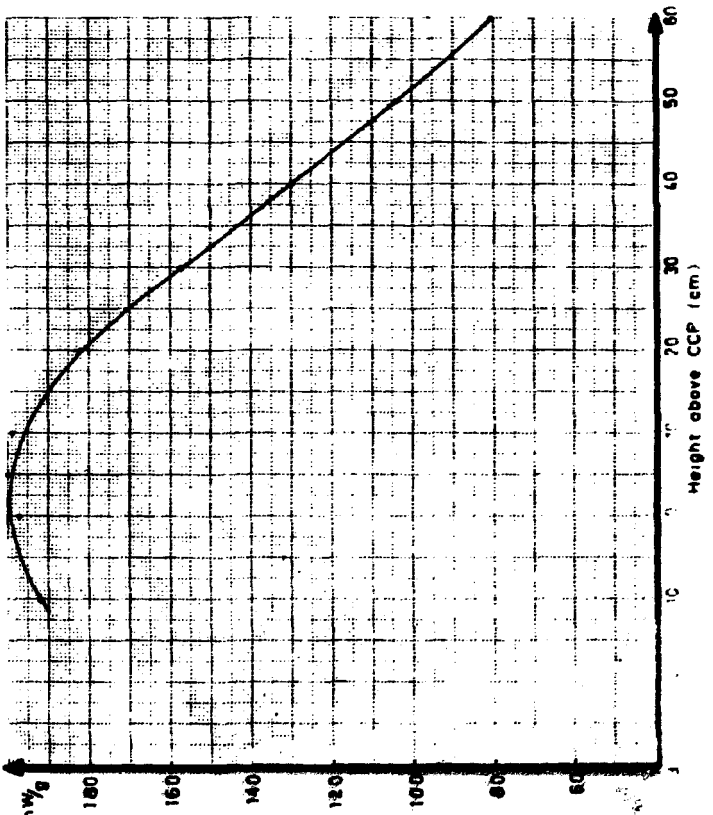

FIGURE NO. 27

REAKTOR DR - 3

POSITION DOSE RATE IN 4V1

MEASUREMENT DATA

PERIOD No. 51

CALORIMETER	A 25/2
COMPUTED POWER	984 MW
CCA ANGLE	19.276°
FCR POSITION	
DATE OF MEASUREMENT	18/1/65
CORE CONFIGURATION No	80

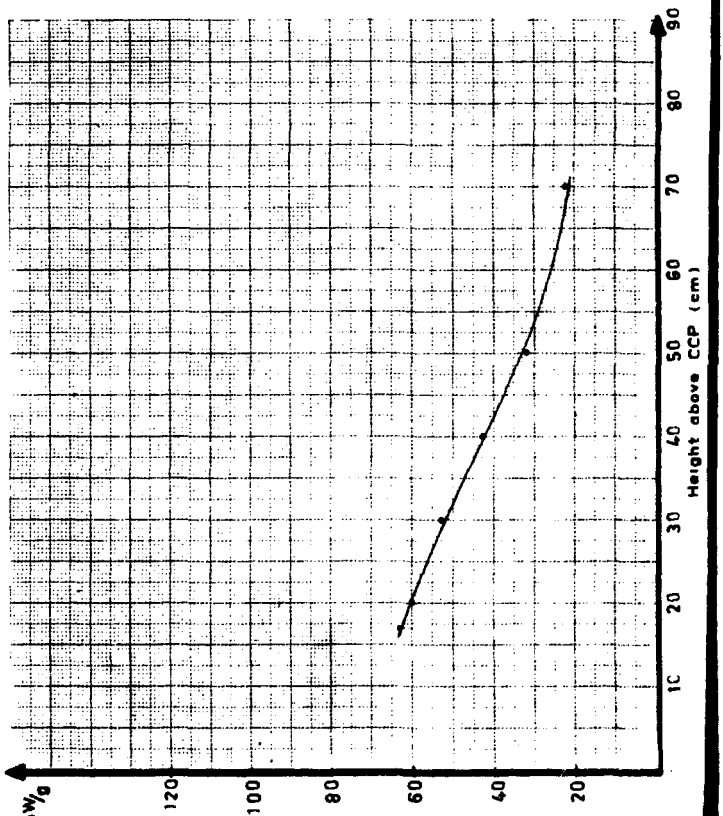

FIGURE NO. 28

REAKTOR DR - 3

POSITION DOSE RATE IN 4V2

MEASUREMENT DATA

PERIOD No. 61

CALORIMETER	A 25/2
COMPUTED POWER	982 MW
CCA ANGLE	22,390°
PCR POSITION	
DATE OF MEASUREMENT	28/10/65
CORE CONFIGURATION No	90

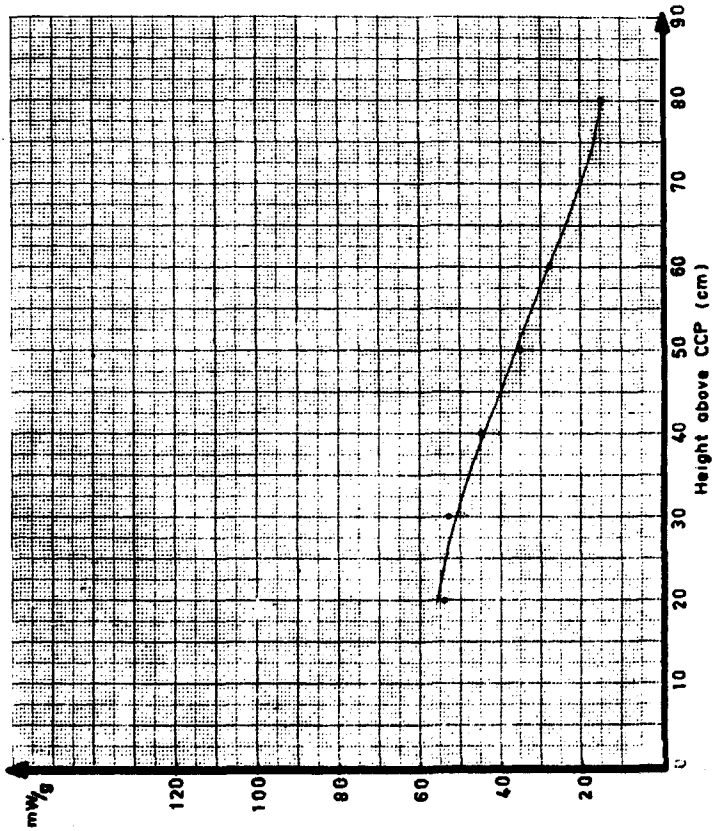

FIGURE NO. 8

REAKTOR DR - 3

POSITION DOSE RATE IN 4V3

MEASUREMENT DATA

PERIOD No. 59

CALORIMETER	A 25/2
COMPUTED POWER	9.86 MW
CCA ANGLE	28.861°
FCR POSITION	-
DATE OF MEASUREMENT	6/9-1965
CORE CONFIGURATION No.	88

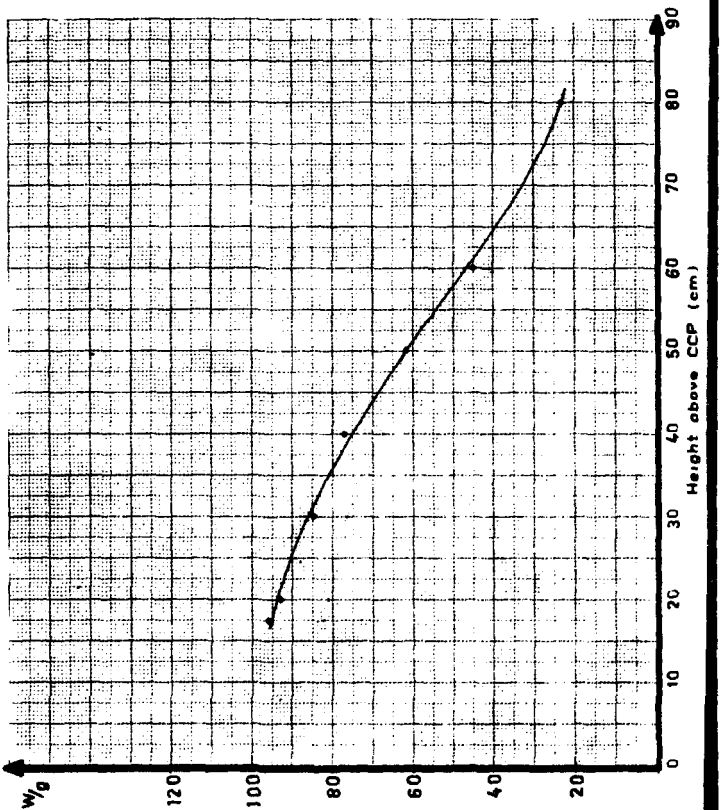

FIGURE NO. 30

REAKTOR DR - 3

POSITION DOSE RATE IN 4V4

MEASUREMENT DATA

PERIOD No. 62

CALORIMETER	A 25/2
COMPUTED POWER	10.10 MW
CCA ANGLE	25.086°
FCR POSITION	-
DATE OF MEASUREMENT	25/11-1965
CORE CONFIGURATION No.	91

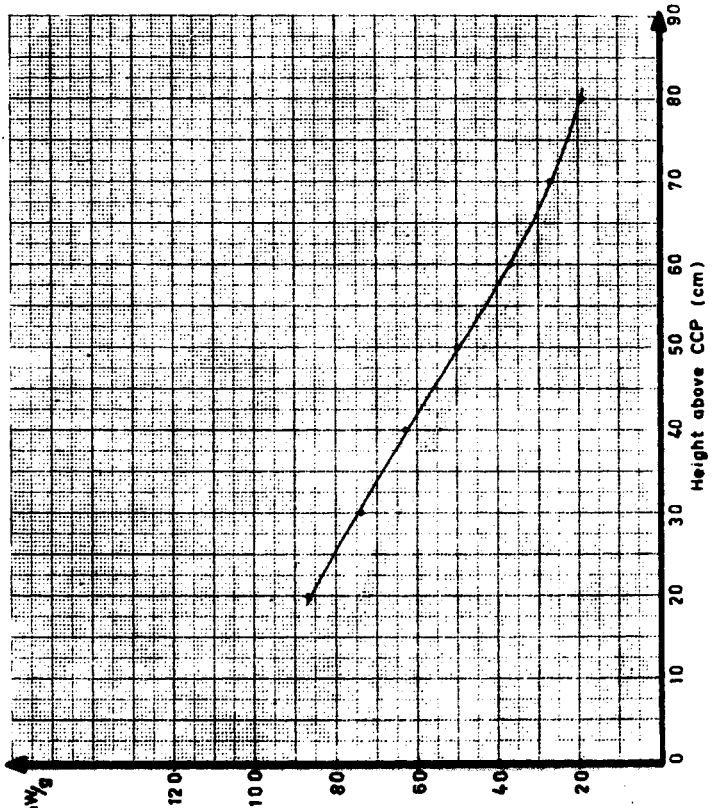

FIGURE No. 11

REAKTOR DR - 3.

POSITION DOSE RATE IN 4VGR-1

MEASUREMENT DATA

PERIOD No. 58

CALORIMETER	A 25/2
COMPUTED POWER	9.90 MW
CCA. ANGLE	31.695°
FCR. POSITION	—
DATE OF MEASUREMENT	12/8-1965
CORE CONFIGURATION No.	87

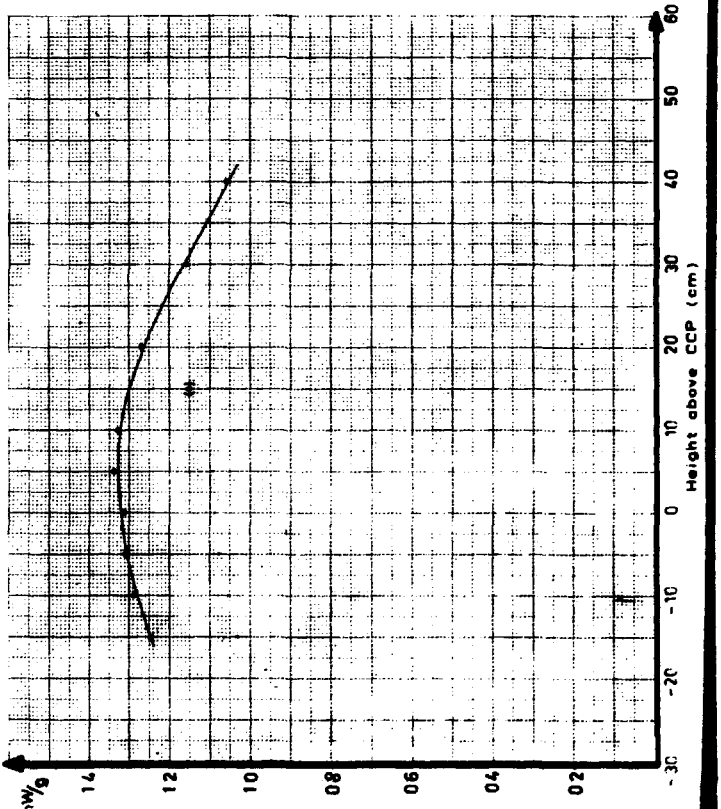

FIGURE NO. 22

REAKTOR DR - 3.

POSITION DOSE RATE IN 4VGR-2.

MEASUREMENT DATA.

PERIOD No. 63

CALORIMETER.	A 25/2
COMPUTED POWER.	10.00 MW
CCA. ANGLE.	21.260°
FCR POSITION	—
DATE OF MEASUREMENT.	23/12-1965
CORE CONFIGURATION No.	92

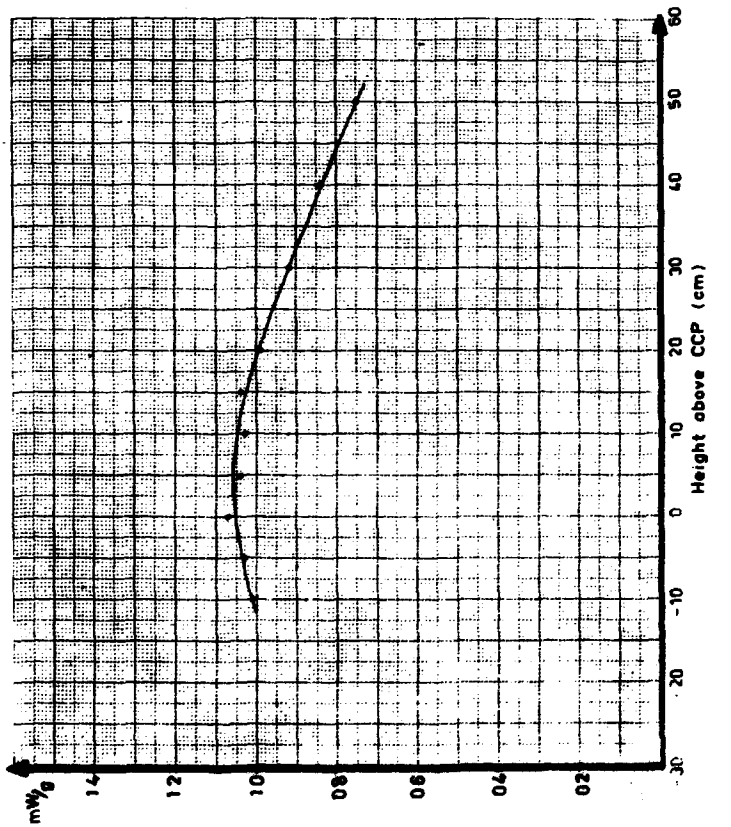

FIGURE NO.31

REAKTOR DR - 3

POSITION DOSE RATE IN 4VGR-3

MEASUREMENT DATA PERIOD No. 64

CALORIMETER	A 25/2
COMPUTED POWER	9.90 MW
CCA ANGLE	21.358°
FCR POSITION	—
DATE OF MEASUREMENT	27/1-1966
CORE CONFIGURATION No	93

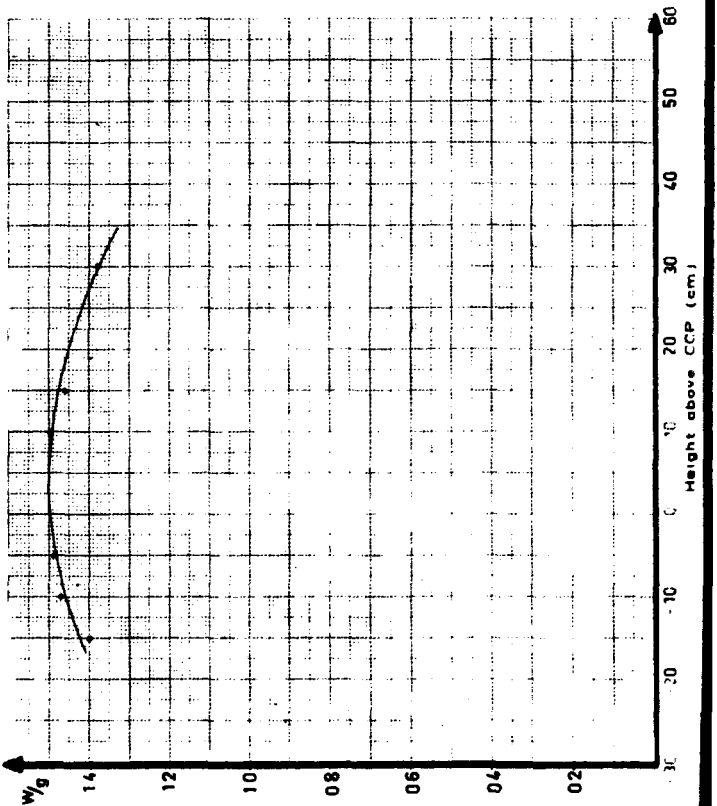

FIGURE NO. 34

REAKTOR DR - 3

POSITION DOSE RATE IN 4V GR-4

MEASUREMENT DATA

PERIOD No. 60

CALORIMETER	A 25/2
COMPUTED POWER	9.50 MW
CCA. ANGLE	25.229°
FCR. POSITION	–
DATE OF MEASUREMENT	4/10-1965
CORE CONFIGURATION No.	89.

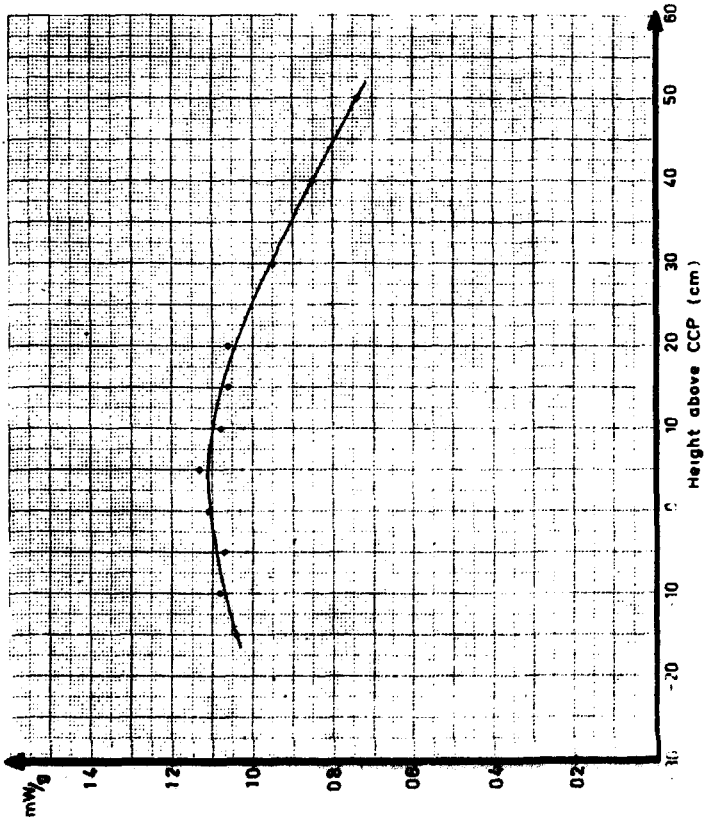

flamm

FIGURE NO. 31

REAKTOR DR - 3.

POSITION DOSE RATE IN 4VGR-5.

MEASUREMENT DATA PERIOD No 65.

CALORIMETER	A 25/2
COMPUTED POWER	9.40 MW
CCA ANGLE	17.899°
FCR POSITION	—
DATE OF MEASUREMENT	12/2-1966
CORE CONFIGURATION No	94.

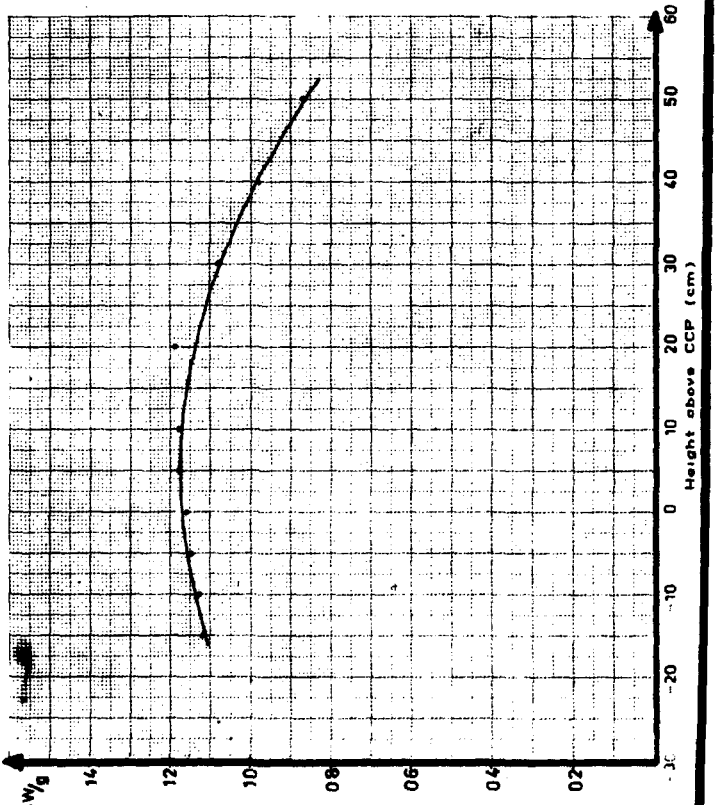

FIGURE NO. 36

REAKTOR DR - 3.

POSITION DOSE RATE IN 4VGR-6.

MEASUREMENT DATA. PERIOD No. 66

CALORIMETER	A 25/2
COMPUTED POWER.	10.15 MW
CCA. ANGLE	19.247°
FCR POSITION	—
DATE OF MEASUREMENT	16/3 1966.
CORE CONFIGURATION No	95.

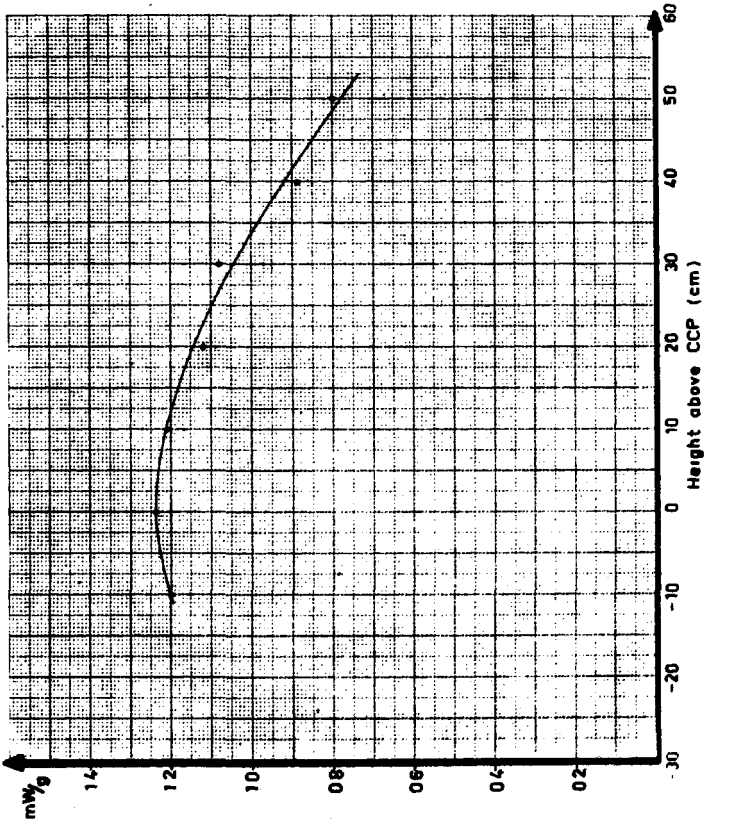

3.2. Scannings of the Core by Means of Calorimeter I6

3.2.1. Methods and Techniques

All core positions which are equipped with a flux-scan tube can be scanned by an I6 calorimeter. The standard flux-scan tube used in DR 3 is an aluminium tube with inner/outer diameter 7.8/9.5 mm (5/16"/3/8"). Also slighty curved flux-scan tubes as those installed in Mk. 2 fuel elements can be scanned by an 16 calorimeter.

The equipment for insertion and withdrawal of the calorimeter is described in 1.6 and shown schematically in fig. 10. By means of 8 cable cams spaced 10 cm apart, vertical scans are performed from 30 cm below to 40 cm above the core centre plane. The measurement time in each position is set at 8 minutes. Two special cams constitute the lower and upper limit switches. The latter stops the calorimeter in the top plug for "cooling" (decay) after a scan. Generally, the scans are made during upward movement of the calorimeter.

Including the time needed for withdrawal of the calorimeter, movement of the gear plug to a new position and re-insertion of the calorimeter in the core, a measurement takes ideally 1 1/2 hours if the operator is not occupied with other experiments. Generally 4 positions are scanned in each 8-hour shift. Thus, a full core scan is made within two days.

The calorimeter type was gradually modified during the making and operation of the first six serial numbers. The design stayed unchanged from I6/7. Fig. 5 shows an X-ray photo of I6/7.

Routine scans of all accessible positions in the core were made at the beginning and at the end of nearly every reactor run (three weeks' continuous reactor operation) since May 1969. The calorimeters were in operation as follows:

I6/7	reactor runs	108 - 110 (May - August 1969)
I6/8	reactor runs	111 - 117 (August 1969 - March 1970)
I6/9	reactor runs	118

The calorimeters I6/7 and I6/8 failed at open T/C-circuit. Repair was impossible because the radiation from the long-lived isotopes in the heater and thermocouple wires was too high.

The material dose rate calculations in 2.5.2 are based on calorimeter I6/9, but they are also applicable to I6/7 and I6/8 as these calorimeters are identical with respect to materials and geometrical size.

3.2.2. Calibrations

By means of the built-in heater wire the I6 calorimeter can be electrically calibrated. If the resistance of each of the two wires in the heater loop is

$$\frac{1}{2} \cdot r \text{ ohms/cm},$$

and the current is i amps., the heat deposition in the sample rod at electrical calibration out-of-pile is

$$r \cdot i^2 \text{ W/cm}.$$

As the aluminium weight of one cm of the rod is

$$A \cdot V \text{ g/cm},$$

where A is the rod cross section and V the aluminium density, we have ideally

$$q' = \frac{r \cdot i^2}{A \cdot V} \text{ W/g}. \qquad (49)$$

where q' is the nuclear heat in an in-pile measurement which produces the same delta temperature between the rod ends as the current i in an out-of-pile calibration.

However, these idealized conditions are not quite realistic. The main objections are:

(1) The thermocouple and heater cables contribute to the heating of the rod when exposed to nuclear heat.

(2) The heater and inner thermocouple are not carried right to free end of the rod.

(3) The parameters r, A and V are temperature-dependent.

Correction for (1) can be made by the following consideration:

The alloys in the cable sheaths and wires are Co, Ni, Al, Cr, and small amounts of Si, Fe and Mn. As the mass γ-absorption coefficients of these metals have nearly the same spectrum in the range 1 - 3 MeV, which is the most significant part of the reactor γ-spectrum, the relative contribution of the cables to the nuclear heat in the rod can be approximated

by the relative cable mass in the rod. The axial heat conduction in a cable is negligible. The relative mass is

$$\frac{M_c}{A \cdot V}$$

for each cable, where M_c g/cm denotes the mass of one cable. Consequently the nuclear heat found from eq. (49) has to be corrected to

$$q = \frac{q'}{1 + \frac{n \cdot M_c}{A \cdot V}} = \frac{q'}{k_n} , \qquad (50)$$

where n is the number of cables.

The actual values of k_n are given in table 3.2.1.

Table 3.2.1

Corrections for nuclear heat in rod cables

	n	M_c (mg/cm)	A (cm^2)	V (g/cm^2)	k_n
Rod section with 1 cable	1	11.6	0.124	2.7	1.0353
Rod section with 2 cables	2	11.6	0.122	2.7	1.0706

In order to give an answer to objection (2), more detailed calculations than those shown in 1.3.2 are needed.

In fig. 11 the rod is divided into three sections, $0\text{-}x_v$, $x_v\text{-}x_i$ and $x_i\text{-}x_y$ with 0, 1 and 2 cables in the rod. Cross sections as well as nuclear heat depositions change from section to section, so an exact calculation necessitates successive treatments of the individual sections.

Below formulas for an arbitrary section will be deduced.

In 1.3.2 the rod is treated as a whole, and it is assumed that the temperature gradient in the free rod end is 0. This is not the case in an arbitrary section, and consequently eq. (1) in 1.3.2 must be modified to

$$Z_x^2 = \frac{2qV}{K}(T_a - T_x) + Z_a^2 , \qquad (51)$$

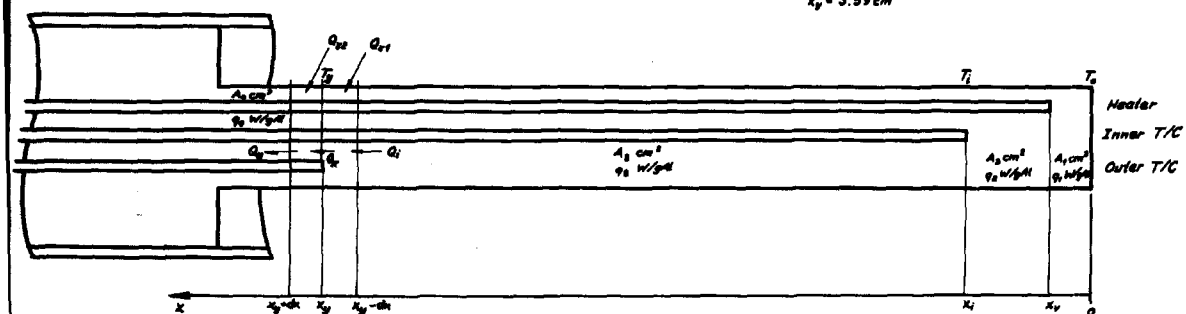

Calorimeter J6. Principle diagram for calibration calculations.

Figure 11

where index "a" refers to the section boundary closest to the free end of the rod. For simplicity we put

$$C \equiv \frac{qV}{2K}$$

and find

$$\frac{d(T_x)}{dx} = Z_x = -\sqrt{4C(T_a - T_x) + Z_a^2}. \tag{52}$$

It is evident that Z will not be positive.
By integration we find

$$x - x_a = \int_{x_a}^{x} dx = -\int_{T_a}^{T_x} \frac{d(T_x)}{\sqrt{4C(T_a - T_x) + Z_a^2}}$$

$$x - x_a = \frac{1}{2C}\left[\sqrt{4C(T_a - T_x) + Z_a^2}\right]_{T_a}^{T_x} = \frac{1}{2C}\left(\sqrt{4C(T_a - T_x) + Z_a^2} + Z_a\right), \tag{53}$$

and consequently

$$T_x = T_a - (x - x_a)^2 \cdot C + (x - x_a) \cdot Z_a . \tag{54}$$

When the temperature T_a and temperature gradient Z_a at one end of a rod section are known, the corresponding T_b and Z_b at the other end of the rod section can be calculated from eqs. (54) and (52) as

$$T_b = T_a - (x_b - x_a)^2 \cdot C + (x_b - x_a) Z_a \tag{55}$$

and

$$Z_b = -\sqrt{4C(T_a - T_b) + Z_a^2}. \tag{56}$$

By crossing the boundary between two sections a discontinuity in the temperature gradient is introduced. Consequently Z_b cannot be used directly as "input value" to the calculations for the subsequent section.

Consider the infinitesimal rod sections around x_y in fig. 11. The heat equations for the two sections are

$$\begin{aligned} Q_i + Q_{y1} &= Q_x \\ Q_x + Q_{y2} &= Q_u \\ \hline Q_i + Q_{y1} &= Q_u - Q_{y2} \,. \end{aligned} \tag{57}$$

By means of the conventional equations for heat transfer eq. (57) is expanded to

$$-K \cdot A_3 \cdot Z_{x_y - dx} + q_3 \cdot V \cdot A_3 \cdot dx = -K \cdot A_4 \cdot Z_{x_y + dx} - q_4 \cdot V \cdot A_4 \cdot dx$$

or

$$(q_3 A_3 + q_4 A_4) V \, dx = K(A_3 \cdot Z_{x_y - dx} - A_4 \cdot Z_{x_y + dx}) \,.$$

which gives the discontinuity of the temperature gradient for $dx \to 0$

$$Z_{x_y + dx} = \frac{A_3}{A_4} \cdot Z_{x_y - dx} \,. \tag{58}$$

The temperature T_y is now calculated for in-pile measurements and for out-of-pile electrical calibrations by means of eqs. (55), (56) and (58) used on the rod sections

1 : $0 - x_v$

2 : $x_v - x_1$

3 : $x_1 - x_y$.

<u>In-pile</u>: $(C \equiv \frac{Vq}{2K})$

1. $x = 0$: $T = T_o$; $Z = 0$

$x = x_v$: $T_v = T_o - x_v^2 \cdot Ck_1$; $Z_{v1} = -2Ck_1 x_v$

2. $x = x_v$: $Z_{v2} = -2Ck_1 x_v \frac{A_1}{A_2}$

$$x = x_i: \quad T_i = T_o - x_v^2 Ck_1 - (x_i - x_v)^2 Ck_2 - 2(x_i - x_v) Ck_1 x_v \frac{A_1}{A_2}$$

$$x = x_i: \quad Z_{i2} = -2C \sqrt{k_2 ((x_i - x_v)^2 k_2 + 2(x_i - x_v) \frac{A_1}{A_2} k_1 x_v) + \frac{A_1^2}{A_2^2} k_1^2 x_v^2}$$

3. $$x = x_i: \quad Z_{i3} = \frac{A_2}{A_3} \cdot Z_{i2}$$

$$x = x_y: \quad T_y = T_i - (x_y - x_i)^2 Ck_3 + (x_y - x_i) \frac{A_2}{A_3} \cdot Z_{i2} \qquad (59)$$

Out-of-pile: $(D \equiv \frac{ri^2}{2K} = q\frac{AV}{2K} = CA)$

1. $$x = 0: \quad T = T_o; \quad Z = 0$$

$$x = x_v: \quad T = T_o; \quad Z_{v1} = Z_{v2} = 0$$

2. $$x = x_i: \quad T_i = T_o - (x_i - x_v)^2 \cdot \frac{D}{A_2}; \quad Z_{i2} = -2(x_i - x_v) \frac{D}{A_2}$$

3. $$x = x_i: \quad Z_{i3} = -2(x_i - x_v) \frac{D}{A_3}$$

$$x = x_y: \quad T_y = T_i - (x_y - x_i)^2 \cdot \frac{D}{A_3} - 2(x_y - x_i)(x_i - x_v) \frac{D}{A_3} \qquad (60)$$

If a nuclear heat qW/g produces the same rod delta temperature $(T_i - T_y)^\circ C$ as a current i amp. in an out-of-pile calibration, eqs. (59) and (60) give the relation between q and i

$$q = \frac{r \cdot i^2}{A_3 \cdot V} k_c$$

$$= \frac{ri^2}{A_3 \cdot V} \cdot \frac{x_y + x_i - 2x_v}{(x_y - x_i)k_3 + 2\frac{A_2}{A_3}\sqrt{k_2((x_i - x_v)^2 k_2 + 2(x_i - x_v)\frac{A_1}{A_2} k_1 x_v) + (\frac{A_1}{A_2} k_1 x_v)^2}} \qquad (61)$$

where the correction factor for the cable geometry k_c is defined by the equation.

Actual values of k_c for the calorimeters are given in table 3.2.2.

Table 3.2.2

Corrections for calorimeter cable geometry

	x_v (cm)	x_i (cm)	x_y (cm)	k_c
I6/7	0.17	0.20	3.52	0.852
I6/8	0.14	0.19	3.61	0.868
I6/9	0.16	0.18	3.59	0.858

In the method of electrical calibration it is assumed that the mean rod temperature T_R is the same at calibrations as at in-pile measurements with the same rod delta temperatures. This implies that errors from heat losses through the gas gap and from variation of the rod mean temperature are eliminated.

Consequently, in the treatment of objection (3) it is not necessary to evaluate the temperature corrections for the rod cross section A and the rod density V. Only the temperature correction of the heater loop resistance r is relevant.

The actual value of the heater loop resistance r ohms/cm during a calibration depends on the rod mean temperature T_R and the heater load which produces an excess heater temperature ΔT above T_R: With a 1-core model equivalent to the 2-core heater we find

$$\Delta T = \frac{r \cdot i^2 \cdot \ln(d_2/d_1)}{\lambda \cdot 2\pi \cdot 1} \quad , \tag{65}$$

where the mineral insulator of the cable has an inner and outer diameter d_1 and d_2 and heat conductivity λ.

With

r = 3.38 ohms/cm

d_1 = 0.018 cm

d_2 = 0.035 cm

λ = 0.0084 W/^oC · cm

we find

$$\Delta T = 42.4 \cdot i^2 \, ^\circ C , \tag{66}$$

and thus the heater temperature correction k_r is given by

$$r_{TR+\Delta T} = r \cdot k_r = r(1+\alpha_r(T_R + 42.4\, i^2 - 22)) . \tag{67}$$

The temperature coefficient is

$$\alpha_r = 1 \cdot 10^{-4} (^\circ C)^{-1} .$$

The heater loop resistance r should be four times the unswaged heater cable loop resistance R if the swaging is made correctly. Both values are given in table 3.2.3 for comparison. The value r was measured on the heater leads of the stripped calorimeter after the calorimeter was taken out of operation.

Table 3.2.3

Calibration heater loop resistance

	R (ohms/cm)	4R (ohms/cm)	r (ohms/cm)
16/7	0.8532	3.41	3.37
16/8	0.8472	3.39	3.43
16/9	0.8460	3.38	3.42

The expression for the nuclear heat, including the corrections deduced above, is then

$$q = k_c \cdot k_r \cdot \frac{r \cdot i^2}{AV} . \tag{68}$$

The calibration result for each calorimeter is a plot of the measured rod delta temperature

$$\Delta T = T_i - T_y$$

versus the applied temperature-corrected heat per cm rod length:

$W_1 = k_r \cdot r \cdot i^2$, see figs. 19, 20 and 21.

The slope of a linear fit through origin is the calibration factor

$$f_c = \frac{\Delta T}{W_i} . \tag{69}$$

The calorimeter sensitivity f_s is defined by

$$q = f_s \cdot \Delta T . \tag{70}$$

The relationship between f_c and f_s is found by means of eqs. (68), (69) and (70):

$$q = f_s \cdot \Delta T = \frac{k_c}{AV} \cdot k_r \cdot r \cdot i^2$$

$$f_s = \frac{k_c}{AV} \cdot \frac{W_1}{\Delta T} = \frac{k_c}{AV f_c} \tag{71}$$

The calibration factors and the appropriate sensitivities are listed in table 3.2.4. For comparison is also given the calibration factors calculated from the known physical constants and corrected for the heat transfer through the gas gap. This calculation will be found in the Appendix.

Table 3.2.4

Calibration factor and calorimeter sensitivity

	$f_c(^oC \cdot cm/W)$ calculated	$f_c(^oC \cdot cm/W)$ measured	$f_s(W/g \cdot {}^oC)$
16/7	21.0	21.2	0.121
16/8	22.6	22.6	0.116
16/9	22.0	21.2	0.122

In the calculation of f_s the constants

$A_3 = 0.123\ cm^2$, $A_2 = 0.125\ cm^2$, $A_1 = 0.126\ cm^2$

$V = 2.70\ g/cm^3$

are used.

Figure 18.

Calibration of Isothermal Rod Calorimeter IG/2

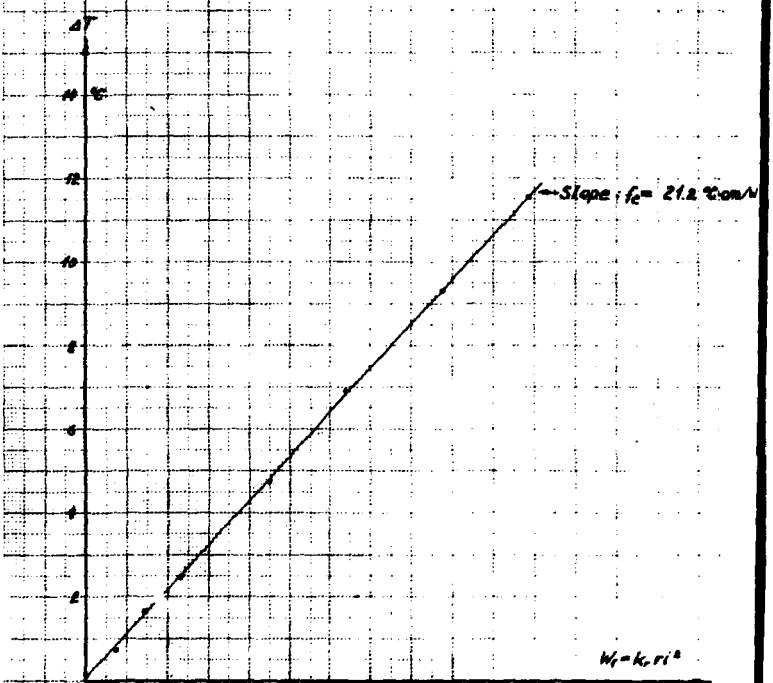

Figure 20

Calibration of Isothermal Rod Calorimeter T6/8

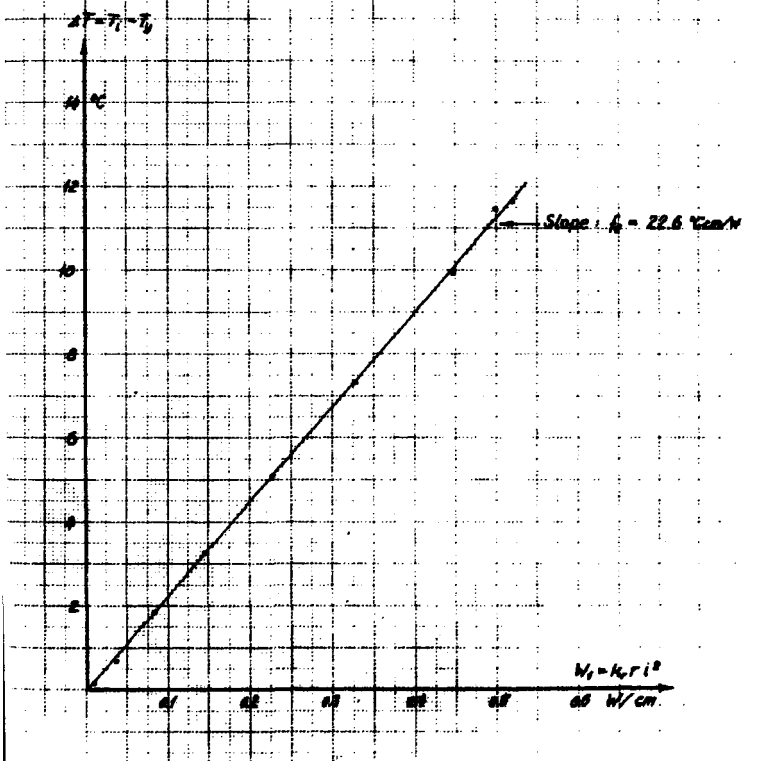

Figure 21.

Calibration of Isothermal Rod Calorimeter I6/9

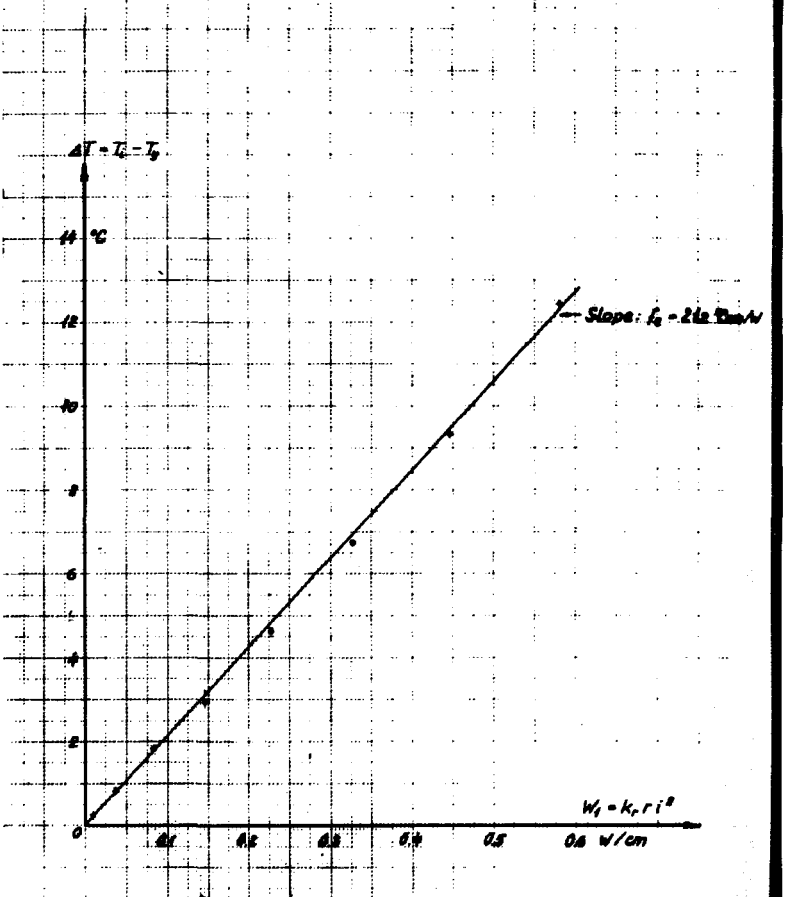

3.2.3. Results

A typical isothermal measurement result is shown in fig. 22 which is a cut of the ΔT-recorder paper. The recorder sensitivity and zero adjustment were checked daily during the measurement series.

A rough scan of the rod temperature during the measurements was made by switching the fixed rod and thermocouple to a separate recorder during each 10 cm movement, where the thermocouple was not in use for the delta temperature measurement. These scans showed that the rod temperatures were about the same, 70 - 100°C, as during the calibrations. In that temperature range the thermocouple sensitivity is fairly constant, see fig. 16, about 42.2 μV/°C, which is why this figure is used in all measurements for the relation between ΔT and the recorder paper readings. The conversion ratios obtained from the sensitivities in table 3.2.4 are

Table 3.2.5

Conversion ratios

Recorder range		1.2 V (2.370 °C/cm)	0.6 V (1.185 °C/cm)
Conversion	I6/7	0.287	0.143
Ratio in	I6/8	0.275	0.138
W/g · cm	I6/9	0.289	0.145

The measured nuclear heat is split into material dose rate and position dose rate in accordance with their definitions in 2.1.2. By means of the thermal and fast values and the calculated conversion factors from tables 2.5.13 and 2.5.14 the material dose rates are found.

Some characteristic results are given in table 3.2.6 and plotted in figs. 37 - 43. These results were selected among several hundred measurements on the basis of the criteria that

(1) The measurements are made in fuel elements of the Mk. 4/9 type with an actual U235 content of about 100 g. The Mk. 4/9 type contains initially 115 g U235.

(2) There is one representative from each of the seven fuel element groups, the elements in each group having the same distance to the vertical core centre axis.

Figure 22

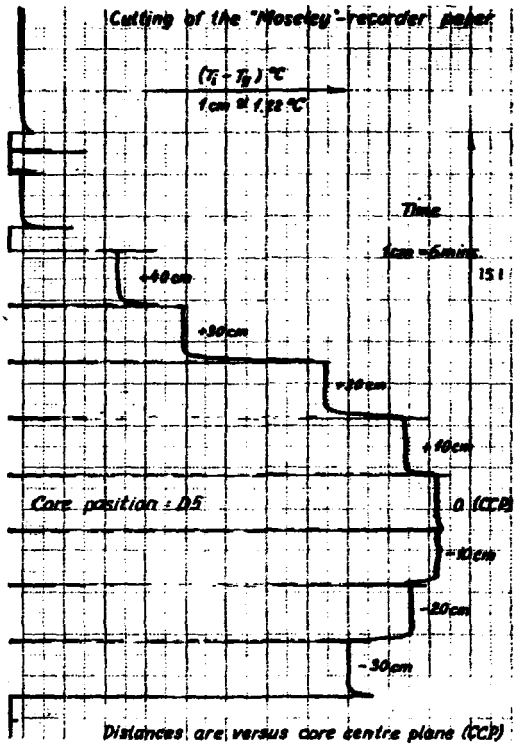

Nuclear heat in fuel element No 4667 with 96 g U^{nat} left at October 10th, 1970. Measured by means of the isothermal rod calorimeter I6/9.

Figure 16

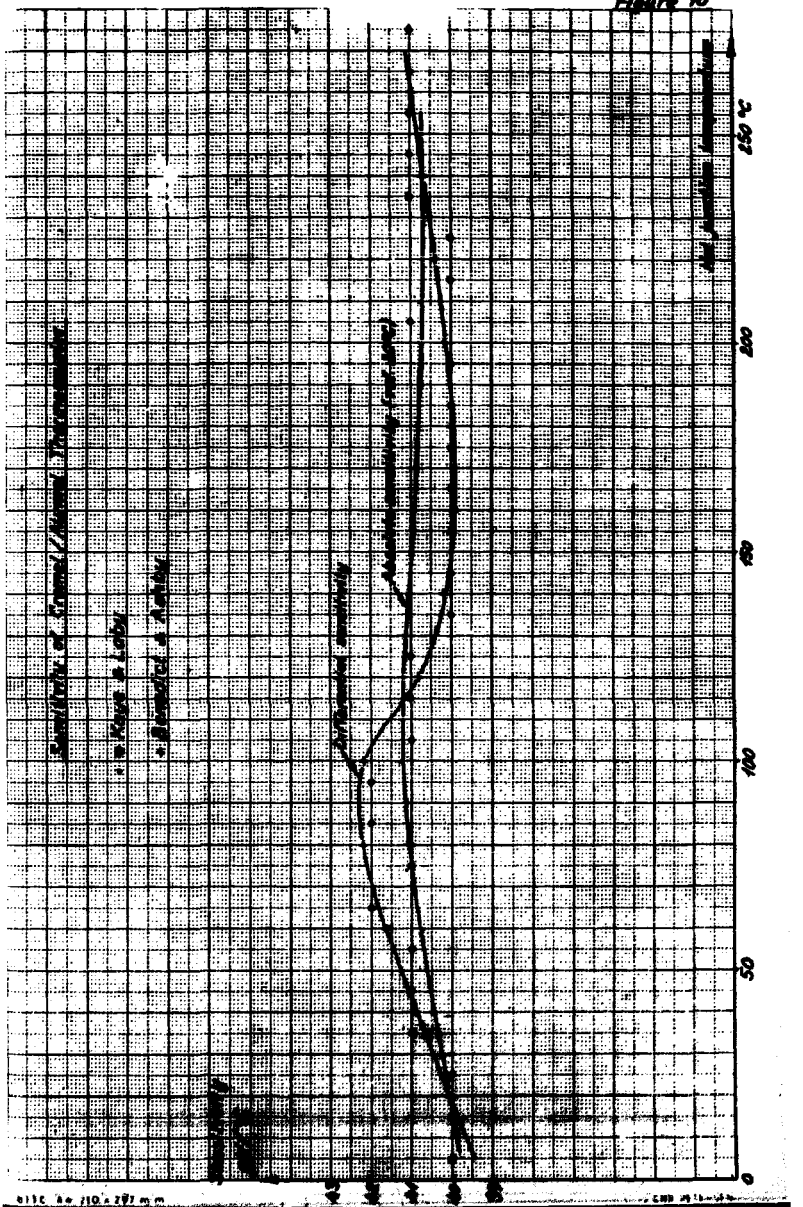

FIGURE NO. 3

REAKTOR DR - 3.

NUCLEAR HEAT IN C3 (GROUP NO.1)

MEASUREMENT DATA. PERIOD No 121

CALORIMETER	I6/9
COMPUTED POWER.	206 MW
CCA. ANGLE.	24° 168
U^{235} CONTENT	181,2 G
DATE OF MEASUREMENT.	18/6 - 70
CORE CONFIGURATION No.	156

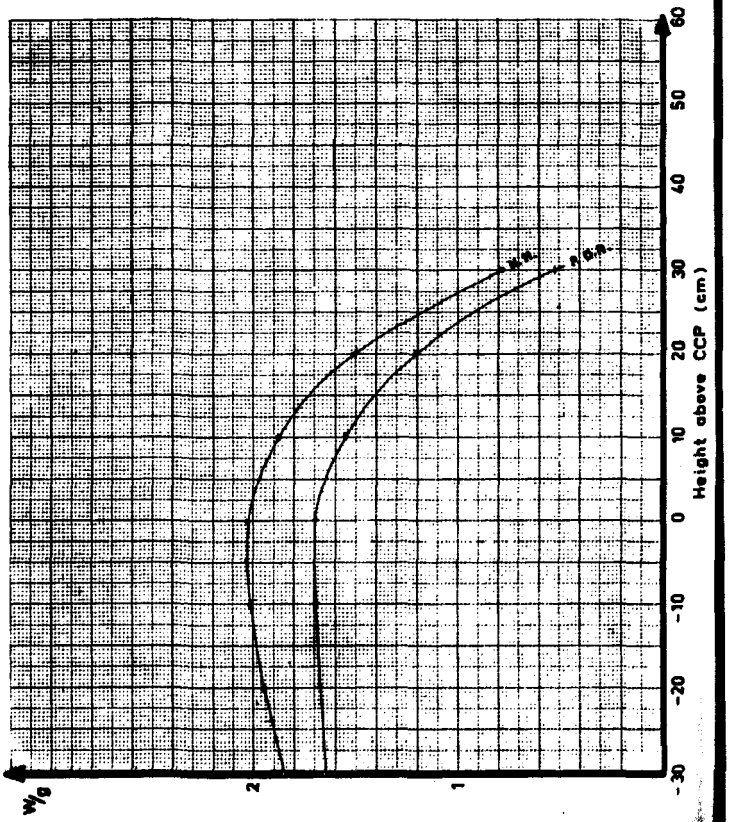

FIGURE NO. 38

REAKTOR DR - 3.

NUCLEAR HEAT IN DA (GROUP NO. 2)

MEASUREMENT DATA. PERIOD No 125

CALORIMETER.	16/9
COMPUTED POWER.	200 MW
CCA. ANGLE.	22° 000
U^{235} CONTENT	101,16
DATE OF MEASUREMENT	10/10 - 70
CORE CONFIGURATION No.	154

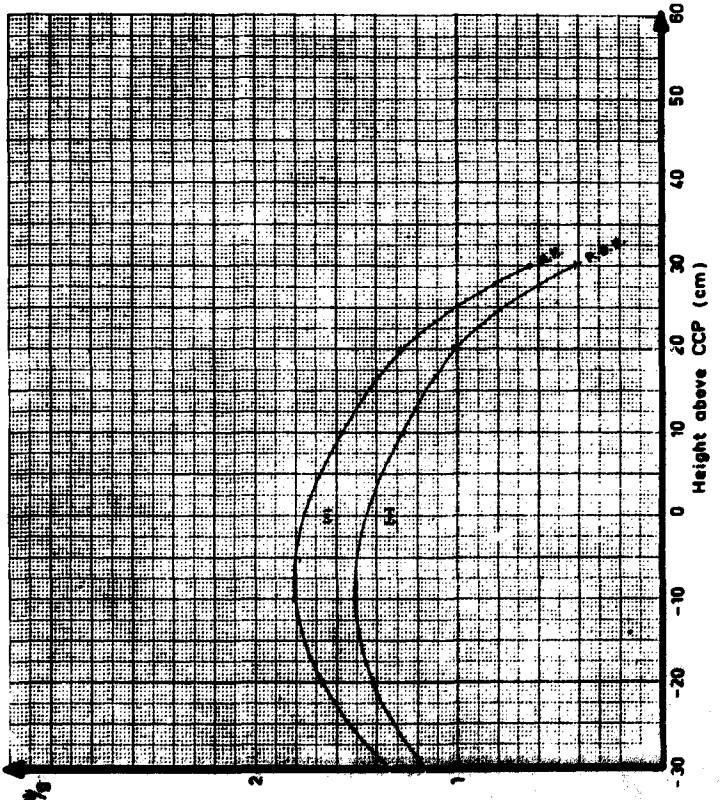

REAKTOR DR - 3.

NUCLEAR HEAT IN CS (GROUP NO. 3)

MEASUREMENT DATA. PERIOD No. 129

CALORIMETER.	IG/8
COMPUTED POWER.	10.11 MW
CCA. ANGLE.	10°440
U^{235} CONTENT	102.8 G
DATE OF MEASUREMENT.	3/5 - 70
CORE CONFIGURATION No.	149

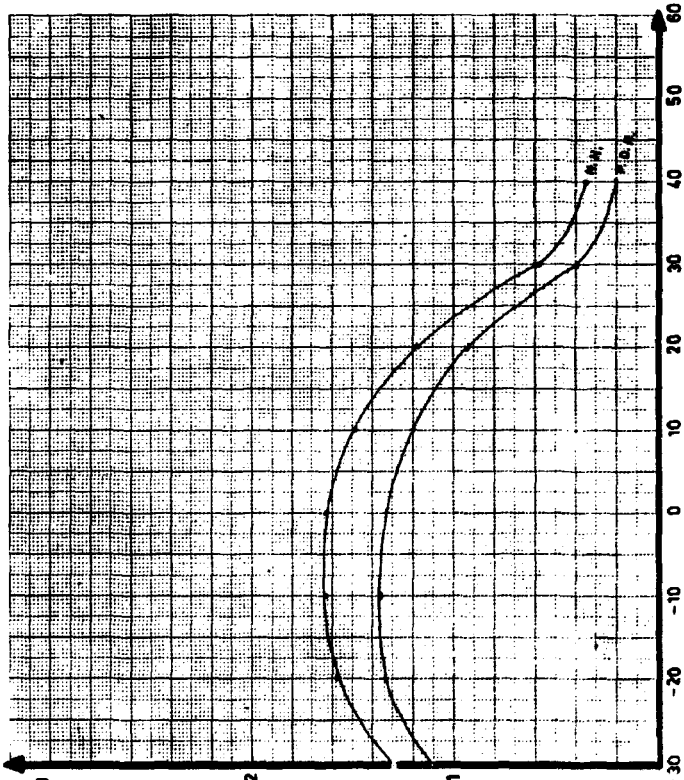

FIGURE NO. 49

REAKTOR DR - 3.

NUCLEAR HEAT IN D2O (GROUP NO. 4

MEASUREMENT DATA.

PERIOD No. 124

CALORIMETER.	I 8/9
COMPUTED POWER.	886 MW
CCA. ANGLE.	19°832
U^{235} CONTENT	1880
DATE OF MEASUREMENT.	27/8 - 70
CORE CONFIGURATION No.	193

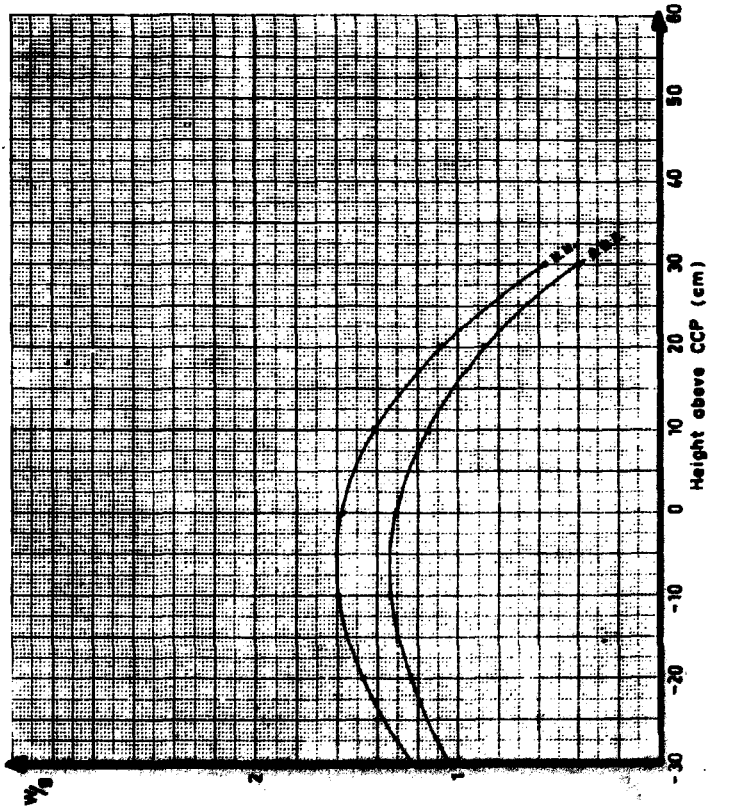

FIGURE NO. 8

REAKTOR DR - 3.

NUCLEAR HEAT IN A2 (GROUP NO. 5)

MEASUREMENT DATA. PERIOD No. 184

CALORIMETER.	IG/9
COMPUTED POWER	884 MW
CCA. ANGLE.	25°000
U^{235} CONTENT	90,6 G
DATE OF MEASUREMENT	10/9 - 70
CORE CONFIGURATION No.	153

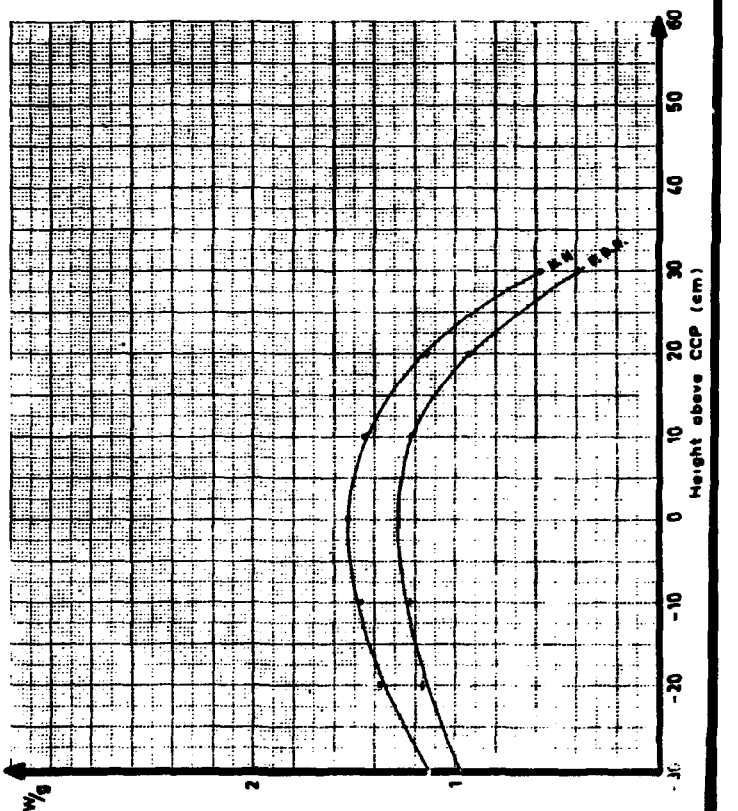

FIGURE NO. 42

REAKTOR DR - 3.

NUCLEAR HEAT IN E1 (GROUP NO. 6)

MEASUREMENT DATA.

PERIOD No. 124

CALORIMETER	I6/8
COMPUTED POWER.	924 MW
CCA. ANGLE.	25°100
U^{235} CONTENT	1045 G
DATE OF MEASUREMENT.	9/8 - 70
CORE CONFIGURATION No.	153

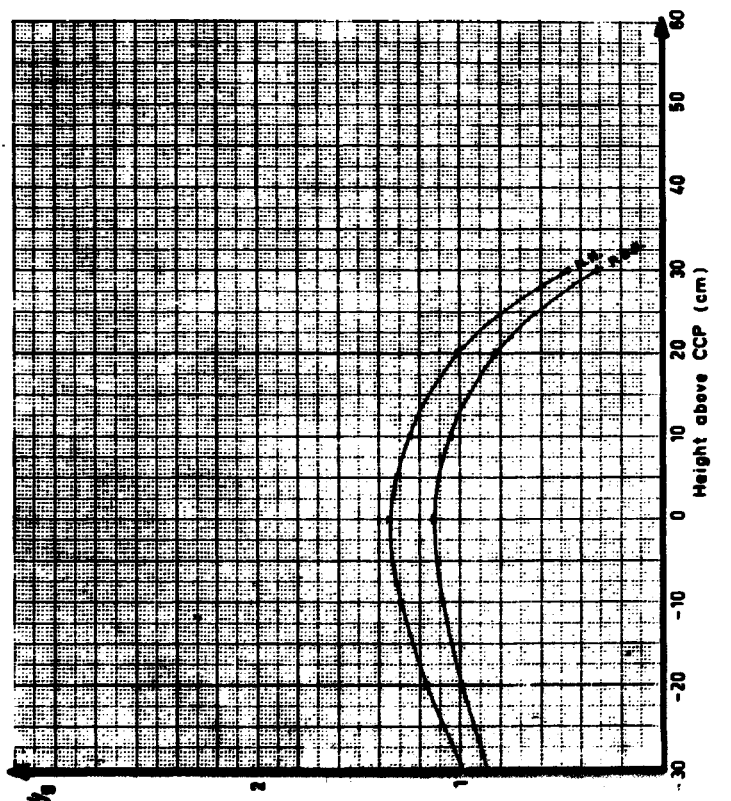

FIGURE NO. 13

REAKTOR DR - 3.

NUCLEAR HEAT IN Be (GROUP NO.7)

MEASUREMENT DATA. PERIOD No 125

CALORIMETER.	26/9
COMPUTED POWER.	980 MW
CCA. ANGLE.	18° 966
U^{235} CONTENT	101,3 G
DATE OF MEASUREMENT.	26/9 - 70
CORE CONFIGURATION No.	154

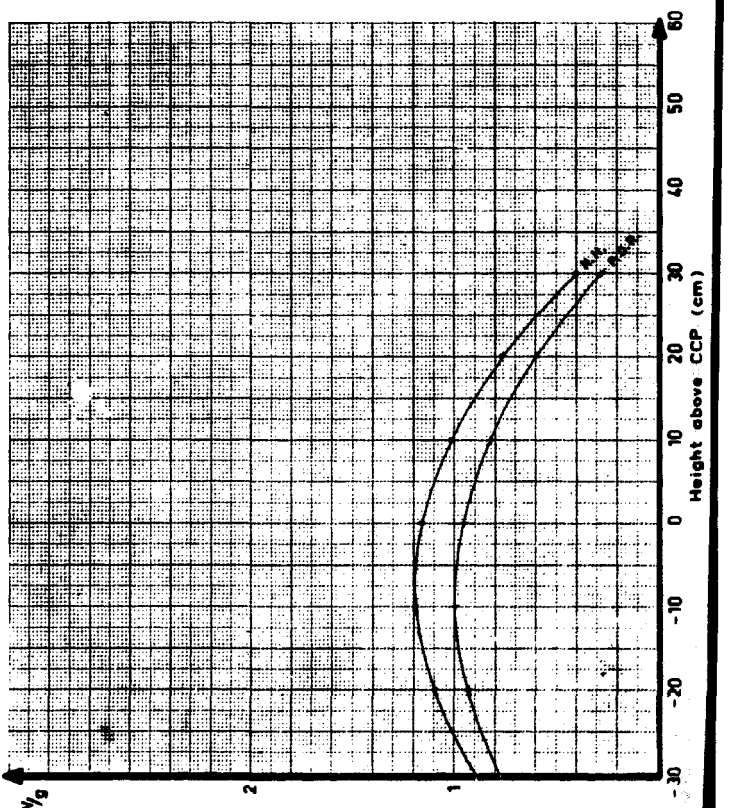

The results were treated by the Burroughs B 6700 computer by means of code No. P 630: DOSESEPARATION. In table 3.2.6 is given outputs of P 630. The symbols used are:

KTEMP	Conversion ratio W/g per cm as listed in table 3.2.5.
KTERM	Thermal-neutron material dose factor in mW/g per 10^{14} n/cm^{2}sec as listed in table 2.5.23.
KFAST	Fast-neutron material dose factor in mW/g per 10^{14} n/cm^{2}sec as listed in table 2.5.14.
KP	Reactor run No.
DAY	Day No. in the reactor run when the measurement was made.
POS. NO.	Core position No. (A1 = 1, A2 = 2, ... E4 = 26).
ELNO	Manufacturing No. of the fuel element.
KPLENGTH	Number of days of the actual reactor run.
CAM NO.	Vertical position identification (1 = -30 cm, 2 = 20 cm, ... 8 = +40 cm above core centre plane).
DELTATP	Delta temperature measured by the I6-calorimeter in terms of "cm recorder paper reading".
TFLUX	Thermal flux in terms of 10^{14} n/cm^{2}sec.
FFLUX	Fast flux in terms of 10^{14} n/cm^{2}sec.
MATDOSE	Material dose.
POSDOSE	Position dose.
USTART	U235-content at start of the reactor run.
USTOP	U235-content at end of the reactor run.
UVAEGT	U235-content at time of measurement.

Table 3.2.6

Dose rates in the fuel element groups with 100 g U235-content

KP 121 DAY 20 POS NO 13 ELNO 4993 KPLENGTH 23.5

CAM NO	DELTATP	TFLUX	FFLUX	MATDOSE	POSDOSE
1	12.76	1.248	0.049	0.195	1.655
2	13.44	1.282	0.259	0.277	1.672
3	13.68	1.430	0.330	0.324	1.689
4	14.04	1.484	0.350	0.339	1.697
5	12.96	1.423	0.345	0.328	1.551
6	10.40	1.260	0.317	0.295	1.213
7	5.38	1.215	0.240	0.260	0.520
8	0.00	0.000	0.000	0.000	0.000

MEAN POS DOSE = 1.428 UPOSDOSE RATIO MEAN = 70.9
UPOSDOSE RATIO CCP = 59.7
USTART = 115.4 USTOP = 98.8 UVAEGT = 101.3

KP 125 DAY 22 POS NO 20 ELNO 4997 KPLENGTH 23.5

CAM NO	DELTATP	TFLUX	FFLUX	MATDOSE	POSDOSE
1	9.21	1.169	0.045	0.182	1.153
2	11.51	1.186	0.240	0.256	1.413
3	12.45	1.321	0.306	0.300	1.506
4	11.32	1.369	0.324	0.313	1.328
5	10.78	1.304	0.319	0.302	1.261
6	8.79	1.145	0.293	0.270	1.005
7	4.41	1.078	0.222	0.234	0.405
8	0.00	0.000	0.000	0.000	0.000

MEAN POS DOSE = 1.153 UPOSDOSE RATIO MEAN = 67.6
UPOSDOSE RATIO CCP = 76.1
USTART = 115.0 USTOP = 100.1 UVAEGT = 101.1

KP 120 DAY 2 POS NO 15 ELNO 4662 KPLENGTH 23.5

CAM NO	DELTATP	TFLUX	FFLUX	MATDOSE	POSDOSE
1	8.91	1.225	0.042	0.189	1.103
2	10.85	1.105	0.222	0.238	1.335
3	11.23	1.185	0.283	0.272	1.357
4	11.20	1.275	0.300	0.291	1.333
5	10.24	1.240	0.296	0.284	1.200
6	8.13	1.090	0.272	0.254	0.925
7	4.10	0.905	0.206	0.204	0.391
8	2.39	0.890	0.054	0.146	0.200

MEAN POS DOSE = 1.092 UPOSDOSE RATIO MEAN = 94.0
UPOSDOSE RATIO CCP = 77.0
USTART = 103.8 USTOP = 90.0 UVAEGT = 102.6

KP 124 DAY 6 POS NO 18 ELNO 4998 KPLENGTH 23.5

CAM NO	DELTATP	TFLUX	FFLUX	MATDOSE	POSDOSE
1	8.41	1.136	0.037	0.175	1.045
2	10.12	1.116	0.199	0.231	1.236
3	11.01	1.195	0.253	0.262	1.334
4	10.87	1.200	0.266	0.268	1.309
5	9.70	1.164	0.264	0.265	1.142
6	7.53	0.876	0.243	0.213	0.879
7	3.90	0.727	0.184	0.171	0.395
8	0.00	0.000	0.000	0.000	0.000

MEAN POS DOSE = 1.048 UPOSDOSE RATIO MEAN = 94.4
UPOSDOSE RATIO CCP = 75.7
USTART = 102.3 USTOP = 89.2 UVAEGT = 99.0

KP 124 DAY 20 POS NO 2 ELNO 8665 KPLENGTH 23.5

CAN NO	DELTATP	TFLUX	FFLUX	RATDOSE	POSDOSE
1	7.74	0.931	0.034	0.145	0.978
2	9.43	0.958	0.181	0.202	1.165
3	10.10	1.070	0.230	0.236	1.228
4	10.56	1.104	0.244	0.246	1.285
5	9.99	1.053	0.241	0.238	1.211
6	7.87	0.932	0.221	0.213	0.928
7	3.98	0.925	0.167	0.192	0.385
8	0.00	0.000	0.000	0.000	0.000

MEAN POS DOSE = 1.026 UPOSDOSE RATIO MEAN = 97.1
UPOSDOSE RATIO CCP = 77.5
USTART = 110.6 USTOP = 97.7 UVAEGT = 99.6

KP 124 DAY 19 POS NO 23 ELNO 49107 KPLENGTH 23.5

CAN NO	DELTATP	TFLUX	FFLUX	RATDOSE	POSDOSE
1	6.81	0.810	0.030	0.126	0.861
2	8.05	0.833	0.158	0.176	0.991
3	8.96	0.931	0.201	0.206	1.093
4	9.33	0.960	0.213	0.214	1.139
5	8.61	0.916	0.210	0.207	1.042
6	6.99	0.811	0.193	0.186	0.828
7	3.34	0.805	0.146	0.168	0.317
8	0.00	0.000	0.000	0.000	0.000

MEAN POS DOSE = 0.896 UPOSDOSE RATIO MEAN = 116.6
UPOSDOSE RATIO CCP = 91.8
USTART = 114.1 USTOP = 102.2 UVAEGT = 104.5

KP 125 DAY 7 POS NO 10 ELNO 49105 KPLENGTH 23.5

CAN NO	DELTATP	TFLUX	FFLUX	RATDOSE	POSDOSE
1	6.16	0.810	0.028	0.125	0.768
2	7.58	0.820	0.147	0.170	0.929
3	8.24	0.923	0.187	0.200	0.995
4	8.00	0.945	0.198	0.207	0.953
5	7.00	0.851	0.195	0.192	0.823
6	5.26	0.685	0.179	0.163	0.600
7	2.76	0.517	0.136	0.123	0.277
8	0.00	0.000	0.000	0.000	0.000

MEAN POS DOSE = 0.764 UPOSDOSE RATIO MEAN = 132.7
UPOSDOSE RATIO CCP = 106.3
USTART = 104.1 USTOP = 94.7 UVAEGT = 101.3

In the cases where one or more of the input values of table 3.2.6 were lacking, 0.000 is stated.

The curve shapes are dependent on the CCA-angle, as expected. The shape changes also at the core borders, i.e. at +30 and -30 cm above the core centre plane (CCP).

As a major part of the nuclear heat is Y-heat from the fissions and the fission products of short life, the position dose rate is strongly dependent on the power release in the fuel element itself and in the nearest fuel elements.

The power release in a fuel element increases with increasing U235-content. Consequently the position dose rate should behave similarly.

An example is shown in fig. 44 where the mean position dose rates measured during the in-core life of fuel element no. 4994 are plotted versus the U235-content. The fuel element was placed in position A4 and had an initial content of 115 g U235. The deviations from a smooth curve are mainly caused by changes in the fuel contents of the surrounding fuel elements and the position of the coarse-control arms. Measurements in a dummy fuel element (0 g U235) in D4 in reactor run 124 showed that the contribution from the surrounding elements to the position dose rate amounts to about 45% of the mean position dose rate.

Statistics based on a few measurements in each core position indicate that the mean slope of the linear regression curves of position dose rates versus the U235-content in the respective elements is

0.0035 W/g per g U235.

A line with this slope is also shown in fig. 44.

Figure 44.

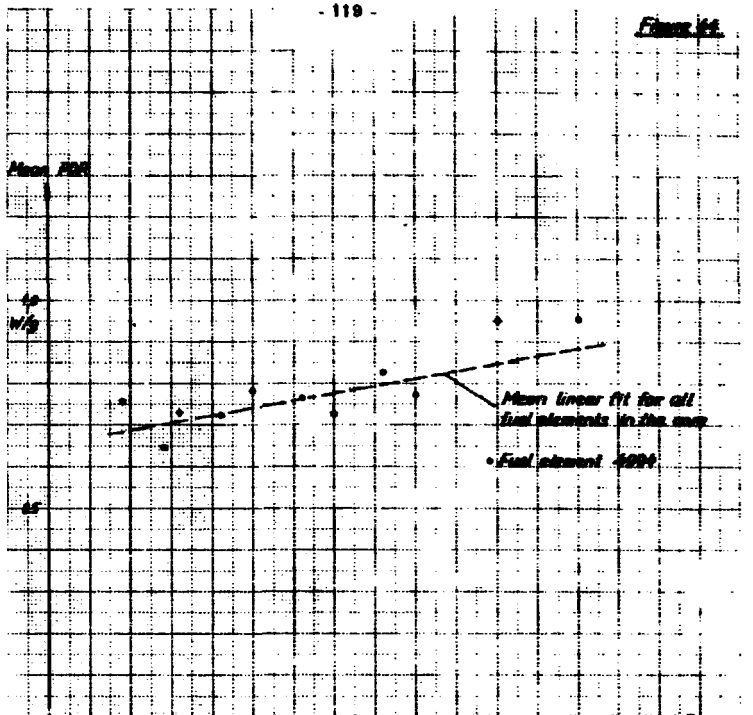

Mean Positive Power Ratio (PPR) Variation through the In-Core Life of Fuel Element No 4094 in Position H4.

Table 3.2.7

Mean position dose rate variation through the in-core life fuel element No. 4994 in position A4

Reactor run No.	Day No.	Mean position dose rate (W/g)	U235 weight in A4 (g)
121	2	0.954	115
121	22	0.951	105
122	19	0.773	95
123	5	0.826	91
123	19	0.725	85
124	6	0.766	81
124	20	0.782	75
125	6	0.722	71
125	20	0.731	66
126	5	0.647	64
126	19	0.780	59

In spite of the thorough calibrations of the calorimeters as described in 3.2.2, the three serial nos. 7, 8 and 9 of the I6-type apparently give deviating responses. This is discovered by comparison of all measurements in each of the fuel elements, where the results fall into three groups, each belonging to one of the calorimeter serial numbers.

The reason may be that the three calorimeters perform differently in spite of their identical geometrical construction and their nearly merging calibration curves. Investigations going on at the moment (January 1972) concern the heat conductions at the insulated hot junctions of the thermocouples. The nuclear heat may raise temperature gradients here during in-pile measurements, large enough to explain the deviations.

However, the explanation might also be the quite simple one that the nuclear heat has actually changed from the time when I6/7 was in operation to the time when I6/8 was in operation and further on to I6/9 owing to the changes in core configuration and rig load.

4. UTILIZATION OF RESULTS FOR PREDICTION OF NUCLEAR HEAT

4.1. Need for Dose Separation

Division of nuclear heat into position and material dose rates facilitates an accurate prediction of nuclear heat in a reactor experiment.

The position dose rate in a selected experiment hole is independent of the experiment installed in the hole as long as heavy gamma-absorbing materials are not present in the rig construction. This implies that the position dose rates measured by means of the γ-calorimeters can be used directly in most cases.

The material dose rate depends on the choice of materials in the rig, the weight of the materials and their assembly. Therefore the material dose rates differ from rig to rig, and those of the calorimeters are generally not applicable to the rig design. However, the methods of calculating the material dose rates in the calorimeters are applicable to rig design. A guide on material dose rate calculations for rigs will be given in the following pages.

In some cases an exact prediction of the nuclear heat is not necessary. An example is a rig containing fissile material where the nuclear heat is only a minor fraction of the total heat deposition in the rig. In that case the uncorrected nuclear heat as it is measured by one of the calorimeters may be a sufficiently good approximation to the nuclear heat in the rig.

4.2. Calculation of the Position Dose Rate in a Rig

Tables 3.1.1 and 3.2.6 give the vertical distribution of the position dose rates in the experimental holes outside and inside the core respectively. The units are watts per gram of material, and as the mass γ-absorption coefficients of the conventional rig construction elements are nearly equal in the energy range 1 - 3 MeV, which is predominant in the γ-spectrum of the reactor, the position dose rate fraction of the heating can be found simply by multiplying the position dose rate value from the table by the mass of the element in grams.

If very heavy rig structures are used, the γ-field may be perturbed and the dose rate will be smaller than that calculated as above. This deviation will not be calculated here because heavy rig structures are infrequent as they are unwanted from a reactivity-consumption point of view.

4.3. Calculation of the Material Dose Rate in a Rig

The most convenient procedure is to classify the rig construction in groups of either cylindrical or plane shape and calculate for each element in the groups the heat deposition

(a) from the other components, and

(b) from the component itself.

Each component should consist of only one material, and it should be concentric to the vertical rig axis. In practice, all major components in rigs can be classified in this way by a good approximation.

As the material dose rate comprises the heating by the radiation from interactions between the thermal and fast fluxes and the rig structure, the following reactions should be considered:

(1) Thermal neutron capture

(2) Decay of nuclei produced by thermal-neutron capture

(3) Fast-neutron reactions.

Only the common (n, γ)-reaction and $(\beta^- + \gamma)$-decay will be considered here. Materials in which reactions and decays are accompanied by release of α-particles or protons are seldom used in rig constructions as they entail very high heating rates.

The calculations are performed by treating each of the components in the rig assembly in turn as a target for the emission from the component itself as well as from the remaining rig components.

The deductions of the formulas are similar to those in 2.2, 2.3 and 2.4 where the calorimeter sample was the "target" component.

The following symbols are used:

Q - number of components in the rig assembly

I - number of isotopes in component no. q

K - number of decay modes of isotope no. i

J - number of intervals in β-spectrum of decay mode no. k

Δ_j - length of interval no. j in a β-spectrum (MeV)

E_j - mean energy of β-particles in Δ_j (MeV)

N_j - number of β-particles in Δ_j

E_{bi} - binding energy of the last neutron in isotope no. (i+1) (MeV)

X - probability that protons released in a component will be absorbed in the component itself

μ_{ea} - linear γ-energy absorption coefficient (cm^{-1})

b_{ntj} - fraction of β-energy expelled from the n'th towards the t'th component which is not absorbed by intermediate structure layers

d - fraction of β-energy released in the t'th component which is not absorbed in the component itself

M_t - mass of "target" component (g)

M_n - mass of "emitter" component (g)

G_{nt} - geometry factor expressing the probability that a particle from the n'th component will be expelled in the direction of the t'th component

A_i - atomic weight of isotope no. i

σ_{ai} - thermal-neutron cross section (Westcott) of isotope no. i (barns)

P_i - natural mass abundance of isotope i

φ_{th} - thermal-neutron flux (Westcott) (n/cm^2s)

φ_γ - fast-neutron flux (n/cm^2s)

u - lethargy, defined by $u \equiv \ln \frac{E_o}{E}$

E_o - reference level of the neutron energy E

$\varphi_{(u)}$ - neutron flux per unit lethargy interval

$\sigma_{(u)}$ -neutron cross section at lethargy u.

The total material dose rate in an assembly is the sum of contributions (a) through (f), viz.

(a) Heat from thermal-neutron capture in the components themselves:

$$\Delta W_{Ctt} = 9.65 \cdot 10^{-14} \varphi_{th} \sum_{q=1}^{Q} \sum_{i=1}^{I} \left(\frac{M_q}{M_i} D_i E_{bi} X_i \right) W/g,$$

where

$$D_i = \frac{\sigma_{ai} P_i}{A_i} \qquad (72)$$

(b) Heat from thermal-neutron capture in the other components of the assembly:

$$\Delta W_{Cnt} = 9.65 \cdot 10^{-14} \varphi_{th} \sum_{q=1}^{Q} \sum_{i=1}^{I} \left(\frac{M_{ni}}{M_t} G_{nt} D_i E_{hi} \mu_{eal} \right) W/g. \quad (73)$$

(c) Heat from decay in the components themselves:

$$\Delta W_{Dtt} = 9.65 \cdot 10^{-14} \varphi_{th} \sum_{q=1}^{Q} \sum_{i=1}^{I} \left(\frac{M_{ti}}{M_t} D_i \sum_{k=1}^{K} ((1-d) \sum_{j=1}^{J} (N_j E_j \lambda_j) + \right. \quad (74)$$

$$\left. + N_k E_k X_k \right)) W/g.$$

(d) Heat from decay in the other components of the assembly:

$$\Delta W_{Dnt} = 9.65 \cdot 10^{-14} \varphi_{th} \sum_{q=1}^{Q} \sum_{i=1}^{I} \left(\frac{M_{ni}}{M_t} G_{nt} D_i \sum_{k=1}^{K} \sum_{j=1}^{J} (N_j \lambda_j E_j \lambda_{ntj}) + \right. \quad (75)$$

$$\left. + N_k E_k X_k \right)) W/g.$$

(e) Heat from fast-neutron elastic scattering:

$$\Delta W_{Sc.el.} = \sum_{q=1}^{Q} \sum_{i=1}^{I} \left(\frac{19.32 \cdot 10^{-14} \varphi_f}{(A_i+1)^2} \int_{u_1}^{u_2} \varphi(u) \sigma_{Sc.el.}(u) du \right) W/g. \quad (76)$$

(f) Heat from fast-neutron inelastic scattering:

$$\Delta W_{Sc.el.} = \sum_{q=1}^{Q} \sum_{i=1}^{I} (0.3575 \cdot 10^{-14} \varphi_f \int_{0}^{u_1} \varphi(u) \sigma_{Sc.il.}(u) du) W/g. \quad (77)$$

In practice a number of approximations are made to the thorough calculation procedure outlined above, because generally the results are not wanted with this amount of accuracy.

A proposal for a rather good approximation is that of treating the rig assembly as a solid cylinder or sphere containing a uniform mixture of the masses of the isotopes present in the rig. The relative loss of β-energy from a cylinder or sphere with a diameter of more than 3 cm will be negligible. The self-capture probability of photons released in the rig can be found by means of fig. 14 when the mean linear mass absorption coefficient of the isotope mixture is calculated. The summations on the β-spectra may be avoided by using a mean β-energy: 0.3 - 0.5 times the tabulated maximum energy (acc. to (15)).

5. ACKNOWLEDGEMENTS

For valuable assistance during the early planning and construction of the calorimeters I am grateful to Mourits Nielsen of the Physics Department and B. Bukholt of the Engineering Department at Risø.

The complicated construction of calorimeter A25/2 was successfully performed by J. Olsen, DR 3.

The I6-type calorimeters were manufactured at DR 3 by Ole Pedersen and, later, by Steen E. Nielsen who also maintained the equipment and made modifications to permit the operation of the gear device, advised by K. Petersen.

For valuable assistance during the design and maintenance of the instrumentation I am indebted to Frode Hansen of the Electronics Department, Risø, and to J. E. Jørgensen, F. Carlsen, and S. E. Jensen, DR 3.

With the inventive and enthusiastic co-operation of P. Wiig, the measurements with the A25/2-calorimeter were successfully carried out.

The measurements with the I6-calorimeters were carefully undertaken by the rig operators on the reactor shifts: B. S. Andersen, S. E. Christensen, Aage H. Pedersen, H. Rask, W. Søndergaard Hansen, and W. Westborg.

I take this opportunity to thank the persons mentioned above and all members of the staff of DR 3 who took part in the calorimetric measurements.

6. REFERENCES

1) C. M. Davisson and R. D. Evans, Gamma-Ray Absorption Coefficients. Rev. Mod. Phys. 24 (1952) 79-107.

2) Tables for the Analysis of Beta Spectra. Reprinted. (National Bureau of Standards, Applied Mathematics Series, 13). (USGPO, Washington D. C., 1962). 61 pp.

3) C. H. Hogg, Y-Heating Measurements in the MTR. IDO-16093 (1955). 11 pp.

4) K. M. Case et al., Introduction to the Theory of Neutron Diffusion, 1 (Los Alamos Scientific Laboratory, Los Alamos, 1953).

5) W. F. Witzig, WAPD-1 Experiments in the Materials Testing Reactor. I. Gamma Heating WAPD-1-1. WAPD-79 (1955). 31 pp.

6) Samuel Glasstone, Principles of Nuclear Reactor Engineering. (Macmillan, London, 1956). 861 pp.

7) D. M. Richardson, A. O. Allen, and J. W. Boyle, Dosimetry of Reactor Radiation by Calorimetric Measurement. In: Proceedings of the 1st International Conference on the Peaceful Uses of Atomic Energy, Geneva, 8-20 August 1955, 14 (United Nations, New York, 1955-58) 209-212.

8) T. Rockwell (editor), Reactor Shielding Design Manual. (Van Nostrand, New York, 1956). 472 pp.

9) S. Glasstone and M. C. Edlund, The Elements of Nuclear Reactor Theory. (Van Nostrand, Princeton N. J., 1957). 416 pp.

10) F. T. Binford, Gamma-Ray Heating in BSR. Nucleonics 15, No. 3 (1957) 93-97.

11) D. J. Hughes and R. B. Schwartz, Neutron Cross Sections, 2nd Edition, (BNL-325). (Brookhaven National Laboratory, Upton N. Y., 1958) 373 pp.

12) N. G. Goosev et al., Gamma Radiation Inside and Outside Extended Sources. In: Proceedings of the 2nd United Nations International Conference on the Peaceful Uses of Atomic Energy, Geneva, 1-3 September 1958, 21 (IAEA, Vienna, 1958) 122-130.

13) H. S. Carslaw and J. C. Jaeger, Conduction of Heat in Solids, 2nd edition. (Clarendon Press, Oxford, 1959). 510 pp.

14) L. V. Groshev et al., Atlas of γ-Ray Spectra from Radioactive Capture of Thermal Neutrons. (Pergamon Press, London, 1959). 198 pp.

15) M. F. James et al., Average Electron Energy in Beta Decay. AERE-M-640 (1960). 20 pp.

16) K. L. Hall et al., Reactor Monitoring by Calorimetry. In: Materials in Nuclear Applications, San Francisco, Calif., 12-16 October 1959. (ASTM Special Technical Publication, 276). (American Society for Testing Materials, Philadelphia, 1960). 30-39.

17) A. R. Anderson and R. J. Waite, A Calorimeter for Measuring Energy Absorption from Pile Radiation. J. Sci. Instrum. 33 (1956) 46-51.

18) S. B. Wright, Calculation of High Energy Neutron Spectra in Heterogeneous Reactor Systems. AERE-R-4080 (1962). 34 pp.

19) L. D. Weber and C. H. Hogg, MTR Gamma Heat Generation Measurements. IDO-16652 (1961). 39 pp.

20) A. R. Anderson and J. K. Linacre, Calorimetric Dosimetry of Reactor Radiation. In: Selected Topics in Radiation Dosimetry, Vienna, 7-11 June 1960. (IAEA, Vienna, 1961) 609-621.

21) B. Petree and G. Ward, The Construction of Calorimeters for the Measurement of Absorbed Dose. NBS-TN-163 (1962). 34 pp.

22) A. K. Dickson, Nuclear Heating of Non-Fissile Material by Thermal Neutron Reactions. TRG-Report-322 (1962). 16 pp.

23) Radiation Quantities and Units. International Commission on Radiological Units and Measurements (ICRU), Report 10A. (National Bureau of Standards Handbook, 84). (National Bureau of Standards, Washington D. C., 1962).

24) G. Constantine and J. Needham, Nuclear Heating Measurements in Reactors. AERE-R-4368 (1963). 43 pp.

25) C. C. Minter, Effect of Pressure on the Thermal Conductivity of a Gas. AD-298 999 (1963). 21 pp.

26) W. Suckow, Bestimmung der Strahlenfelder in den Bestrahlungskanälen des Rossendorfer Forschungsreaktors. ZfK-RN-21 (1963). 36 pp.

27) N. M. Lazar et al., Calorimetric Methods for the Assay of Fuel Pins and Residues. ANL-6771 (1964). 35 pp.

28) R. Dehn, Measurement of Gamma Heating in D. F. R. TRG-Report-844 (1964). 9 pp.

29) B. Asphaug, Gamma Thermometer Development at HBWR. In: Development and Applications of In-Core Instrumentation at HBWR, Oslo, 15-19 June 1964, I, (HPR-35) - (OECD, Halden Reactor Project, 1964) Section 7.

30) J. Brun, Calorimetre Adiabatique a vide statique pour la mesure d'echauffements de materiaux en pile. CEA-R-2581 (1964). 57 pp.

31) Z. Kovar, Les methodes calorimetriques dans la dosimetrie des rayonnements ionisants. II. X-(Traduction)-567 (1962). 13 pp.

32) J. de Goer et al., Dosimetrie du rayonnement complexe de pile par une technique calorimetrique. CEA-R-2443 (1964). 26 pp.

33) H.G. Lipson and L.O. Bouthillette, Epoxy Vacuum Seal for Introduction of Leads into Cryogenic Equipment. AFCRL-63-78 (1963). 4 pp.

34) S.R. Gunn, A Large-Volume Radiometric Calorimeter. UCRL-7490 (1963). 9 pp.

35) S.R. Gunn, A Rod-Conduction Radiometric Calorimeter. UCRL-7488 (1963). 9 pp.

36) S.R. Gunn, An In-Reactor Radiometric Calorimeter. UCRL-7489 (1963). 12 pp.

37) J.-R. Puig and F. Romano, Le dosimetre calorimetrique Calvet. CEA-R-2768 (1965). 16 pp.

38) T. Linacre, Calorimetric Dosimetry for Reactor Irradiation Experiments. AERE-R-4805 (1965). Part 1-3.

39) K.W. Foster, Gamma *Self-Absorption in a Spherical* Distributed Gamma Source. MLM-1219 (1965). 10 pp.

40) J. de Goer, Microcalorimetres pour mesure d'energie nucleaire en pile. In: Societe Europeenne de l'Energie Atomique: Annales du Colloque sur les procedes de mesures de flux associes aux dispositis d'irradiation dans les reacteurs de recherche et d'essais de materiaux, Grenoble, 15-17 Novembre 1965, 3 (Commissariat a l'Energie Atomique, Centre d'Etudes Nucleaires de Grenoble, Grenoble, 1966) No. 22.

41) J. Berger, Capsule d'Irradiation Cyrano etude nucleaire et thermique. Resultats des premieres mesures en pile. In: (as ref. 40) 3, No. 29.

42) M.J. Todd et al., A Calorimeter for Graphite Dose Rate in Advanced Gas-Cooled Reactors. In: (as ref. 40) 3, No. 24.

43) H. J. Leyers, Die Neutronen- und Gamma-Aufheizung in Experimentierkanälen des Reaktors FRJ-2. Nukleonik 7 (1965) 300-309.

44) K. Haack, Nuclear Heat Measurement in DR 3. In: (as ref. 40) 3, No. 26.

45) H. Lenders and F. Leonard, Mesures de rayonnements avec 3 sondes calorimetriques dans les cartouches combustible. In: (as ref. 40, 3, No. 27.

46) F. Ayela, Calorimetre differentiel a compensation electrique. In: (as ref. 40) 3, No. 23.

47) M. Wiegandt, Measurements with a Differential Calorimeter in an In-Pile Irradiation Position of the Swimming Pool Reactor. In: (as ref. 40) 3, No. 21.

48) J. Standring, Use of Small Isothermal Calorimeters to Measure the Radiation Dose Rate in CO_2/Graphite Rigs. In: (as ref. 40) 3, No. 25.

49) Personal Communication, 1967.

50) J. S. Stutheit, Fast-Response Gamma Thermometers. Nucl. Instrum. Meth. 63 (1968) 300-306.

51) B. Radak et al., Dosimetric Intercomparison Measurements in the Core of Reactor Isis at Saclay. Nucl. Applic. Tech. 7 (1969) 409-414.

52) R. L. Senn and W. R. Mixon, Experimental Measurement of Gamma Heat in the High Flux Isotope Reactor. Trans. Amer. Nucl. Soc., 12 (1969) 797-798.

53) K. Haack, Computer Code P.400: BETATAB. Risø-M-938 (1969). 11 pp. Internal report.

54) H. Kröckel, A Method for Determination of Convertible Nuclear Heating Data EUR-4415 (1970). 44 pp.

55) S. R. Gunn, Radiometric Calorimetry: A Review (1970 Suppl.) Nucl. Instrum. Meth. 85 (1970) 285-312.

56) A. W. Boyd and A. Keddar, Intercomparison of Reactor Calorimeters. At. Energy Rev. IAEA 8 (1970) 949-955.

57) J. Kott, The Development of Calorimetry in the Skoda Nuclear Power Plants Division. ZJE-70 (1970). 7 pp.

58) C. L. Fellers and J. D. Nutter, High-Wattage Twin Water Flow Calorimeter. Nucl. Instrum. Meth. 80 (1970) 192-196.

59) C.H. Hogg, Gamma-Ray Dosage Rate Measurement. IDO-16205 (1954). 17 pp.

60) W. Primak, Gamma-Ray Dosage in Inhomogeneous Nuclear Reactors. J. Appl. Phys. 27 (1956) 54-62.

61) P.J. Dyne and W. Thurston, A Calorimetric Determination of Energy Deposition in the J-Rod Annulus of the NRX Reactor. CRC-696 (AECL-432) (1957). 32 pp.

62) L.D. Weber and C.H. Hogg, MTR Gamma Heat Generation Measurements. IDO-16652 (1961). 39 pp.

63) C.D. Bopp and R.L. Towns, Calorimetric Measurement of Nuclear Heating in a Reactor. Nucl. Sci. Eng. 13 (1962) 245-249.

64) R.J. Howerton, Tabulated Neutron Cross Sections. Part 1: UCRL-5226 (1958). Part 2: UCRL-5351 (1958). Part 3: UCRL-5573 (1961).

APPENDIX

CALCULATION OF I-6 CALIBRATION FACTORS

The temperature conditions in the rod of the I6/7-calorimeter are calculated by means of the known physical constants. Allowance for the heat transport through the gas gap is made by dividing the rod into five sections, each of them having a uniform temperature distribution at the level of the mean temperature of the actual rod.

Introductorily, the temperature distribution along the rod without heat loss through the gas gap is calculated by means of eqs. (55), (56), (58), and (60) in subsection 3.2.2.

Assuming the calibration current $i = 0.5$ amp,
the heater resistance $r = 3.40$ +cm,
the thermal conductivity of aluminium $K = 2.00$ W/cm°C,
and the rod cross sections 0.124 cm^2 and 0.122 cm^2 with one and two cables respectively, we find

Position x (cm)	Temperature T (°C)	Temperature gradients at x-dx (°C/cm)	x+dx (°C/cm)
0.17 (x_v)	T_o	0	0
0.20 (x_1)	T_o-0.0015	-0.1028	-0.1045
1.03	T_o-1.278	-	-
1.86	T_o-4.934	-	-
2.69	T_o-10.971	-	-
3.52 (x_y)	T_o-19.376	-	-

(A2)

Curve I in fig. A1 is drawn through the plots of the temperatures calculated above. The curve is extrapolated in order to estimate the heat sink temperature, which is assumed to be the same as that of the calorimeter sheath.

By means of curve I an estimate of the real temperature distribution is made by iterations, considering the heat loss by conduction through the

gas gap (curve II).

The heat conduction from each rod section through the gas gap is found with the equation

$$Q_g = \frac{2\pi\lambda}{\ln\frac{d_2}{d_1}} \cdot \Delta T \text{ W/cm},$$

and the correction is introduced in the D-factor (see eq. (60) in subsection 3.2.2)

$$D = \frac{ri^2 - Q_g}{2K} = 0.2125 - 0.250\, Q_g \ ^\circ\text{C cm}$$

Rod section	Estimated gas gap temp. diff °C	Q_g (W/cm)	D (°C cm)	Corr. section border temp. (°C)	temp. grad. (°/cm)
				T_o	0
0	19.1	0.0905	0.1899		
				T_o-0.0014	-0.0930
I	18.7	0.0881	0.1905		
				T_o-1.147	-2.668
II	16.4	0.0776	0.1931		
				T_o-4.441	-5.27
III	11.8	0.0435	0.2016		
				T_o-9.882	-7.96
VI	5.0	0.0237	0.2066		
				T_o-17.65	-

The plot of the corrected section border temperatures is shown as curve III in fig. A1.

The heat transport by radiation may be calculated with the formula

$$Q = FC\left(\left(\frac{T_1}{100}\right)^4 - \left(\frac{T_2}{100}\right)^4\right) \text{ kcal/h} \quad \text{(ref. a)},$$

where the surface area of the irradiated body is F cm^2, the radiation coefficient is C kcal/cm^2 h°K, and T_1 °K and T_2 °K are the absolute temperatures of the radiating and the irradiated body respectively.

Considering rod section 1 (see fig. A1) we have

$$F = 0.55 \pi (1.02 + 0.3) = 2.28 \text{ cm}^2.$$

With the temperatures $T_1 = 343^\circ K$ and $T_2 = 323^\circ K$, and a $C = 0.26$ kcal/cm$^2 \cdot$ h $\cdot ^\circ K = 0.302 \cdot 10^{-4}$ W/cm$^2 ^\circ K$ we find

$$Q = 0.00204 \text{ W},$$

which is negligible, compared with the heat transport by conduction.

Heat transport by convection is impossible owing to the small dimensions inside the calorimeter.

Consequently in this case the only significant heat transport mode is conduction, and curve III constitutes the best prediction of the temperature distribution in the rod.

The calibration factor, as defined in subsection 3.2.2, equation (69), is then

$$f_c = \frac{\Delta T}{k_r \cdot r \cdot i^2} = \frac{17.73}{0.997 \cdot 3.40 \cdot 0.5^2} = 21.0 \ ^\circ C \text{ cm/W}$$

as

$$k_r = 1 - 10^{-4}(45 + 10.6 - 22) = 0.997 \quad \text{(see eq. (67))}.$$

Similar calculations were carried out for calorimeters I8/8 and I8/9. The results are listed in table 3.2.4.

Figure A1

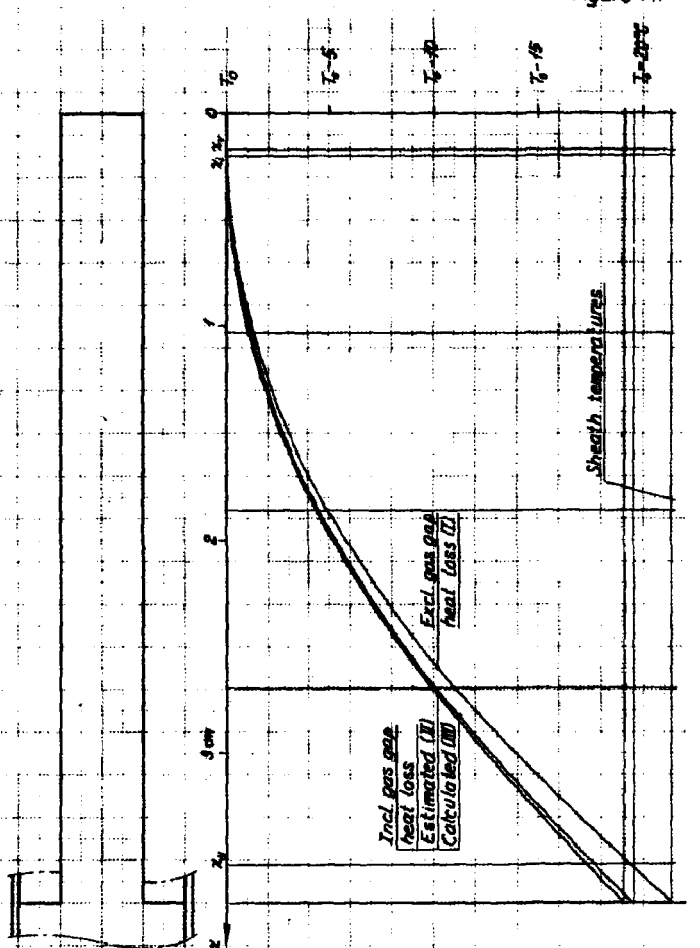

Calculation of temperature distribution along the rod of calorimeter I6/7.

APPENDIX II
DECAY HEAT MEASUREMENTS WITH A25/2

An experimental verification of the decay heat calculations in subsections 2.3. and 2.5.1. can be made by measurement of the residual heat in the calorimeter sample after quick withdrawal from a measurement in the core.

Also the saturation progress during the first minutes of an in-core measurement gives information about the decay heat in the calorimeter sample.

The predominant decay process in the sample is

$$Al^{28} \rightarrow Si^{28} + \beta + \gamma$$

with a nominal half life of 2.3 minutes. This β - γ -release causes heating of the sample which is calculated in subsection 2.5.1. under the assumption of equilibrium of Al^{28}:

Decay- β in the structure	9.5 mW/g
Decay- γ in the structure	3.8 -
Decay- β in the sample	94.6 -
Decay- γ in the sample	6.1 -
Total	114.0 mW/g

at a neutron flux of 10^{14} n/cm^2 sec.

Two measurements have been made: In 4-VGR/2 at CCP (horizontal core centre plane) 28 December 1965, and in 7V150 cm above CCP, 2 January 1966. The measurement procedure was the following:

The sample was pre-heated electrically by means of the built-in heater coil in order to facilitate the operation of the zero- ΔT-instrumentation during the transient at start of the in-pile measurement which lasted 10 minutes. The calorimeter was then withdrawn into the flask and the residual heat was measured during another 10 minutes.

With a position dose rate PDR (see 2.1.2.), a material dose rate MDR_d from decay processes at equilibrium, and a material dose rate MDR_r comprising the remaining part of the material dose rate, the nuclear heating at the moment of insertion is

$$W_o = PDR + MDR_r \qquad (1)$$

During the irradiation the nuclear heating increases according to

$$W_i = PDR + MDR_r + MDR_d (1-e^{\lambda t}), \qquad (2)$$

where λ is the predominant decay constant ($\lambda_{Al28} = 0.301$ sec $^{-1}$)
Immediately before withdrawal the heating is

$$W_{10} = PDR + MDR_r + MDR_d (1-e^{-10\lambda}) = W_o + 0.96\ MDR_d \qquad (3)$$

decreasing after the withdrawal according to

$$W_d = 0.96\ MDR_d\ e^{-\lambda t}. \qquad (4)$$

The exponential function on the right-hand side of eq. (4) can be isolated in eq. (2) as

$$W_s = MDR_d\ e^{-\lambda t} = PDR + MDR_r + MDR_d - W_i$$

$$= \frac{1}{0.96} (W_{10} - 0.04\ W_o) - W_i \ . \qquad (5)$$

Thus the plotted results of W_s calculated by means of eq. (5) from the measured values of W_i should merge with those of $\frac{1}{0.96} W_d$.

By extrapolation of the W_i-curves we find

7V1: W_o = 90.1 mW/g; W_{10} = 125.5 mW/g; W_s = 127.0 - W_i mW/g
4VGR/2: W_o = 12.0 -; W_{10} = 16.4 mW/g; W_s = 16.6 - W_i mW/g .

The curves in figure A2/1 are drawn with slopes according to the nominal half life of Al^{28}: 2.3 minutes. The total in-pile decay heats, read at t = 0, are listed in table A2/2 for comparison with the values calculated by means of the measured neutron fluxes.

Table A2/1
Measurement results

Decay				Saturation		
Pos.	t (sec)	W_d (mW/g)	$\frac{1}{0.95} W_d$ (mW/g)	t (sec)	W_i (mW/g)	W_s (mW/g)
	-2	125.8	(125.8)			
	0	-		0	-	
	8	34.0	35.4	8	90.6	33.4
	38	27.9	29.1	38	95.7	31.3
	68	22.7	23.6	68	102.1	24.9
	98	21.3	22.2	123	108.5	18.5
	128	17.3	18.0	243	117.1	9.9
7V1	188	12.9	13.4	303	118.9	8.1
	248	9.8	10.2	363	121.1	5.9
	308	7.5	7.8	423	124.0	8.0
	368	5.7	5.9	483	123.3	3.7
	428	4.2	4.4	543	123.5	3.5
	488	3.0	3.1	603	125.4	1.6
	0	-		0	-	
	30	3.95	4.11	30	12.7	3.9
	60	3.30	3.44	60	13.3	3.3
	90	2.68	2.79	90	13.9	2.7
	120	2.28	2.37	120	14.1	2.5
	150	1.79	1.86	150	14.5	2.1
4VGR/2	180	1.58	1.65	180	14.8	1.8
	240	1.25	1.30	240	15.4	1.2
	300	0.88	0.90	300	15.8	0.8
	360	0.68	0.71	360	16.1	0.5
	420	0.56	0.58	420	16.2	0.4
	540	0.33	0.34	600	16.4	0.2

Table A2/2

Material dose rate from decay of activated nuclei

	Thermal neutron flux n/cm^2s	Decay heat (mW/g)	
		Calculated	Measured
7V1	0.33×10^{14}	37.6	36.0
4VGR/2	0.04×10^{14}	4.6	4.5

Figure AE/1

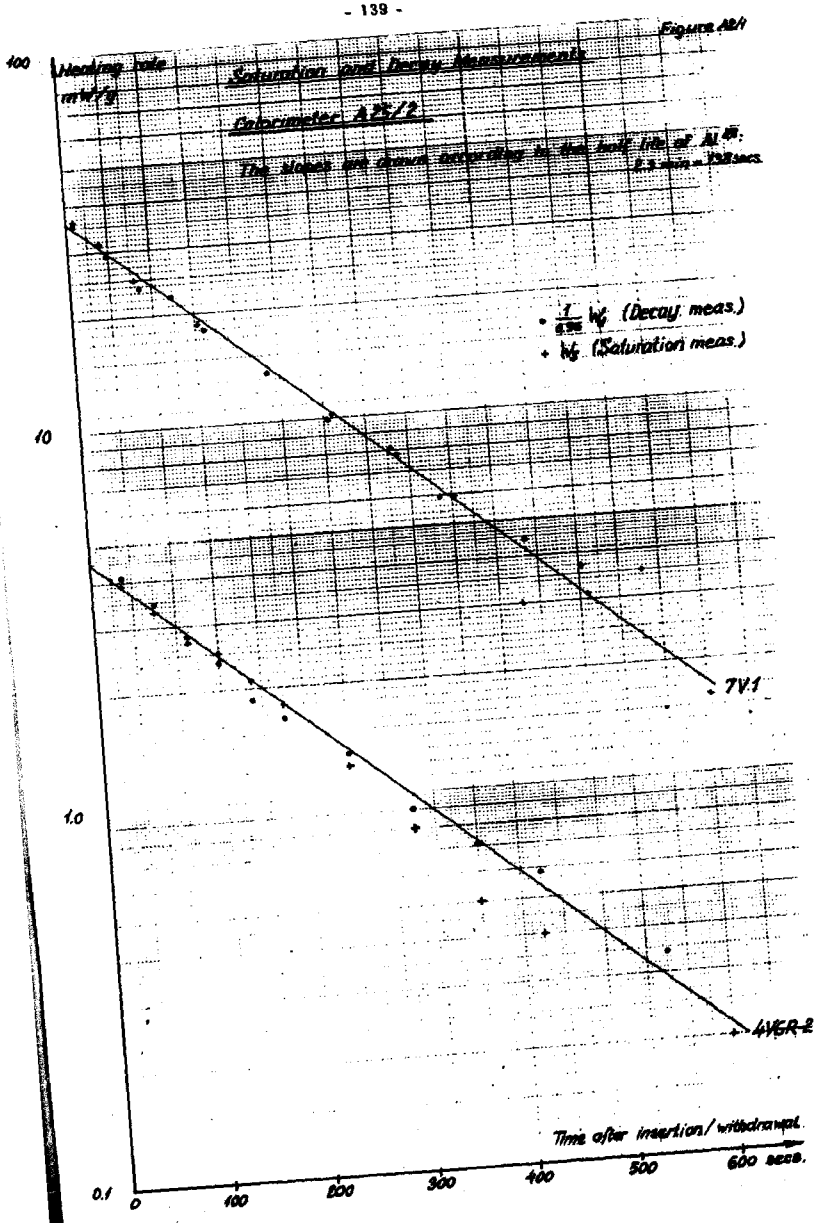
100
10
1.0
0.1
Heating rate mW/g
Saturation and Decay Measurements
Calorimeter A 2½/2
The values are plotted according to the half life of Al 28:
2.3 min = 138 secs.
• 1/0.96 Wf (Decay meas.)
+ Wf (Saturation meas.)
7V1
4V5R-2
Time after insertion/withdrawal.
0
100
200
300
400
500
600 secs.

APPENDIX III
EVALUATION OF UNCERTAINTY OF MEASUREMENTS

1. Adiabatic Calorimeter A25

The nuclear heat is given by eq. (33) in 3.1.2.:

$W = 4.1868 \cdot c \cdot dT/dt \quad W/g,$

where the specific heat c is found by means of eqs. (37) and (45):

$$c = \frac{1}{4.1868 \cdot M_p} \cdot \frac{I_{3-4}}{I_{1-2}+I_{3-4}} \cdot \frac{t_2 - t_1}{T_2 - T_1} \cdot r \cdot i^2 \quad cal/^oC\ g\ .$$

The indeterminateness of the individual figures is:

	Size	Indeterminateness Absolute	Relative	Squares (rel.)
I	~ 5000 °C sec	20 °C sec	0.4%	0.16
t	~ 400 sec	2 sec	0.5%	0.25
ΔT	~ 8 °C	0.05 °C	0.6%	0.36
M_p	~ 8 g	0.1 mg	0.0%	0.00
r	~ 25 Ω	0.01 Ω	0.0%	0.00
i	~ 0.1 amp	0.5 mA	0.5%	0.25
$\frac{dT}{dt}$	~ 0.5 °C/sec	0.003 °C/sec	0.6%	0.36

Sum of squares 1.38

Uncertainty of the instrumentation:

$$\Delta W = \sqrt{1.38} = \sim 1.2\% \ .$$

In the value of I is included the indeterminateness of t and ΔT ($=T_2-T_1$). The T-value comprises the instrument and reading indeterminateness and the thermocouple calibration uncertainty.

To this instrumentation uncertainty a contribution arising from possible deviations from the adiabatic conditions in the calorimeter must be added.

The delta temperature between sample and heat shield can be kept below 0.1 °C up to about 300 m W/g. At higher values of nuclear heat the minimum obtainable ΔT increases according to the curve shown in fig. A3.

Characteristic values of the thermal conductivity of the gas gap are:

CO_2 at atm. pressure: 25 mW/°C

Vacuum: 12 mW/°C

At ΔT's according to fig. A3 the corresponding errors will be:

Nuclear heat mW/g	10	50	100	300	500	800
T °C	0.1	0.1	0.1	0.1	0.3	1.0
Gas gap heat transfer:						
at vacuum (mW)	1.2	1.2	1.2	1.2	3.6	12
with CO_2 (1 atm) (mW)	2.5	2.5	2.5	2.5	7.5	25
Errors:						
at vacuum (%)	1.5	0.3	0.2	0.1	0.1	0.2
with CO_2 (1 atm) (%)	3.1	0.6	0.3	0.1	0.2	0.4

The sample/can delta temperature is recorded during each measurement in order to control that it is within the limits specified above. Normally the error is negligible and it is then included in the measurement uncertainty, thus giving the curves of uncertainty shown in fig. A3.

Below 50 mW/g the gas gap error becomes significant, and corrections for the gas gap heat transfer have to be made in each case. This neccessitates a thorough calibration of the sample and can thermocouples, as temperatures in the range 0.01 °C have to be detected.

In this way the measurement uncertainty can be kept below 1.5% in the range 10 - 800 mW/g.

2. Isothermal Calorimeter I6

The nuclear heat measured by the isothermal calorimeter is given by eqs. (69), (70), and (71) in 3.2.1.:

$$q = f_s \cdot \Delta T_m \ W/g,$$

where $f_s = \frac{k_c}{A V f_c}$ W/g °C

and $f_c = \frac{\Delta T_{cal}}{k_r r i^2}$ cm °C/W .

The indeterminateness of the individual figures is

	Size	Indeterminateness Absolute	Relative	Squares (rel)
ΔT	~ 10 °C	0.05 °C	0.5%	0.25
A	~ 0.15 cm^2	0.0025 cm^2	1.7%	2.89
V	2.70 g/cm^3	0.02 g/cm^3	0.7%	0.49
i	~ 0.5 amp	0.005 amp	1 0%	1.00 (x2)
r	3.4 Ω	0.05 Ω	1.5%	2.25
k_r	1.0	$5 \cdot 10^{-4}$	0.0%	0.00
k_c	0.85	0.005	0.6%	0.36

Sum of squares: 8.24

Errors from gas gap heat transfer and deviations in the thermal conductivity of the sample rod are eliminated by the calibration method.

Thus the resulting measurement uncertainty is:

$\Delta q = \sqrt{8.24} \approx \sim 3\%$.

Figure A3

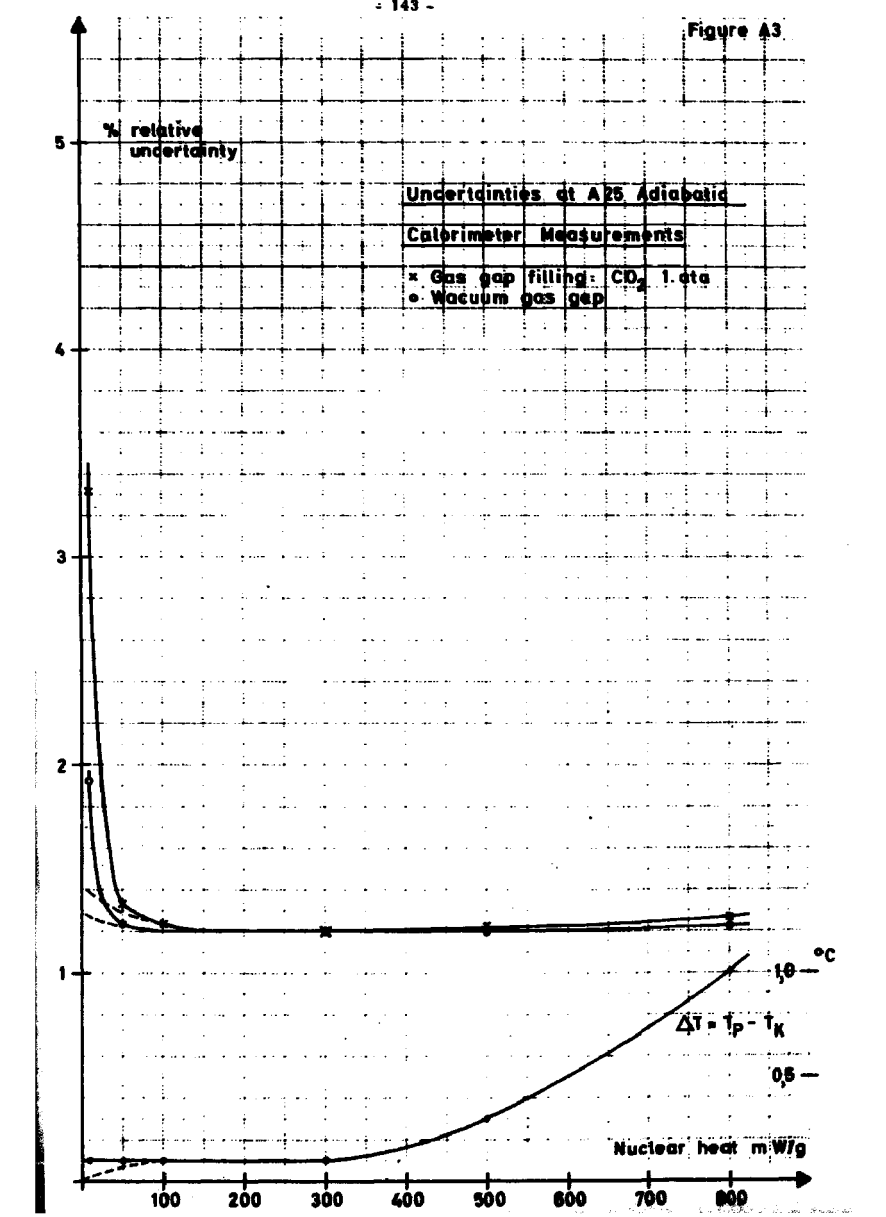
% relative uncertainty
Uncertainties at A25 Adiabatic Calorimeter Measurements
× Gas gap filling: CD_2 1 ata
• Vacuum gas gap
5
4
3
2
1
°C
1,0
0,5
$\Delta T = T_P - T_K$
Nuclear heat mW/g
100
200
300
400
500
600
700
800

ERRATA

Page 31, Equation (12), last term: Change to $\frac{L}{2R}$

- 53, Table 2.5.15, 5th column: Change (barns) to (grams)
  - 3.97 - 0.99
  - 8.357 - 83.565
  - 5.269 - 1.035

- 53, Table 2.5.15., 7th column: Change 0.322 to 0.080
  - 0.021 - 0.207
  - 0.004 - 0.001

- 56, Table 2.5.20, 10th column: Change 0.0185 to 0.185
  - 0.0050 - 0.0037
  - 0.0027 - 0.0045
  - 0.0009 - 0.0025
  - 0.0005 - 0.0018
  - 0.00005 - 0.0011

- 56, Table 2.5.20, 11th column: Change 0.010 to 0.108
  - 0.003 - 0.002
  - 0.283 - 0.380

- 57, Table 2.5.21, 6th - 8th column: Change 3.468 to 0.317
  - 0.238 - 0.373
  - 17.4 - 23.0
  - 2.6 - 2.2

- 58, Table 2.5.23, 2nd column: Change 9.9 to 8.8
  - 17.4 - 23.0
  - 2.6 - 2.2
  - 142.0 - 146.1